Durham E-Theses

Simulations of electron transport in GaN devices

Arabshahi, Hadi

How to cite:

Arabshahi, Hadi (2002) *Simulations of electron transport in GaN devices*, Durham theses, Durham University. Available at Durham E-Theses Online: http://etheses.dur.ac.uk/4119/
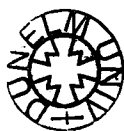
Use policy

Simulations of Electron Transport in GaN Devices

Hadi Arabshahi

A thesis

submitted in candidature for the degree of

Doctor of Philosophy

at the University of Durham,
Department of Physics

January 2002

This thesis is dedicated to my wife Mitra and my son Ramtin. Without their love, support and understanding, this effort would not been possible.

Abstract

This thesis deals with the development and application of Monte Carlo simulations to study electron transport in bulk GaN in the wurtzite crystal structure and the properties of field effect transistors made from the material. There is a particular emphasis on transport in the high electric field regime and transistors operating at high voltages. The simulation model includes five sets of non-parabolic conduction band valleys which can be occupied by electrons during high field transport. The effects on electron transport of impurities and the relevant phonon scattering mechanisms have been considered. Results for electron transport at both low and high electric field are presented and compared with the properties of GaN in the zincblende structure, of other group-III nitride semiconductors, and of GaAs. The dependence of the transport properties on the material parameters is discussed and also with regard to the temperature, donor concentration and electric field magnitude and direction. The transport properties of electrons in wurtzite GaN n^+-i(n)-n^+ diodes are also explored, including the effect of the upper valleys and the temperature on hot electron transport.

Simulations have also been carried out to model the steady-state and transient properties of GaN MESFETs that have recently been the subject of experimental study. It has been suggested that traps have a substantial effect on the performance of GaN field effect transistors and we have developed a model of a device with traps to investigate this suggestion. The model includes the simulation of the capture and release of electrons by traps whose charge has a direct effect on the current flowing through the transistor terminals. The influence of temperature and light on the occupancy of the traps and the I-V characteristics are considered. It is concluded that traps are likely to play a substantial role in the behaviour of GaN field effect transistors.

Further simulations were performed to model electron transport in AlGaN/GaN heterojunction FETs. So called HFET structures with a 78 nm $Al_{0.2}Ga_{0.8}N$ pseudomorphically strained layer have been simulated, with the inclusion of spontaneous and piezoelectric polarization effects in the strained layer. The polarization effects are shown to not only increase the current density, but also improve the electron transport by inducing a higher electron density close to the positive charge sheet that occurs in the channel.

Declaration

The work presented in this thesis has been carried out by the candidate and has not previously been submitted for any degree and is not being currently submitted in candidature for any other degree.

Ph.D Candidate

Ph.D Supervisor

Acknowledgements

I would first of all like to thank my supervisor, Professor Dick Abram, for his help and his endless patience and support during my course of study, and for his comments during the time spent writing this thesis. His supervisory style has allowed me to learn and develop my understanding of the details of this work in particular, and of science in general.

My special thanks go to Dr Gavin Crow for making available computer simulation programs and for his comments on the problems that have confronted me during my research. I also appreciate those who have been in the Condensed Matter Theory Group and have spent time discussing problems and providing practical help, especially Dr Stuart Brand, Dr Stewart Clark, Dan Harrison, David Dugdale, Ian Bolland and Anucha Yangthaisong. I would also like to thank Dr Lydia Heck for solving every conceivable computational problem and for her unfailing cheerfulness. I also wish to thank my parents, who have always remembered me in their prayers, for their support throughout my studies.

Finally, I wouldn't find myself in the position I am now without the constant patience and encouragement of my wife Mitra and my son Ramtin. They have offered support of every kind throughout the course of my education in Durham, and especially at times when I have needed it most.

Contents

List of Figures

Chapter 1

Introduction

The origin of semiconductors goes back to Faraday and Becquerel. Faraday discovered in 1833 that silver sulphate has a negative temperature coefficient, and in 1839 Becquerel studied the properties of various electrolytes. In 1948 Brattain and Bardeen of the Bell laboratories in the U.S.A. invented the first contact transistor which was made of germanium, and a few months later Schockley [1] produced a junction transistor which soon replaced the point contact transistor and after extensive improvements became the device which we know today as the bipolar transistor. Following the developments in the 1940s semiconductors rapidly grew in importance and now form the foundation of modern electronics, being used in a vast range of applications.

A wide variety of semiconductor devices are available, fabricated from a range of semiconductor materials. The most common active devices found in electronic circuits include diodes, field effect transistors, bipolar transistors, microwave and optoelectronic devices. Silicon is the most commonly used semiconductor material for both discrete and integrated devices in electronic circuits, although other binary compounds, particularly those formed from elements of group III and V, are used for specialist applications. In addition to binary compounds, ternary and quaternary alloys also exist and can be used to advantage in certain applications. Recently there has been much interest in the alloy SiGe as a way of enhancing the speed of transistors for the fabrication of field effect transistors.

This thesis aims to use Monte Carlo simulation methods to provide an insight into
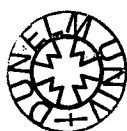
the advantages of using GaN and related materials. GaN and other group-III nitride compounds constitute an interesting material system because, together with alloys Al-GaN, GaInN and AlInN, they provide semiconductors with direct bandgaps from 1.9 eV (InN) to 6.2 eV (AlN). The huge potential of this material system in high-power, high-temperature, high-frequency and high phonon energy optoelectronic devices is now being achieved as the material technology improves. Light emitting diodes (LEDs) based on nitride semiconductors have the potential to display full colour because emission of the three primary red, green and blue colours is possible. In addition, emission at short wavelength means that nitride based laser diodes can be focused more sharply than the lasers that are currently used and so can be used to increase storage capacities. For example, the storage density of digital versatile disks (DVDs), is predicted to go up from 1 Gb to about 40 Gb per disk when GaN blue lasers are used. Semiconductor nitrides are also prime condidates for ultra violet (UV) photodetectors which have many potential applications in such diverse areas as solar astronomy and combustion process monitoring.

The large electron drift velocity in GaN, the large band discontinuties at Al-GaN/GaN heterojunctions, and the tolerance to high temperatures in nitride p-n junctions form the basis for high power electronic devices with applications requiring high power efficiency and operation under extreme conditions.

However, there have been several growth related problems resulting in imperfections in epitaxial GaN layers particularly, the lack of a good substrate material. There are also problems with large n-type background carrier concentrations, the difficulty in doping GaN p-type and the lack of a suitable etchant for the material. Nevertheless, there have been substantial improvements in the quality of material in recent years. Optimized buffer layers on sapphire substrates and more recently the availability of SiC substrates have allowed greatly improved material to be grown by hydride vapor phase epitaxy (HVPE) [2] , metalorganic chemical vapor deposition (MOCVD) [3,4] and molecular beam epitaxy (MBE) [5,6] techniques. As a result of such improvements, GaN background carrier concentrations have been reduced to as low as 4×10^{22} m^{-3} in high quality thin films. Also an understanding of the Mg acceptor impurity has made

it possible to dope GaN to hole concentrations as high as 3×10^{24} m^{-3}. These advances in material quality and processing have allowed device researchers to demonstrate and commercialize GaN based optical sources.

The first blue GaN LED was fabricated by Pankove *et al.* [7] in the early 1970s. Due to an inability at the time to dope GaN p-type, these devices were not conventional p-n junction LEDs, but rather metal-insulator-semiconductor (MIS) structures. Only recently, when Amano *et al.* [8] first obtained p-type GaN was a p-n junction GaN LED realized. Advances in all aspects of GaN technology have finally enabled several types of GaN field effect transistors (FETs) to be fabricated, including metal-semiconductor FETs (MESFET) [9, 10], AlGaN/GaN HFETs [11], metal-oxide-semiconductor FETs (MOSFET) [12], AlGaN/GaN doped channel [13] and AlGaN/GaN HEMTs [14].

The development of GaN based transport devices was initially limited by poor material quality and unreliable knowledge of the carrier transport properties. There has been a substantial experimental effect to characterise the material. Also theoretical studies of carrier transport in the nitride compounds and alloys, have been useful in predicting various quantities which are not readily accessible through experiment. Such studies continue to have an important role to play in the design, development and understanding of nitride devices. In particular, they reduce the time and cost required for developing a specific device, by allowing the designer to home in on a suitable geometry and doping profile prior to the fabrication stage.

A knowledge of the velocity-field characteristics of carriers is important in considering a material for electronic device applications. In particular, the low field mobility is considered to be an important figure of merit, although the high field drift velocity can be more important in device applications. Monte Carlo simulation of the electron transport in GaN as a function of electric field at different temperatures and doping concentration was first carried out by Littlejohn *et al.* in 1976 [15]. Littlejohn considered a two valley model and included scattering by acoustic phonons, polar optical phonons, ionized impurities, and piezoelectric charge to predict a peak in the electron drift velocity of 2×10^5 ms^{-1} at a field of $\sim 2 \times 10^7$ Vm^{-1} for an electron concentration of 10^{23} m^{-3}, which is considerably larger than that found in Si or GaAs. The

work of Littlejohn was extended by Gelmont *et al.* [16], to include the effect of higher valleys in the conduction band. Gelmont predicted a peak electron velocity at 300 K of 2.7×10^5 ms^{-1} for an electron concentration of 10^{23} m^{-3} at a field of $\sim 1.5 \times 10^7$ Vm^{-1}. Gelmont's results also suggested that a low field electron mobility as high as 1400 cm^{2}V^{-1}s^{-1} could be achieved for uncompensated GaN at room temperature with a donor concentration of $\sim 10^{23}$ m^{-3}. Experimentally, a mobility of more than 1000 cm^{2}V^{-1}s^{-1} at room temperature with similar doping concentration has been reported in the case of high quality samples with very low compensation. There have been some reports specifically concerned with the calculation of low field electron mobility in GaN. Chin *et al.* [17] have used the variational principle to calculate low field electron mobility and compared results with fairly old experimental data [18]. They tried to fit the experimental data with a greater compensation ratio than reported, probably reflecting the fact that in the old samples, the low electron mobility was limited by poor substrate and buffer quality, and other growth related problems. The iterative technique has been used by Rode and Gaskill [18] to obtain the dependence of low field mobility on electron concentration at room temperature but they found a poor fit to experiment at high electron concentrations. Littlejohn *et al.* [15] and Bhapkar *et al.* [19] have also calculated the low field electron mobility in GaN using the Monte Carlo method, but they did not consider the effect of dopant compensation on the electron mobility, which can be important in GaN because of the role of nitrogen and/or gallium vacancies [20, 21].

Simulations of GaN and other nitride electronic devices are based on the physics of their electron transport properties and can provide valuable insight into the detailed device operation. In particular, they may be used to predict the characteristics of new devices within the constraints of the information available on the nitride material properties. Simulations may be used for the full range of the operating conditions and have been used successfully to model and analyse steady-state, transient, large-signal and high frequency operation. The Monte Carlo technique is a very powerful and much used technique for the simulation of carrier transport in semiconductor materials and devices. Interest in using Monte Carlo techniques to characterise material proper-

ties and device operation has grown steadily since Kurosawa [22] first introduced the method into semiconductor modelling in 1966. Its increasing popularity can be attributed to the continuing search for a detailed understanding of semiconductor device properties and because of the steady improvement in computer processing power (both in terms of speed and available memory). Monte Carlo techniques can be applied to a wide range of semiconductor materials and to characterise a wide range of devices from FETs to optoelectronic devices. The application of Monte Carlo simulation to nitride semiconductors and devices is the subject of this thesis. The rest of this thesis is organized as follows:

Chapter 2 describes the electronic band structure model used for the transport calculations. We consider GaN in both the zincblende crystal structure and the more common wurtzite structure. Some low-field transport calculations have been carried out using an iterative solution of the Boltzmann equation in a one-valley model. However, the Monte Carlo simulations are based on 3 and 5 valley models for the zincblende and wurtzite crystal structures, respectively. A review of the scattering processes relevant to electron transport in GaN structures which is considered in the calculation models is also discussed in this chapter.

Chapter 3 describes the low and high field transport calculations in zincblende and wurtzite GaN. To calculate the temperature and donor concentration dependence of the low-field electron mobility in zincblende and wurtzite GaN an iterative approach based on conduction in the non-parabolic Γ-valley at the centre of the first Brillouin zone is used. A single valley is adequate for the low field mobility calculations since a low applied electric field of 10^4 Vm^{-1} is used which is insufficient to excite the electrons to higher valleys.

Characterization of electronic transport properties of GaN at high electric fields is performed using an ensemble Monte Carlo simulation. The calculations are performed using an appropriate multivalley model. For the wurtzite crystal structure, the first five conduction band valleys, which extend in energy to about 3.1 eV above the lowest conduction band minimum, are included in the simulation. In our calculations steady-state and transient electron transport characteristics of bulk GaN and other nitride

materials have been simulated. In the case of wurtzite GaN, transport has been modelled with an electric field applied both parallel and perpendicular to the $(0001)c$-axis. Additionally, the effect of varying the temperature and donor concentration on the steady-state velocity, valley occupancy and average electron energy has been examined.

Chapter 4 describes a Monte Carlo simulation study of wurtzite n^+-n-n^+ diodes. The simulation results are used as the basis of a discussion of the influence of the high lattice temperatures on hot electron transport and the electron distribution function. The implications for the gate-drain region of GaN power FETs are also considered. In addition, the importance of back-scattering of electrons from the anode n^+-layer, the effects of active layer length and the dependence of electron doping on the length of the active layer are examined.

Chapter 5 describes a theoretical study of a GaN MESFET. The I-V characteristics, transconductance and cutoff frequency are calculated for a GaN MESFET and the results compared with experiment. The simulations suggest that traps play an important role in device behaviour and that the current collapse observed experimentally in GaN MESFETs is a trap related phenomenon. The influence of trap parameters like capture cross-section, trap density and trap energy on the device characteristics are explored. We also simulate the photoionization of traps by light incident on the device and the related effect of optically induced reversal of current collapse.

Chapter 6 describes two-dimensional self-consistent Monte Carlo simulation for electron transport in an $Al_{0.2}Ga_{0.8}N$/GaN strained-layer HFET structure. In the simulated GaN HFET the piezoelectric polarization effect in the strained layer are taken into account by a simple model. The polarization effect is shown to not only increase the current density, but also improve the electron transport properties in this device.

Finally, conclusions drawn from this research are presented in chapter 7 and suggestions are made for further work.

Chapter 2

Energy Bands and Scattering Mechanisms in GaN

2.1 Introduction

The theoretical study of the electronic transport properties of semiconductors generally requires a detailed knowledge of the energy band structure and the different electron scattering mechanisms. Specifically, in the study of the high field properties, consideration of the conduction band over a substantial range of energy is very important because of the level of excitation experienced by the electrons. Thus it is essential to have an appropriate band structure model and to understand how the important electron scattering mechanisms vary with energy, wavevector and temperature.

In section 2.2 we give a brief review of the GaN crystal structures and their band structures and go on to describe the models and material parameters which are employed in our transport calculations. Section 2.3 describes the scattering processes which are relevant to transport in GaN. The goal of this section is a quantitative understanding of the different scattering mechanisms to make possible a calculation of the electron transport in GaN, based on either the iterative solution of the Boltzmann equation or Monte Carlo simulation, which are described in subsequent chapters.

2.2   Crystal and band structure

GaN can crystallize in either the zincblende or wurtzite structures, which have slightly different material properties and substantially different band structures. However, the wurtzite phase of GaN (and also of AlN and InN) is the more stable bulk form of the material and the common form for epitaxial layers, although thin epitaxial layers can be grown with the zincblende structure.

GaN in the zincblende structure is shown in figure 2.1a. It can be regarded as two interpenetrating face-centred cubic (fcc) Bravais lattices displaced along the diagonal of the cube in figure 2.1a by one quarter of its length. Ga atoms are located on one fcc lattice and N atoms on the other resulting in a structure where each atom is surrounded by four neighbours of the other type at the corners of a regular tetrahedron [23]. There is one unit of GaN per primitive unit cell where the primitive lattice vectors are described in terms of the cubic lattice constant a by

$$
\begin{aligned}
\mathbf{a} &= (0, 1/2, 1/2)\, a \quad ; \\
\mathbf{b} &= (1/2, 0, 1/2)\, a \quad ; \\
\mathbf{c} &= (1/2, 1/2, 0)\, a \quad ; \qquad\qquad (2.1)
\end{aligned}
$$

in a Cartesian basis. Figure 2.1b shows the first Brillouin zone of GaN in the zincblende structure. The first Brillouin zone is a truncated octahedron of volume $4(2\pi/a)^3$. It has 14 faces, six squares perpendicular to the $\langle 100 \rangle$ directions and eight regular hexagons perpendicular to the $\langle 111 \rangle$ directions. The high-symmetry points Γ, X and L, which are at the centre of Brillouin zone, the centres of the squares and the centres of the hexagons respectively, are indicated in the figure.

The wurtzite crystal structure of GaN is shown in figure 2.2a. It can be regarded as an interpenetration of two hexagonally close packed (HCP) sublattices with a relative displacement along the c-axis by uc where u is the so called internal parameter and c is the lattice constant for the c-axis. The distance between in-plane atomic neighbours is denoted by a. For an ideal wurtzite structure $c/a = \sqrt{8/3} = 1.633$ and $u = 3/8 = 0.375$ and the atoms have the regular tetrahedral coordination of nearest neighbours that occurs for the zincblende structure. The difference between the two structures is in the
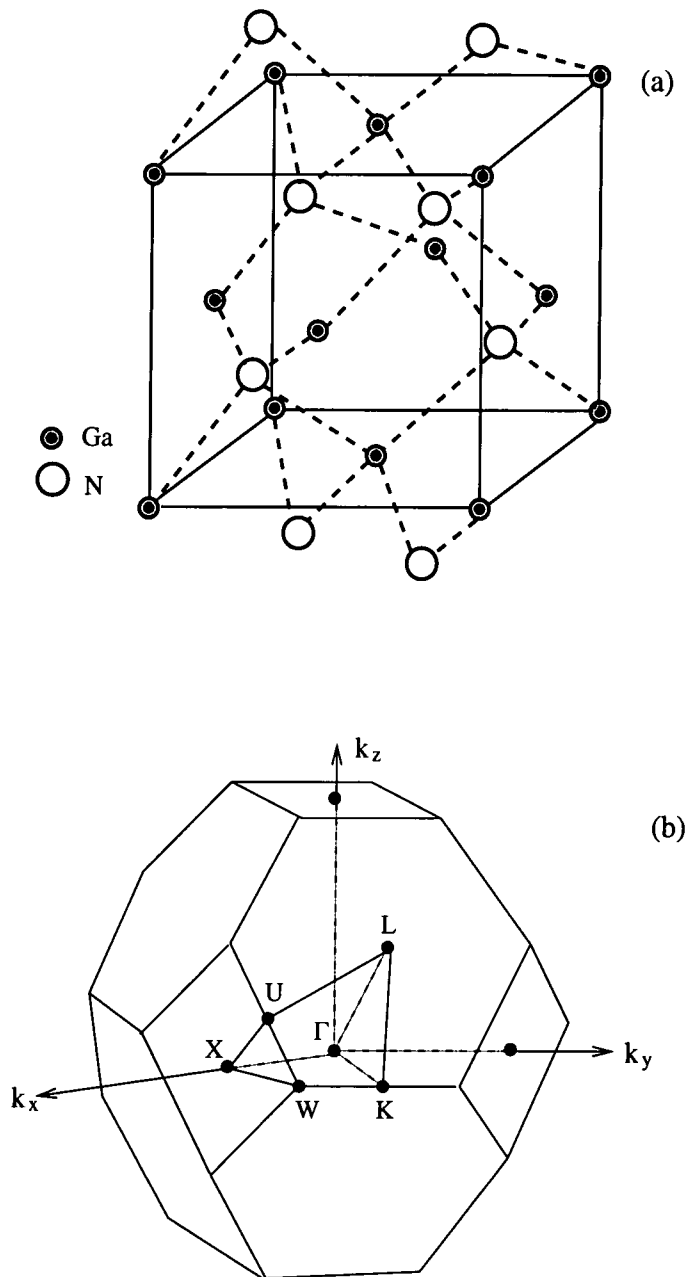
Figure 2.1: (a) The crystal structure of zincblende GaN. (b) The first Brillouin zone of a zincblende crystal with the principal symmetry directions and points.
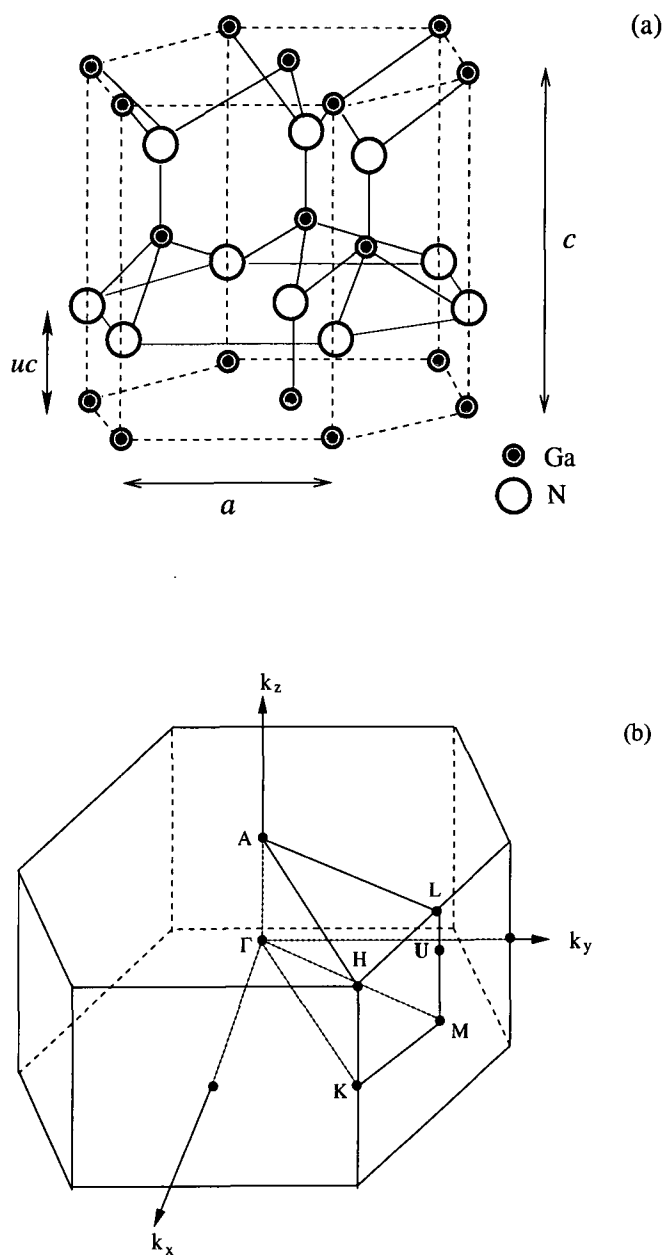
Figure 2.2: (a) The crystal structure of wurtzite GaN. (b) The first Brillouin zone of a wurtzite crystal with the principal symmetry directions and points.

next nearest neighbour arrangement. The structure of GaN is nearly ideal with $c/a = 1.627$ and $u = 0.377$, but AlN is far from ideal with $c/a = 1.601$ and $u = 0.382$ [23]. The primitive lattice vectors are written in terms of the two lattice constants a and c as

$$
\begin{aligned}
\mathbf{a} &= (\sqrt{3}/2, 1/2, 0)\, a \quad ; \\
\mathbf{b} &= (-\sqrt{3}/2, 1/2, 0)\, a \quad ; \\
\mathbf{c} &= (0, 0, c/a)\, a \qquad ;
\end{aligned}
\tag{2.2}
$$

where c/a is called the axial ratio. There are two units of GaN per primitive hexagonal unit cell. The first Brillouin zone of wurtzite GaN which is a hexagonal prism of volume $\frac{2}{\sqrt{3}} \cdot (2\pi)^3/a^2 c$ is shown in figure 2.2b together with the locations of the high-symmetry points Γ, K, M and U.

2.2.1 Band structure features

In order to calculate the electronic transport properties of GaN a knowledge of conduction band structure is necessary. A full discussion of the electronic band structure of GaN structure in both zincblende and wurtzite phases can be found in, for example, [24–27]. Figures 2.3a and 2.4a show the results of a semi-empirical pseudopotential calculation of the band structures along the main symmetry axes of the Brillouin zone for the zincblende and wurtzite crystal structures of GaN [27]. Although the band structures of the two phases of GaN have some similarities (both have direct fundamental gaps at the Γ point that differ by only about 10% [28]), the conduction bands are sufficiently different to cause a significant variation in their electron transport properties. For example, the nearest satellite valley in the zincblende structure (X point) is about 1.5 eV above the lowest conduction band minimum while the nearest satellite valley in the wurtzite structure, at the U point, is about 2 eV above the minimum. Also, in the wurtzite GaN band structure there is a second Γ conduction band valley at a relatively low energy (approximately 2.1 eV) above the lowest minimum, labelled Γ_3, compared to 4.5 eV in zincblende GaN.

In this thesis we have used a valley model for the calculation of the electronic

transport properties of GaN material and devices. Each valley includes band non-parabolicity by relating the electron energy $E(\mathbf{k})$ to the wavevector $\mathbf{k}$ by

$$\gamma(\mathbf{k}) = E(\mathbf{k})[1 + \alpha_i E(\mathbf{k})] = \frac{\hbar^2 k^2}{2m_i^*} \tag{2.3}$$

where m_i^* is the effective mass at the bottom of the i-th valley and α_i is the non-parabolicity coefficient of the i-th valley which is

$$\alpha_i = E_g^{-1}(1 - \frac{m_i^*}{m_o})^2 \tag{2.4}$$

where m_0 is the free electron effective mass. In the case of wurtzite GaN an ellipsoidal non-parabolic approximation is used to describe the Γ_1 valley in the conduction band. The energy-wavevector relation is defined as

$$E(\mathbf{k})[1 + \alpha_\Gamma E(\mathbf{k})] = \frac{\hbar^2}{2} \left[\frac{k_x^2 + k_y^2}{m_t} + \frac{k_z^2}{m_l} \right] \tag{2.5}$$

which represents a band with ellipsoidal equi-energetic surfaces with rotational symmetry about the c-axis identified by z here, m_t and m_l are the transverse and longitudinal effective masses at the band edge.

For the zincblende structure the well known three-valley model of the energy band structure is used, as illustrated in figure 2.3b, with the Γ, X and L valleys. Table 2.1 shows the valley parameters used in our calculation for GaN in the zincblende structure. The parameters for the valleys are from the recent band structure calculations which have already been used by Shur *et al.* [29] for transport calculations.

In the calculation of transport phenomena in wurtzite GaN a five-valley model is used as illustrated in figure 2.4b. Several authors [16,30,31] have carried out transport calculations using an analytical model for the conduction band based on three types of spherical non-parabolic valley located at Γ_1, U and K. However, in high electric fields the higher Γ_3 and M valleys can also be expected to play an important role in determining the transport properties. Table 2.2 shows the valley parameters used in our calculations for wurtzite GaN. The parameters of the three lower valleys are similar to those accepted by several authors [29,31,32] and already used in previous simulations with just three valleys. The upper valley parameters are selected from

Albrecht *et al.* [25, 33, 34]. However, it should be pointed out that there remains considerable uncertainly over the conduction band parameters, as apparent for example in the considerable difference between those in table 2.2 and those in table II of Bulutay *et al.* [35]

	Γ	X	L
Number of equivalent valleys	1	3	4
Non-parabolicity $(eV)^{-1}$	0.213	0.065	0.029
m_i^*	0.15	0.6	0.4
E_x (eV)	3.2	4.7	6

Table 2.1: Important valley parameters used in our simulation for zincblende GaN where E_x is the energy separation of each valley from the top of the valence band.

	Γ_1	U	Γ_3	M	K
Number of equivalent valleys	1	6	1	3	2
Non-parabolicity $(eV)^{-1}$	0.189	0.065	0.029	0.0	0.7
m_t	0.18	0.4	0.6	0.57	0.3
m_l	0.20	0.4	0.6	0.57	0.3
E_x (eV)	3.5	5.5	5.6	6.5	6.6

Table 2.2: Important valley parameters used in our simulation for wurtzite GaN where E_x is the energy separation of each valley from the top of the valance band. m_l denotes parallel to the $(0001)c$-axis and m_t perpendicular to $(0001)c$-axis.
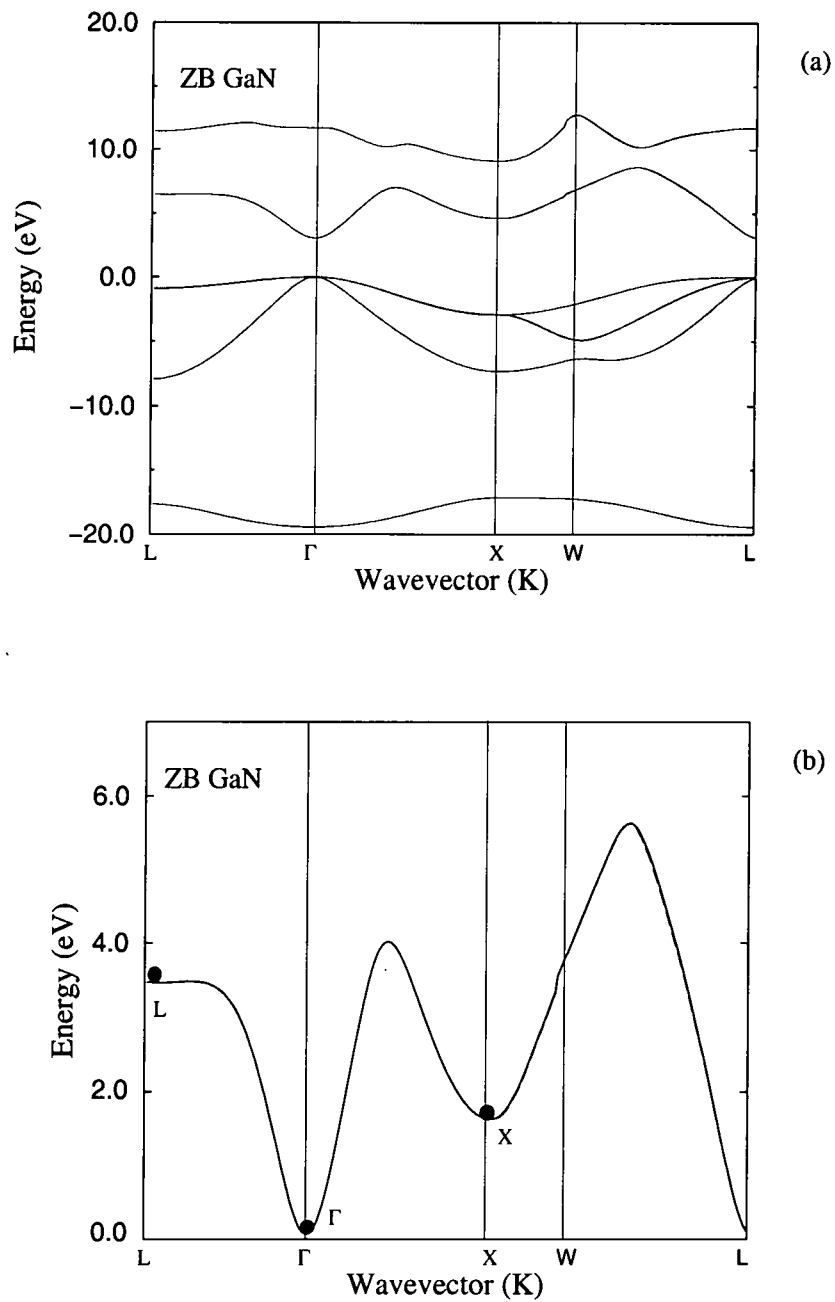
Figure 2.3: (a) The band structure of zincblende GaN in the main directions of symmetry calculated from pseudopotential theory. (b) Three-valley model of the first conduction band of zincblende GaN used in the calculation of electron transport properties using iterative and Monte Carlo simulations.
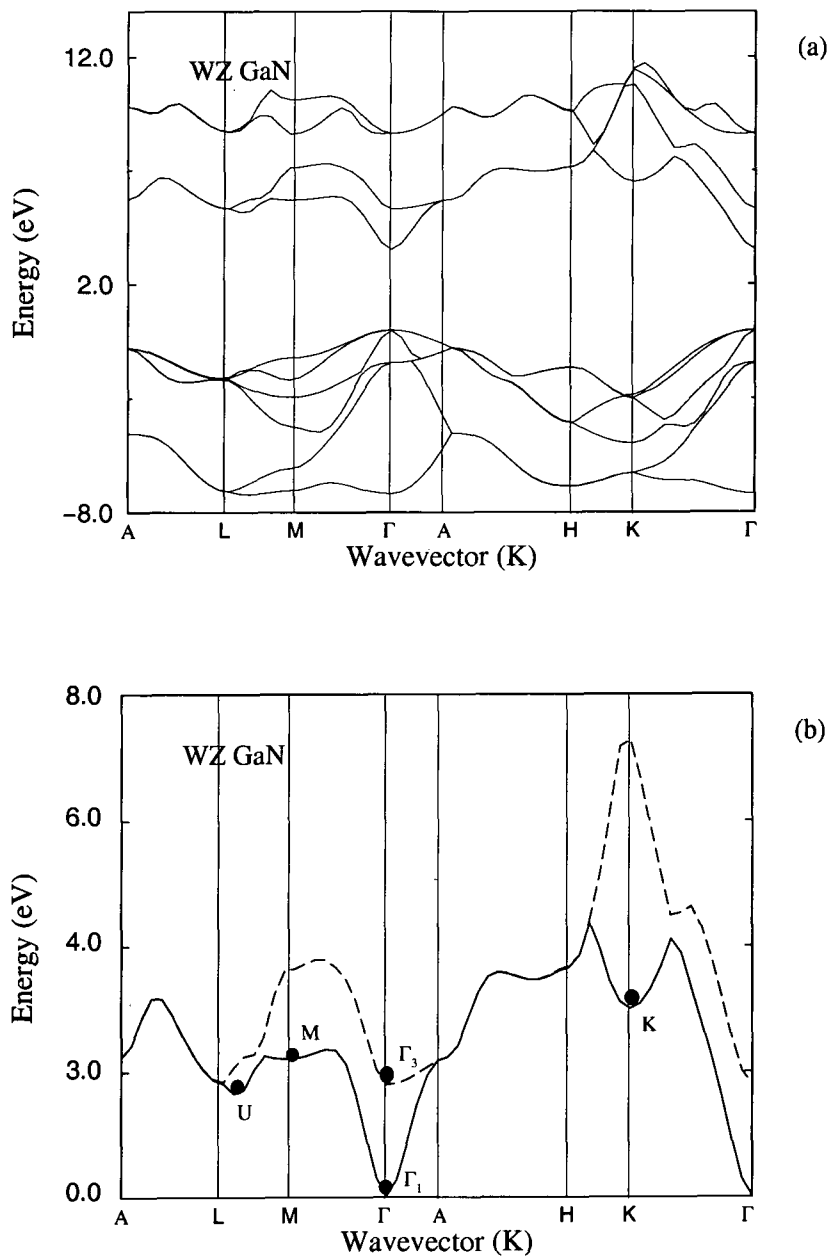
Figure 2.4: (a) The band structure of wurtzite GaN in the main directions of symmetry calculated from pseudopotential theory. (b) Five-valley model of the two lowest conduction bands of wurtzite GaN used in the Monte Carlo simulations.

2.3 Electron scattering mechanisms

In order to calculate the electron transport properties of GaN, we must identify the important electron scattering mechanisms. Therefore in this section we briefly review the relevant electron scattering processes in GaN and give formulae for the scattering rates as a function of electron energy.

2.3.1 General definition

In a semiconductor, there are a number of physical processes which can cause an electron in a certain state to be scattered. The relative importance of each scattering process in a given material depends on the electric field strength and the material properties. When an electron is scattered, the wavevector of the electron is changed from an initial wavevector $\mathbf{k}$ to some final wavevector $\mathbf{k'}$. The time required for a scattering process to change the wavevector from $\mathbf{k}$ to $\mathbf{k'}$ is called the collision duration τ_c. Here we assume collisions occur with $\tau_c = 0$. The inclusion of a scattering in transport calculations normally requires the formulation of the total scattering rate and angular dependence of the scattering between state $\mathbf{k}$ and state $\mathbf{k'}$. The transition rate $s(\mathbf{k}, \mathbf{k'})$ from state $\mathbf{k}$ to state $\mathbf{k'}$ is normally calculated by using Fermi's golden rule

$$s(\mathbf{k}, \mathbf{k'}) = \frac{2\pi}{\hbar} \int |\langle \mathbf{k'}|H|\mathbf{k}\rangle|^2 G(\mathbf{k}, \mathbf{k'})\delta[E(\mathbf{k'}) - E(\mathbf{k}) \pm \Delta E]d^3k' \qquad (2.6)$$

where $|\langle \mathbf{k'}|H|\mathbf{k}\rangle|$ is the matrix element between plane wave functions of the perturbing Hamiltonian describing the scattering agency, ΔE is the energy gain $(+)$ or loss $(-)$ during the transition and the integration is over all final states restricted by the energy conserving delta function. $G(\mathbf{k}, \mathbf{k'})$ is the overlap integral between the periodic parts of the Bloch periodic functions of the initial and final states. The overlap integral is exactly equal to unity for pure s-state wave functions (parabolic conduction bands). When the non-parabolicity of the bands is taken into account, the overlap integral is always less than one and is usually expressed as a function of the non-parabolicity coefficients. In this case the function

$$G(\mathbf{k}, \mathbf{k'}) = 1/2 \sum_{\mu\mu'} |\int d^3r u^*_{\mu'k'}(\mathbf{r})u_{\mu k}(\mathbf{r})|^2 \qquad (2.7)$$

is the overlap integral between the periodic parts of the Bloch functions at **k** and **k′** summed over the doubly degenerate final spin states. In this case Fawcett *et al.* [36] and Kane *et al.* [37] have calculated $G(\mathbf{k}, \mathbf{k'})$ as

$$G(\mathbf{k}, \mathbf{k'}) = (a_{\mathbf{k}} a_{\mathbf{k'}} + c_{\mathbf{k}} c_{\mathbf{k'}} \cos \phi)^2 \tag{2.8}$$

where ϕ is the angle between **k**, **k′** and the quantities $a_{\mathbf{k}}$ and $c_{\mathbf{k}}$ are given by Kane as

$$a_{\mathbf{k}} = \left[\frac{1 + \alpha E(\mathbf{k})}{1 + 2\alpha E(\mathbf{k})}\right]^{1/2} \quad , \quad c_{\mathbf{k}} = \left[\frac{\alpha E(\mathbf{k})}{1 + 2\alpha E(\mathbf{k})}\right]^{1/2} \tag{2.9}$$

Therefore the overlap integral is

$$G(\mathbf{k}, \mathbf{k'}) = \frac{[(1 + \alpha E)^{1/2}(1 + \alpha E')^{1/2} + \alpha(EE')^{1/2} \cos \phi]^2}{(1 + 2\alpha E)(1 + 2\alpha E')} \tag{2.10}$$

where $E' = E(\mathbf{k'})$ is the energy of the electron in the state **k′**. Once the overlap integral between the periodic parts of the Bloch functions at **k** and **k′** are known the total scattering rate $R(\mathbf{k})$ can be calculated by integrating s(**k**, **k′**) in equation 2.6 over all allowed final states

$$R(\mathbf{k}) = \frac{V}{8\pi^3} \int_0^\infty \int_{-\pi/2}^{\pi/2} \int_0^\pi s(\mathbf{k}, \mathbf{k'}) k'^2 \sin \theta d\theta d\phi dk' \tag{2.11}$$

where V is the volume of the crystal.

The scattering mechanisms can be classified into two main types, those due to lattice vibrations and called lattice (or phonon) scattering and defect scattering due to ionized impurities and alloy disorder. In the following sections the behaviour of the electron scattering rates as a function of energy will be shown for various scattering processes in zincblende and wurtzite GaN. The material parameters used in the calculations for zincblende and wurtzite GaN are listed in table 2.3 which are from references [38, 39]. A detailed description of scattering processes incorporated in our calculations is given in the textbooks of Jacoboni and Lugli [40] and Moglestue [41].

2.3.2 Lattice scattering

Lattice scattering occurs due to the vibrations of the constituent atoms of the crystal about their equilibrium sites. These vibrations change the periodic potential in

	zincblende	wurtzite
Density ρ (kgm^{-3})	6100	6150
Longitudinal sound velocity v_s (ms^{-1})	4570	4330
Low-frequency dielectric constant ϵ_s	9.5	9.5
High-frequency dielectric constant ϵ_∞	5.35	5.35
Acoustic deformation potential D (eV)	8.3	8.3
Piezoelectric constant p (Cm^{-2})	0.375	0.375
Polar optical phonon energy $\hbar\omega_{op}$ (eV)	0.0995	0.0995
Lattice constant (Å)	4.5	(a,c) 3.189-5.185

Table 2.3: Material parameters for GaN in zincblende and wurtzite phases.

the semiconductor with time and the result is electron scattering. Lattice vibrations can be quantised and the lattice scattering processes can be considered as an interaction of electrons with the quanta of vibration, called phonons. The phonons have an energy of $\hbar\omega(\mathbf{q})$ where $\omega(\mathbf{q})$ is the vibrational frequency and $\mathbf{q}$ is the wavevector of the vibration. The scattering of electrons with phonons depends on the nature of the phonons involved. There are 2 groups that are each divided into 2 branches. For acoustic phonons, $\omega(\mathbf{q})$ increases with $\mathbf{q}$ almost linearly near the Brillouin zone centre and attains a maximum at the zone edge. The two branches of this group correspond to the longitudinal (LA) and transverse (TA) vibrations. For optical phonons, $\omega(\mathbf{q})$ is fairly constant around the Brillouin zone centre but reaches a smaller value at the zone boundary. The two branches of this group again correspond to longitudinal (LO) and transverse (TO) vibrations.

2.3.3 Intravalley scattering due to acoustic phonons

Acoustic lattice vibrations cause the neighbouring atoms to vibrate in phase. The scattering of electrons by acoustic phonons occurs in two ways:

1. **Deformation potential scattering**:

The acoustic modes modulate the interatomic spacing. Consequently, the position of the conduction and valence band edges and the energy band gap will vary with position because of the sensitivity of the band structure to the lattice spacing. The energy change of a band edge due to this mechanism is defined by a deformation potential and the resultant scattering of carriers is called deformation potential scattering. The energy range involved in the case of scattering by acoustic phonons is from zero to $2\hbar v \mathbf{k}$, where $\mathbf{v}$ is the velocity of sound, since momentum conservation restricts the change of phonon wavevector to between zero and $2\mathbf{k}$, where $\mathbf{k}$ is the electron wavevector. Typically, the average value of $\mathbf{k}$ is of the order of 10^7 cm^{-1} and the velocity of sound in the medium is of the order of 10^5 cms^{-1}. Hence, $2\hbar v\mathbf{k} \sim 1$ meV , which is small compared to the thermal energy at room temperature. Therefore, the deformation potential scattering by acoustic modes can be considered as an elastic process except at very low temperature. The deformation potential scattering rate with either phonon emission or absorption for an electron of energy E in a non-parabolic band is given by Fermi's golden rule as [41]

$$R_{de}(\mathbf{k}) = \frac{\sqrt{2}D_{ac}^2(m_t^{*2}m_l^*)^{1/2}k_B T}{\pi \rho v^2 \hbar^4} \frac{\sqrt{E(1+\alpha E)}}{(1+2\alpha E)}[(1+\alpha E)^2 + 1/3(\alpha E)^2] \quad (2.12)$$

where D_{ac} is the acoustic deformation potential, ρ is the material density and α is the non-parabolicity coefficient.

The formula clearly shows that the acoustic scattering increases with temperature. The acoustic scattering rates as a function of energy within the Γ minimum of the conduction band in both zincblende and wurtzite GaN are shown in figure 2.5. The energy dependence is of the form $E^{1/2}$ corresponding to the three dimensional electronic density of states function. It is apparent that in the wurtzite GaN structure the deformation scattering rate is slightly larger than zincblende due to the lower sound velocity and higher Γ-valley effective mass. In common with other III-V materials deformation potential scattering can be expected to be the dominant lattice scattering mechanism at low temperatures.
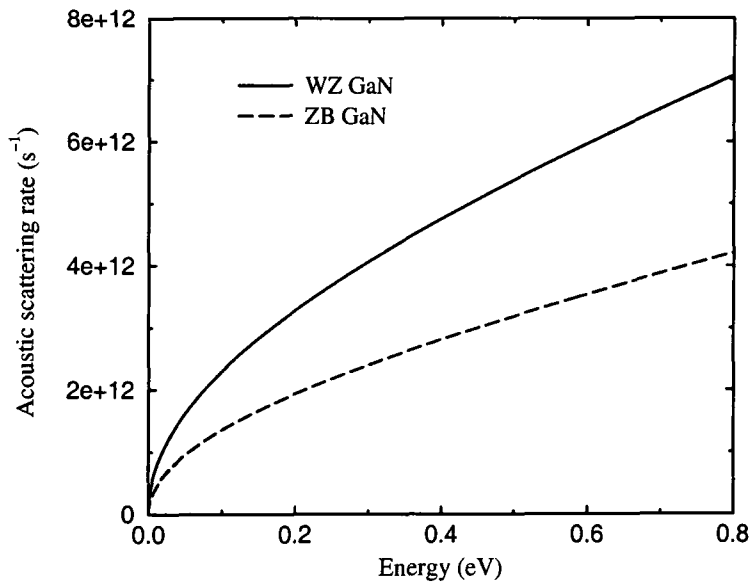
Figure 2.5: Energy dependence of the deformation scattering rate in the Γ valley of zincblende and wurtzite GaN at 300 K.

2. **Piezoelectric scattering:**

The second type of electron scattering by acoustic modes occurs when the displacements of the atoms create an electric field through the piezoelectric effect. This can occur in the compound semiconductors such as the III-V and II-VI materials including GaN, which in fact has a relatively large piezoelectric constant. The piezoelectric scattering rate for an electron of energy E in an isotropic, parabolic band has been discussed by Ridley [42] who included the modification of the Coulomb potential due to free carrier screening. The screened Coulomb potential is written as

$$V(\mathbf{r}) = \frac{e^2}{4\pi\epsilon_0\epsilon_s} \frac{\exp(-q_0\mathbf{r})}{\mathbf{r}} \tag{2.13}$$

where ϵ_s is the relative permittivity constant of the material and q_0 is the inverse screening length, which under non-degenerate conditions is given by

$$q_0^2 = \frac{ne^2}{\epsilon_0\epsilon_s k_B T} \tag{2.14}$$

where n is the electron density. The expression for the scattering rate of an electron in a non-parabolic band structure retaining only the important terms can be written as

$$R_{pz}(\mathbf{k}) = \frac{\sqrt{m^*}e^2 K_{av}^2 k_B T}{4\sqrt{2}\pi\hbar^2\epsilon_0\epsilon_s}\gamma^{-1/2}(E)(1+2\alpha E)^2 \times$$
$$\left\{\ln(1+\frac{8m^*\gamma(E)}{\hbar^2 q_0^2}) - \frac{1}{1+\hbar^2 q_0^2/8m^*\gamma(E)} + (\frac{\sqrt{2}\alpha E}{1+2\alpha E})^2\right\}(2.15)$$

where K_{av} is the dimensionless so called average electromechanical coupling constant [42]. Figure 2.6 shows the piezoelectric scattering rates at room temperature for electrons in the Γ valley of zincblende and wurtzite GaN. Assuming both structures have the same piezoelectric constant equal to 0.375 Cm^{-2}, the higher piezoelectric scattering rate in wurtzite GaN is due to the higher Γ valley effective mass in comparison to zincblende GaN. The piezoelectric constant for GaN is large by the standards of the more familiar III-V materials and such scattering can be expected to have a significant influence on the low field mobility below room temperature [44].
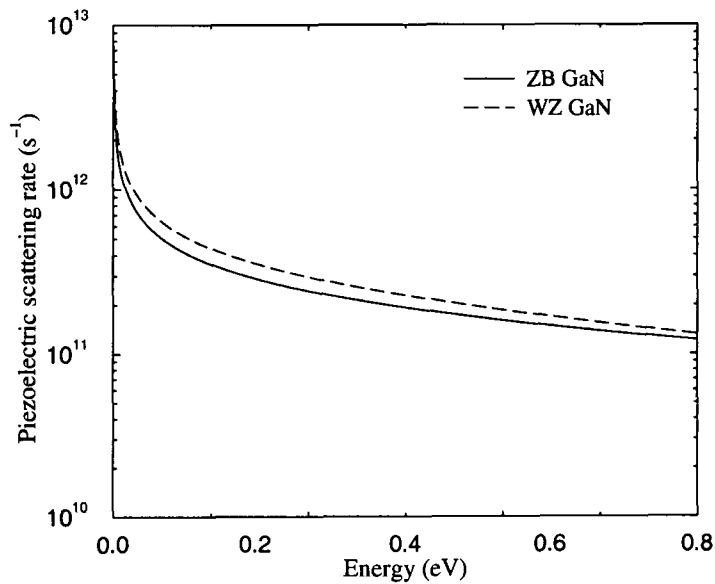
Figure 2.6: Energy dependence of the piezoelectric scattering rate in the Γ valley of zincblende and wurtzite GaN at 300 K.

2.3.4 Intravalley scattering due to optical phonons

Optical lattice vibrations cause neighbouring atoms to vibrate in antiphase. The scattering of electrons by optical phonons occurs by lattice deformation or polar effects.

1. **Polar optical phonon scattering**

   The dipolar electric field arising from the opposite displacement of the negatively and positively charged atoms provides a coupling between the electrons and the lattice which results in electron scattering. This type of scattering is called polar optical phonon scattering and at room temperature is generally the most important scattering mechanism for electrons in III-V semiconductors, and this is also the case in GaN [44] despite the fact that the optical phonon energy is particularly high at ~ 99 meV which suppresses the phonon population and also electrons must reach that energy before phonon emission is possible. The scattering rate due to this process for an electron of energy E in an isotropic, non-parabolic band is [40]

   $$R_{po}(\mathbf{k}) = \frac{\sqrt{2m^*}e^2\omega_{op}}{8\pi\epsilon_0\hbar}(\frac{1}{\epsilon_\infty} - \frac{1}{\epsilon_s})\frac{1+2\alpha E'}{\gamma^{1/2}(E)}F_0(E, E')\left\{ \begin{array}{c} N_{op} \\ N_{op}+1 \end{array} \right\} \quad (2.16)$$

where:

$$\begin{aligned} F_0(E, E') &= C^{-1}\left\{A\ln\left|\frac{\gamma(E)^{1/2} + \gamma(E')^{1/2}}{\gamma(E)^{1/2} - \gamma(E')^{1/2}}\right| + B\right\} \\ A &= [2(1+\alpha E)(1+\alpha E') + \alpha(\gamma+\gamma')]^2 \\ B &= -2\alpha\gamma^{1/2}\gamma'^{1/2}[4(1+\alpha E)(1+\alpha E') + \alpha(\gamma+\gamma')] \\ C &= 4(1+\alpha E)(1+\alpha E')(1+2\alpha E)(1+2\alpha E') \quad (2.17) \end{aligned}$$

ϵ_s and ϵ_∞ are defined in table 2.3, N_{op} is the phonon occupation number and the upper and lower cases refer to absorption and emission, respectively. For small electric fields, the phonon population will be very close to equilibrium so that the average number of phonons is given by the Bose-Einstein distribution

$$N_{op} = \frac{1}{\exp(\frac{\hbar\omega_{op}}{k_B T}) - 1} \quad (2.18)$$

where $\hbar\omega_{op}$ is the polar optical phonon energy. The polar optical scattering rate for both phonon emission and absorption is plotted in figure 2.7 for wurtzite GaN (The rate for the zincblende structure is very similar). Optical phonon absorption can take place at any energy but the polar optical phonon emission occurs only when the initial electron energy exceeds the optical phonon energy (0.0995 eV). At the threshold energy the scattering rate rises sharply up to 7×10^{13} s^{-1} and reduces slowly for higher energy, whereas the rate for phonon absorption is lower at 2×10^{12} s^{-1}. This result shows the importance of polar optical phonon emission at high energies and temperatures in the electron transport properties of GaN.
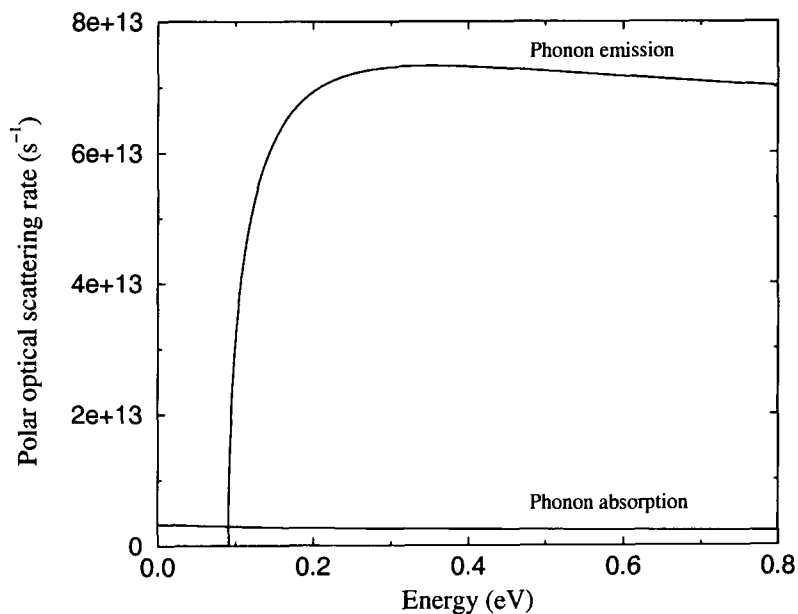
Figure 2.7: Energy dependence of the polar scattering rate in the Γ valley of wurtzite GaN at 300 K.

2. **Non-Polar optical phonon scattering**

Non-polar optical phonon scattering is similar to deformation potential scattering, in that the deformation of the lattice produces a perturbing potential but in this case the deformation is carried by optical vibrations. The non-polar optical

phonon scattering rate in non-parabolic bands is given by [40]

$$R_{npo}(\mathbf{k}) = \frac{D_{od}^2 (m_t^{*2} m_l^*)^{1/2}}{\sqrt{2}\pi\hbar^3 \rho\omega_{op}} (1 + 2\alpha E')\gamma^{1/2}(E') \left\{ \begin{array}{c} N_{op} \\ N_{op} + 1 \end{array} \right\}$$

(2.19)

where D_{od} is the optical deformation potential and $E'=E\pm\hbar\omega_{op}$ is the final state energy phonon absorption (upper case) and emission (lower case).

2.3.5 Intravalley impurity scattering

This scattering process arises as a result of the presence of impurities in a semiconductor. The substitution of an impurity atom on a lattice site will perturb the periodic crystal potential and result in scattering of an electron. Since the mass of the impurity greatly exceeds that of an electron and the impurity is bonded to neighbouring atoms, this scattering is very close to being elastic. Ionized impurity scattering is dominant at low temperatures because, as the thermal velocity of the electrons decreases, the effect of long-range Coulombic interactions on their motion is increased. The electron scattering by ionized impurity centres has been discussed by Brooks-Herring [45] who included the modification of the Coulomb potential due to free carrier screening. The scattering rate for an isotropic, non-parabolic band structure is given by [40]

$$R_{im}(\mathbf{k}) = \frac{8\pi n_i e^4}{k_s^2 \hbar q_0} (m_t^{*2} m_l^*)^{1/2} \gamma^{1/2}(E) \frac{1 + 2\alpha E}{1 + 4\sqrt{2}\gamma(E)(m_t^{*2} m_l^*)^{1/6}/\hbar q_0}$$

(2.20)

where n_i is the impurity concentration, q_0 is the screening length and k_s is the dielectric constant of the material. The ionized impurity scattering rate calculated for electrons in the Γ valley of zincblende and wurtzite GaN with an ionized impurity concentration of 10^{22} m^{-3} is plotted in figure 2.8. It is seen that the scattering rate declines with increasing energy. Ionized impurity scattering is therefore not of importance for very hot electrons. Thus, the scattering of electrons by ionized impurities in GaN is most important at low electric fields and low temperatures, where phonon effects are reduced.
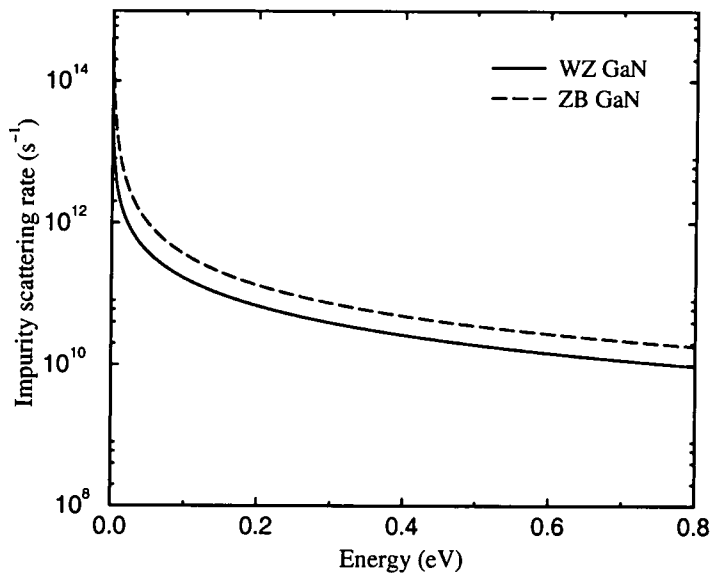
Figure 2.8: Energy dependence of the ionized impurity scattering rate in the Γ valley of zincblende and wurtzite GaN at 300 K.

2.3.6   Intravalley alloy scattering

Alloy scattering refers to the scattering due to the random distribution of the component atoms of the alloy among the available lattice sites. Harrison *et al.* [46] assumed that the alloy crystal potential can be described as a perfectly periodic potential which is then perturbed by the local deviations from this potential, due to the disordering effects in the alloy. Using the Harrison model [46], the scattering rate due to the chemical disorder in a ternary alloy of electrons in a non-parabolic band is given by

$$R_{alloy}(\mathbf{k}) = \frac{4\sqrt{2}\pi m^{*3/2} r_0^6}{9\hbar^4} \frac{x(1-x)(\Delta U)^2}{\Omega^2} \gamma^{1/2}(E)(1+2\alpha E) \qquad (2.21)$$

where x denotes the molar fraction of one of the binary components of the alloy, Ω is the volume of the primitive cell and ΔU is the spherical scattering potential, defined as

$$V(r) = \begin{cases} \Delta U & r \leq r_o \\ 0 & r > r_o \end{cases} \qquad (2.22)$$

where r_0 defines the extent of the scattering potential and ΔU is normally taken as the difference in energy band gaps for the two components of the alloy.

2.3.7 Intervalley scattering due to optical phonons

The constant energy surfaces for the conduction band of GaN derive from several valleys. Thus, under the application of high electric field, electrons can be scattered from an initial state in a certain valley to a final state in a non-equivalent valley. For example, in wurtzite GaN this process occurs when an electron in the Γ valley is heated and is able to transfer to the higher Γ_3, U, K and M valleys. In the case of Γ to zone edge valley scattering the process involves a substantial change of electron wavevector. Acoustic and optical phonons of sufficiently large wavevector can effect the transition but in view of the large wavevectors involved it is normal to treat all processes like deformation scattering by optical phonons. Then the total nonequivalent intervalley scattering rate from a state $\mathbf{k}$ in a certain valley to a set of Z_f different valleys is given by [40]

$$R_{equiv}(\mathbf{k}) = \frac{(D_t K)_i^2 Z_f (m_t^{*2} m_l^*)^{1/2}}{\sqrt{2} \pi \rho \omega_{op} \hbar^3} (\varepsilon \pm \hbar \omega_{op} - \Delta \varepsilon_{fi})^{1/2} \times$$

$$[1 + 2\alpha(\varepsilon \pm \hbar \omega_{op} - \Delta \varepsilon_{fi})] \left\{ \begin{array}{c} N_{op} \\ N_{op} + 1 \end{array} \right\} \qquad (2.23)$$

where $\hbar \omega_{op}$ is the optical phonon energy and $\Delta \varepsilon_{fi}$ is the difference between the energies of the bottoms of the final and initial valleys. $(D_t K)_i$ is the coupling constant, which depends on the initial and final valleys and the branch of phonons involved in the transition. N_{op} is the phonon occupation number, with the upper and lower cases corresponding to phonon absorption and emission, respectively.

The nonequivalent intervalley scattering rate as a function of energy for scattering from the Γ_1 minimum to the higher zone edge valleys in wurtzite GaN is plotted in figure 2.9 for both phonon emission and absorption.
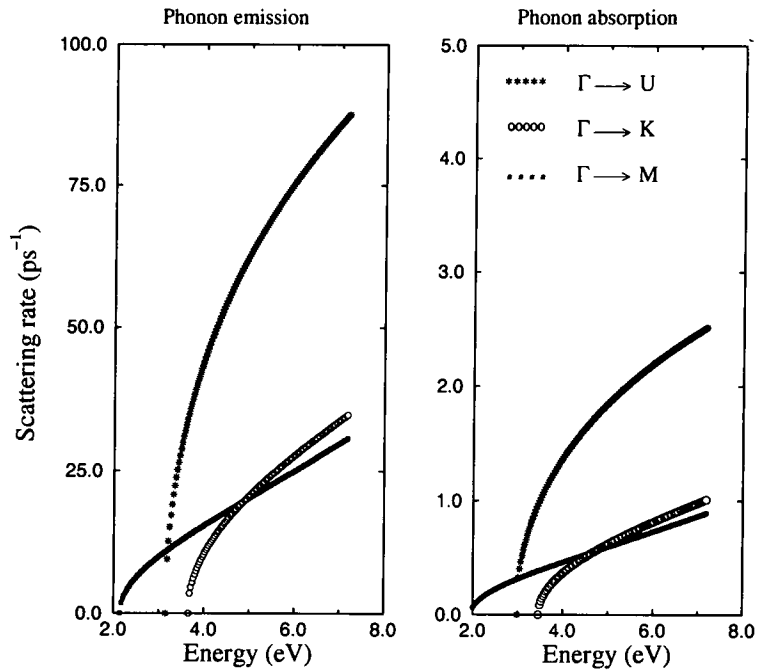
Figure 2.9: Energy dependence of the non-polar optical intervalley scattering rate in the Γ valley of wurtzite GaN at 300 K.

The electrons can also be scattered between valleys of the same type which is called equivalent intervalley scattering. The rate is given by equation 2.23.

Chapter 3

Low and High Field Transport Calculations for Bulk GaN

3.1 Introduction

To carry out calculations of the electronic transport properties of GaN it is necessary to solve the Boltzmann transport equation. There are many different techniques for the solution of the Boltzmann equation and here we have used the iterative method of Rode to determine electron transport properties of bulk GaN in the wurtzite and zincblende phases [47, 48] when the applied field is sufficiently low. The use of numerical iteration to solve the Boltzmann equation has been described and reviewed elsewhere [49–51] and therefore only a brief general summary of the basic features is given in this chapter. However, in more general cases the Boltzmann transport equation is often exceedingly difficult to solve directly. By contrast, it is relatively easy, although computionally intensive, to simulate the trajectories of individual carriers as they move through a semiconductor under the influence of the applied field and the random scattering processes. Indeed, much of our understanding of high field transport in bulk semiconductors and in devices has been obtained through the use of such a method, Monte Carlo simulation. The Monte Carlo method allows the Boltzmann transport equation to be solved using a statistical numerical approach, by following the transport history of one or more carriers (particles), subject to the action of external

forces, such as an applied electric field, and the intrinsic scattering mechanisms. Here, we have used the technique to study high field electronic transport properties in bulk GaN, and other nitride semiconductors, and devices fabricated from them. There are many reviews of the Monte Carlo method giving a detailed description of its application to semiconductors [52–54]. Therefore, only an outline of the basic features are reviewed in this chapter.

Section 3.2 presents a review of the iterative method and shows the results obtained from the iterative solution of the Boltzmann equation for low field transport in zincblende and wurtzite GaN. In order to provide a comparison with a material whose properties are well known, calculations have also been carried out for GaAs, and comparisons of the electron mobilities of the two materials at low fields as a function of temperature and electron concentration are given. Section 3.3 gives a short introduction to the Monte Carlo method, and results from it are described in sections 3.4 and 3.5 for high field electron transport in bulk zincblende and wurtzite GaN, and in two other commonly studied group-III nitrides (AlN and InN). We finish this chapter with section 3.6 which is a brief summary of the main points of interest and the conclusions drawn.

3.2   General features of the iterative model

In principle the iterative and Monte Carlo techniques give exact numerical predictions of electron transport phenomena in bulk semiconductors. Both of them can include the details of the microscopic electronic processes and can be extended to time-dependent phenomena. In low electric fields the effects of scattering, which depend on the details of the distribution function, can be dealt with more conveniently by the iterative technique because it processes the whole distribution function at each step of the procedure. In contrast the Monte Carlo method is highly susceptible to statistic fluctuations in the ensemble when the departure from equilibrium is small because of the weakness of the electric field effects. For these reasons, we used the iterative method to determine the low field electron mobility in bulk GaN.

Rode's iterative technique provides a compact method of solution of the Boltzmann equation in the low field regime. The Boltzmann transport equation for the distribution function $f(\mathbf{r}, \mathbf{k}, t)$ is

$$\frac{\partial f}{\partial t} + \mathbf{v}.\nabla_r f + \frac{e\mathbf{F}}{\hbar} \cdot \nabla_k f = (\frac{\partial f}{\partial t})_{coll} \tag{3.1}$$

where $(\frac{\partial f}{\partial t})_{coll}$ represents the change of distribution function due to the electron scattering. In the steady-state and under application of a uniform electric field the Boltzmann equation can be written as

$$\frac{e\mathbf{F}}{\hbar} \cdot \nabla_k f = (\frac{\partial f}{\partial t})_{coll} \tag{3.2}$$

Consider electrons in an isotropic, non-parabolic conduction band whose equilibrium Fermi distribution function is $f_0(k)$ in the absence of electric field. Note the equilibrium distribution $f_0(k)$ is isotropic in $\mathbf{k}$ space but is perturbed when an electric field is applied. If the electric field is small, we can treat the change from the equilibrium distribution function as a perturbation which is first order in the electric field. The distribution in the presence of a sufficiently small field can be written quite generally as

$$f(\mathbf{k}) = f_0(k) + f_1(k) \cos \theta \tag{3.3}$$

where θ is the angle between $\mathbf{k}$ and $\mathbf{F}$ and $f_1(k)$ is an isotropic function of $\mathbf{k}$, which is proportional to the magnitude of the electric field. $f(\mathbf{k})$ satisfies the Boltzmann equation 3.2 and it follows that

$$\frac{eF \cos \theta}{\hbar} \frac{\partial f_0}{\partial k} = \sum_i \left\{ \int \cos \theta' f_1'[s_i'(1 - f_0) + s_i f_0] d^3 k' - f_1 \cos \theta \int [s_i(1 - f_0') + s_i' f_0'] d^3 k' \right\} \tag{3.4}$$

where the sum is over scattering processes i. For a more compact notation we have written $f(\mathbf{k}') = f'$, $s_i(\mathbf{k}, \mathbf{k}') = s_i$ and $s_i(\mathbf{k}', \mathbf{k}) = s_i'$. $s_i(\mathbf{k}, \mathbf{k}') = s_i$ is the probability for scattering out of state $\mathbf{k}$ into the differential element $d^3 k'$ at $\mathbf{k}'$. For the isotropic conduction band $s_i(\mathbf{k}, \mathbf{k}')$ depends on only $\mathbf{k}$, $\mathbf{k}'$ and the cosine of the angle ϕ between them, and the relation [47]

$$\int \cos \theta' A(\cos \phi) d^3 k' = \cos \theta \int \cos \phi A(\cos \phi) d^3 k' \tag{3.5}$$

may be used to manipulate equation 3.4. Here $A(\cos\phi)$ is an arbitrary function of $\cos\phi$ but does not otherwise depend on θ and θ'. From equation 3.2 and 3.3 we obtain

$$\frac{eF}{\hbar}\frac{\partial f_0}{\partial k} = \sum_i \left\{ \int \cos\phi f_1'[s_i'(1-f_0) + s_if_0]d^3k' - f_1\int[s_i(1-f_0') + s_i'f_0']d^3k' \right\} \quad (3.6)$$

In general there will be both elastic and inelastic scattering processes. For example impurity scattering is elastic and acoustic and piezoelectric scattering are elastic to a good approximation at room temperature. However, polar and non-polar optical phonon scattering are inelastic. Labelling the elastic and inelastic scattering rates with subscripts el and $inel$ respectively and recognising that, for any process i, $s_{eli}(\mathbf{k}',\mathbf{k})=s_{eli}(\mathbf{k},\mathbf{k}')$ equation (3.6) can be written as

$$f_1(k) = \frac{(-eF/\hbar)(\partial f_0/\partial k) + \sum_j \int \cos\phi f_1'[s_{inelj}'(1-f_0) + s_{inelj}f_0]d^3k'}{\sum_i \int(1-\cos\phi)s_{eli}d^3k' + \sum_j \int[s_{inelj}(1-f_0') + s_{inelj}'f_0']d^3k'} \quad (3.7)$$

Note the first term in the denominator is simply the momentum relaxation rate for elastic scattering. Equation 3.7 may be solved iteratively by the relation

$$f_1(k)[n] = \frac{(-eF/\hbar)(\partial f_0/\partial k) + \sum_j \int \cos\phi f_1(k')[n-1][s_{inelj}'(1-f_0) + s_{inelj}f_0]d^3k'}{\sum_i \int(1-\cos\phi)s_{eli}d^3k' + \sum_j \int[s_{inelj}(1-f_0') + s_{inelj}'f_0']d^3k'}$$
$$(3.8)$$

where $f_1(k)[n]$ is the perturbation to the distribution function after the n-th iteration. It is interesting to note that if the initial distribution is chosen to be the equilibrium distribution, for which $f_1(k)$ is equal to zero, we get the relaxation time approximation result after the first iteration. We have found that convergence can normally be achieved after only a few iterations for small electric fields. Once $f_1(k)$ has been evaluated to the required accuracy, it is possible to calculate quantities such as the drift mobility μ, which is given by

$$\mu = \frac{\int \mathbf{v}.\mathbf{F}f(\mathbf{k})d^3k}{F^2\int f(\mathbf{k})d^3k} \quad (3.9)$$

In terms of spherical coordinates

$$\mu = \frac{\int_0^\infty vk^2(f_1/F)dk}{3\int_0^\infty k^2 f_0 dk} \quad (3.10)$$

The Kane approximation relation between electron group velocity and effective mass m^* in a non-parabolic band is

$$v(k) = \frac{\hbar k}{m^*}\frac{1}{(1+2\alpha E)} \quad (3.11)$$

and substituting this result in equation (3.10) we find that

$$\mu = \frac{\hbar}{3m^*F} \frac{\int_0^\infty (k^3/1 + 2\alpha E)f_1 dk}{\int_0^\infty k^2 f_0 dk} \tag{3.12}$$

Here, we have calculated low field drift mobility in GaN structures using the iterative technique. The effects of piezoelectric, acoustic deformation, polar optical phonons and ionized impurity scattering which were described in chapter 1 have been included in the model. It is also assumed that the electrons remain in the Γ-valley of the Brillouin zone. The valley is isotropic in the case of zincblende GaN and approximated as such for the wurtzite crystal structure.

3.2.1 Low-field transport results in bulk GaN

Figure 3.1 shows the calculated electron drift mobilities versus temperature and donor concentration for zincblende and wurtzite GaN. The electron drift mobilities at room temperature that we find are 1300 and 900 cm^{2}V^{-1}s^{-1} for zincblende and wurtzite structures, respectively, for an electric field equal to 10^4 Vm^{-1} and with a donor concentration of 10^{22} m^{-3}. The material parameters used to calculate the electron drift mobilities are tabulated in table 2.3. For the wurtzite crystal structure it is assumed that the conduction band is isotropic with an effective mass 0.2 m_0. This is a reasonable approximation since m_l^* and m_t^* differ by only 10%.

The results plotted in figure 3.1a indicate that the electron drift mobility of wurtzite GaN is lower than that for the zincblende structure at all temperatures. This is largely due to the higher Γ valley effective mass in the wurtzite phase. Figure 3.1b shows the calculated variation of the electron mobility as a function of the donor concentration for both GaN crystal structures at room temperature. The mobility does not vary monotonically between donor concentrations of 10^{21} and 10^{25} m^{-3} due to the dependence of electron scattering on donor concentration, but shows a maximum near 10^{21} m^{-3} for zincblende and wurtzite. The dependence of mobility on donor concentration calculated here is similar to that found by Dhar et al [55].

In order to understand the scattering mechanisms which limit the mobility of GaN under various conditions, we have performed calculations of the electron drift mobility
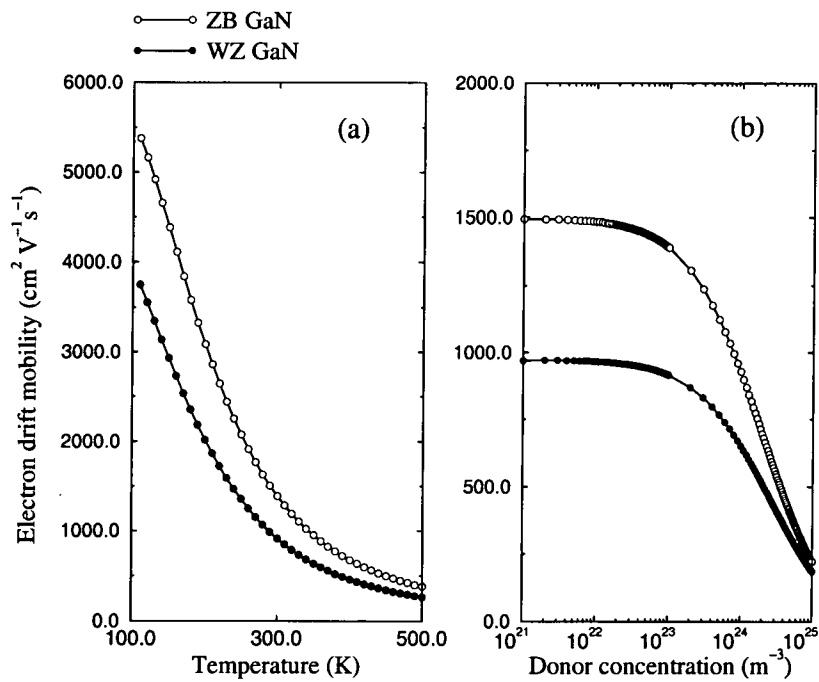
Figure 3.1: (a) Electron drift mobility of GaN in zincblende and wurtzite structures versus temperature. Donor concentration is approximately 10^{22} m^{-3}, (b) Electron drift mobility of GaN in zincblende and wurtzite structures versus donor concentration at room temperature.

when particular scattering processes are ignored. The solid curve in figure 3.2 shows the calculated mobility for wurtzite GaN including all scattering mechanisms whereas the dashed, dotted, and open circle curves show the calculated mobility without ionized impurity, piezoelectric and polar optical scattering, respectively. It can be seen that below 300 K the ionized impurity scattering is dominant while at the higher temperatures electron scattering is predominantly by optical modes. Thus the marked reduction in mobility at low temperatures seen in figure 3.2 can be ascribed to impurity scattering and that at high temperatures to polar optical phonon scattering. In figure 3.2 the mobility in the absence of band non-parabolicity is plotted as a dash-dot curve. Non-parabolicity leads to approximately a 10% reduction relative to the mobility for parabolic band at room temperature. This is because non-parabolicity increases the electron effective mass and also the scattering rates through the density of states.
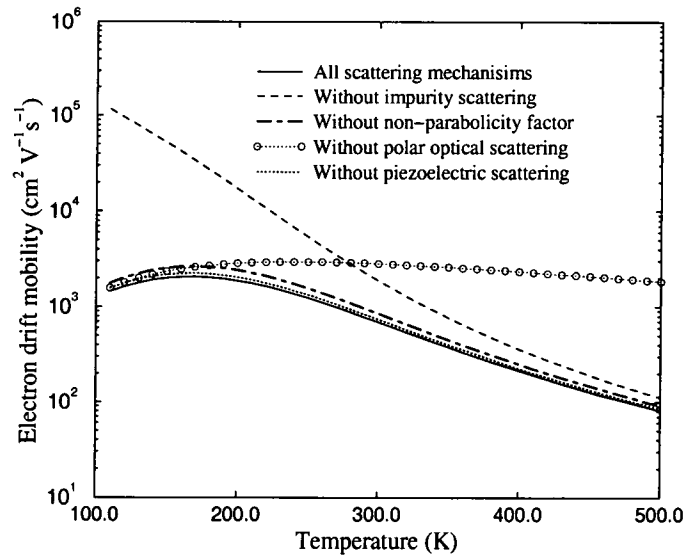
Figure 3.2: Comparison of electron drift mobility in wurtzite GaN with donor concentration of 10^{24} m^{-3} and when individual scattering processes are ignored. The effect of Γ-valley non-parabolicity is also shown.

The temperature variation of the electron drift mobility in zincblende and wurtzite GaN for different donor concentrations is shown in figure 3.3. It is evident from this figure that the curves approach each other at very high temperatures, where the mobility is limited by longitudinal optical phonon scattering, whereas the mobility varies inversely with donor concentration at low temperatures as we would expect from the foregoing discussion.

Finally, we compare the drift mobility characteristics of GaAs, as shown in figure 3.4 with those of GaN. The drift mobility characteristics of the two materials show similar trends, reflecting the fact that both materials are direct-gap compound semiconductors [49]. However, the mobility in GaAs is 7200 cm^{2}V^{-1}s^{-1} at 300 K, some 5 times greater than for zincblende GaN. This is a consequence of the smaller Γ-valley effective mass, 0.068 m_0 (versus 0.15 m_0 in zincblende GaN) and small polar optical phonon energy 0.036 eV in GaAs (versus 0.099 eV in zincblende GaN).
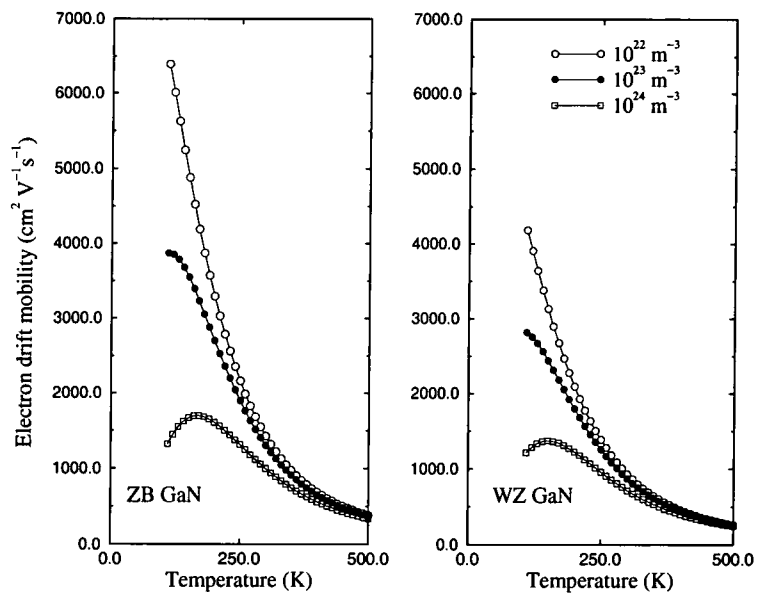
Figure 3.3: Calculated low-field electron drift mobility of zincblende and wurtzite GaN as functions of temperature for different donor concentrations.
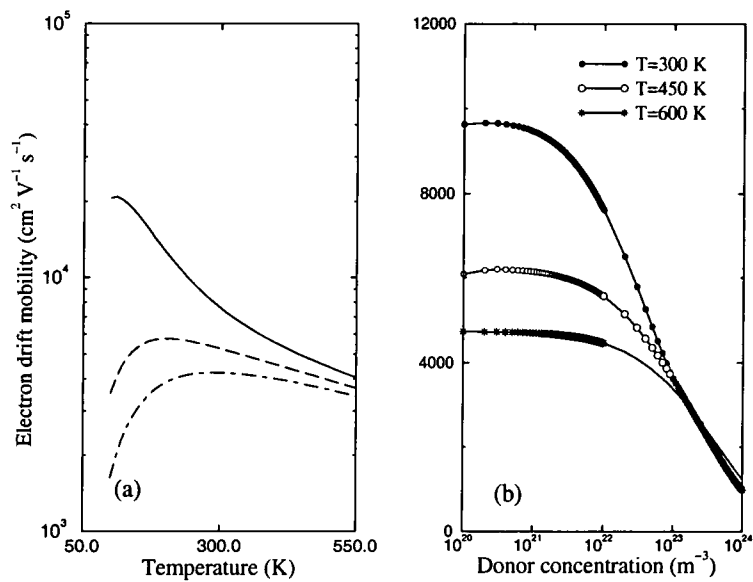
Figure 3.4: (a) Electron drift mobility of GaAs versus temperature for different donor concentrations. The solid, long-dashed and dot-dashed lines represent the results for 10^{22}, 5×10^{22} and 10^{23} m^{-3}, respectively, (b) Electron drift mobility of GaAs versus donor concentration at different temperatures.

3.3 Monte Carlo method

The Monte Carlo method is a general numerical technique for simulating or applying random processes but here we are exclusively concerned with its application to the solution of the Boltzmann equation in the theory of electron transport in bulk materials and devices. Our Monte Carlo transport calculations consist of the computer simulation of the motion of electrons in two-dimensional real space (x, y) and in three-dimensional reciprocal space (k_x, k_y, k_z) as a free flight that is interrupted by scattering events [52, 54]. Between collisions, the electron dynamics is determined by the electronic band structure and the local electric field through the semi-classical laws of motion. The collisions are regarded as random events whose probabilities are known functions of the electron's energy band and wavevector, as predicted by the quantum theory of solids. The duration of a free flight, the type of scattering process, and the change in band and wavevector resulting from scattering are determined using pseudorandomly generated numbers.

Consider, the simulation of the dynamics of a single electron in a homogeneous bulk semiconductor. During the free flight an electron's response to the electric field it experiences is described by the semiclassical equation

$$\hbar \frac{d\mathbf{k}}{dt} = -e\mathbf{E} \tag{3.13}$$

where $\mathbf{k}$ is the electron wavevector and $\mathbf{E}$ is the external electric field. In the simulation, the free flight time between two successive scattering events is chosen stochastically so that the distribution of times corresponds to that predicted by microscopic theory. If the total scattering rate for an electron with wavevector $\mathbf{k}(t)$ is known to be $\Gamma[\mathbf{k}(t)]$, the probability that an electron that was scattered at time t will suffer its next scattering in time interval t and $t+dt$ is

$$p(t)dt = \Gamma[\mathbf{k}(t)]e^{-\int_0^t \Gamma[\mathbf{k}(t')]\,dt'}\,dt \tag{3.14}$$

Free flight times can be chosen with the distribution of equation 3.14 by generating random numbers with a uniform distribution between 0 and 1. To see this, consider

choosing a time t_r by generating a random number r and solving the equation

$$\int_0^{t_r} p(t)dt = r \tag{3.15}$$

for t_r. The probability that the random number lies in the interval r, $r+dr$ is simply dr. It is also equal to the probability that the upper limit of the integral in equation 3.15 lies in the interval t_r, $t_r + dt_r$, where dt_r is defined by

$$\int_0^{t_r+dt_r} p(t)dt = r + dr \tag{3.16}$$

If we denote that probability by $P(t_r)dt_r$, it follows that

$$P(t_r)dt_r = dr \tag{3.17}$$

and

$$P(t_r) = \frac{dr}{dt_r} = p(t_r) \tag{3.18}$$

where we have used equation 3.15 to obtain the last equality. Thus, the probability of obtaining a particular t_r by the above procedure is just the distribution of free flight times $p(t_r)$. Therefore, in principle, we can generate free flight times with the correct distribution by generating random numbers r and solving equation 3.14 for t_r.

However, the total scattering rate is dependent on the electron wavevector and the above selection procedure for free flight times requires the numerical solution of an integral equation for each scattering event, which can be complicated and time consuming. In order to simplify the determination of the free flight time, self-scattering can be introduced. In a self-scattering process neither the wavevector nor the energy of the electron is changed. However, the self-scattering can be chosen so that the total scattering rate is constant for all wavevectors, and $p(t)$ has the form

$$p(t) = \Gamma e^{-\Gamma t} \tag{3.19}$$

Now using equation 3.15

$$\int_0^{t_r} \Gamma e^{-\Gamma t}dt = r \tag{3.20}$$

and it follows that

$$t_r = -\frac{1}{\Gamma}\ln(1 - r) \tag{3.21}$$

which is also equivalent to

$$t_r = -\frac{1}{\Gamma} \ln r \tag{3.22}$$

since r is uniformly distributed between 0 and 1.

After a free flight of duration t the position and wavevector of an electron in a parabolic band are given by

$$
\begin{aligned}
\mathbf{r} &= \mathbf{r}_0 + \hbar\mathbf{k}_0/m^* - e/m^* \int_0^t dt' \int_0^{t'} dt'' \mathbf{E}(t'') \\
\mathbf{k} &= \mathbf{k}_0 - e/\hbar \int_0^t dt' \mathbf{E}(t')
\end{aligned}
\tag{3.23}
$$

where $\mathbf{r}_0$ and $\mathbf{k}_0$ are the position and wavevector of the electron immediately after the last scattering event, taken to be a time $t = 0$. Thus at the end of each free flight, all electrons will have a new state in reciprocal space and a new position in real space.

The selection of the new wavevector and its components depend on the choice of a scattering mechanism at the end of a free flight. A scattering process can be selected using a random number. Each scattering mechanism has a probability of occurrence that is a function of the carrier energy and the probabilities for the different mechanisms can be assigned to numerical intervals between 0 and 1. Random numbers can then be used to select the scattering mechanism. The scattering processes are either elastic or involve the gain or loss of a definite amount of energy by the carrier. In the case of spherical bands, the magnitude of the electron wavevector after scattering is defined by the initial wavevector and the energy change. The angular dependence in k-space of the particular scattering process can then be selected by the use of uniformly distributed random numbers. In the case of ellipsoidal valleys it is convenient to carry out a so called Herring-Vogt transformation [40] of k-space so that the constant energy surfaces are reduced to spheres and the methods described for spherical bands above may be applied.

Figure 3.5 shows the main steps in a Monte Carlo simulation of a single electron. A carrier is initialized by selecting its three components of momentum from a Maxwellian distribution for the lattice temperature T. The carrier then accelerates freely under the applied electric field until it is determined that scattering has occured. This determination is based on the total scattering rate as a function of carrier state and on a
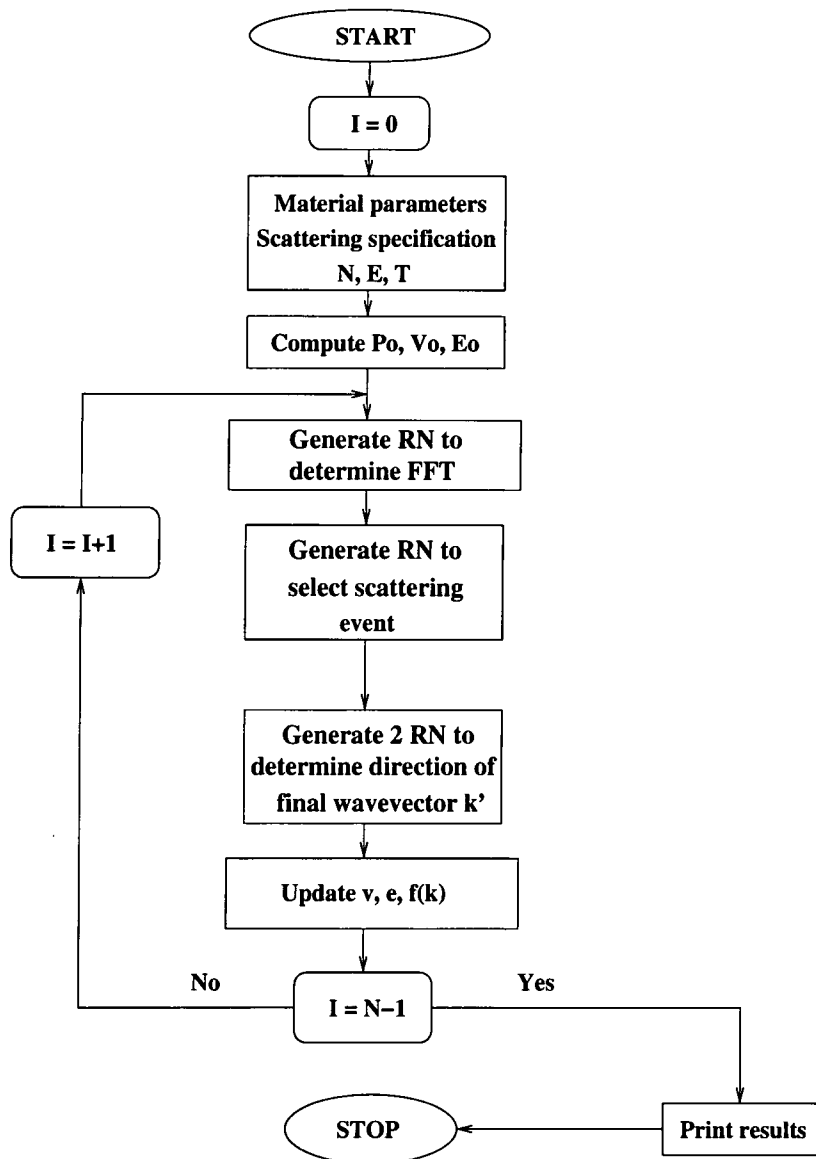
Figure 3.5: Flowchart for a Monte Carlo simulation. I, number of iteration completed; N, number of interactions specified; RN, random number; FFT, free flight time; E, electric field; e, energy; P, momentum; v, velocity; T, temperature; **k**, electron wavevector and $f(\mathbf{k})$ carrier distribution function.

pseudorandom number selected at the beginning of the free flight as described earlier. At the end of the flight another pseudorandom number is selected, which determines which of the various possible scattering processes has occurred. Once a scattering mechanism has been selected, additional pseudorandom numbers determine the initial state of the carrier for the next free flight. These steps are repeated until a specified number of interactions have occurred or until a specified time has elapsed.

We may also simulate the dynamics of several electrons in an inhomogeneous system, such as an electronic device. The electric field experienced by any electron is the resultant of the applied field and the field due to any space charge created by the other electrons, holes and fixed impurity charge centres in the semiconductor. The redistribution of electrons described above changes the electric field in the system, which can be calculated by solving Poisson's equation, taking account of the boundary conditions at the electrodes and device surfaces. The calculation loop of electron free flight, scattering and solution of Poisson's equation must be repeated iteratively for many timesteps until the steady-state flow of electrons is reached.

The exact choice of the Monte Carlo simulation scheme is largely governed by the nature of the problem. For example whether the need is to simulate steady-state or transient phenomena and whether or not the sample in question is inhomogeneous. Steady-state, homogeneous transport may be modelled using a single particle simulation, whereas time and space-dependent phenomena generally require simulation of the motion of a large number of particles simultaneously. The latter is the case in the application of Monte Carlo algorithms to the study of semiconductor devices as described in detail in a number of textbooks and reviews [75, 76]. In summary we may consider Monte Carlo simulations to fall into three main types:

1. **One particle Monte Carlo simulation**

   It is assumed that the electric field is known and then the dynamics of a single particle is followed in time. In the steady-state, the time-averaged behaviour of the simulated particle can be used to predict the properties of a many particle system when the transport history over a long time is representative of the behaviour of all other particles in the system.

2. **Ensemble Monte Carlo simulation**

   The dynamics of a large number of particles is simultaneously simulated with an assumed field. The properties of the ensemble at any given time, including distribution functions and ensemble averages, can be used to predict the time-dependent properties of a many particle system in which the field is constant in time.

3. **Self-consistent ensemble Monte Carlo simulation**

   An ensemble Monte Carlo simulation is carried out in which the particles move in a spatially varying electric field that is determined self-consistently as a function of time from the solution of Poisson's equation for the instantaneous particle distribution.

3.3.1 Device simulation model

We have used the self-consistent ensemble Monte Carlo method for the simulation of GaN devices. Our model is based on SLURPS (Software Library for Universal Random Particle Simulations), which has been developed at the University of Durham in recent years to model a wide range of electronic devices. In this project the capabilities of SLURPS have been developed further to make possible simulation of electronic transport in nitride semiconductors (such as GaN, AlN, InN and their alloys) in the wurtzite phase and devices based on them. In particular, a five-valley model of the conduction band of a wurtzite semiconductor has been introduced into SLURPS. In addition, the polarization charges resulting from the piezoelectric effect in strained layers, and the effects of electron trapping in nitride materials have been included.

SLURPS comprises a library of routines, each of which is designed to perform a specific task in the simulation, such as drifting the particles, scattering rate calculations, specifying charge distributions, solving Poisson's equation, etc. In order to describe all these effects accurately, it is necessary to have a knowledge of the device geometry and dimensions, the band structure of the material used and other physical constants that are necessary for calculating the rates for the relevant carrier scattering mechanisms.

The geometry of the device to be simulated is specified at the beginning of the
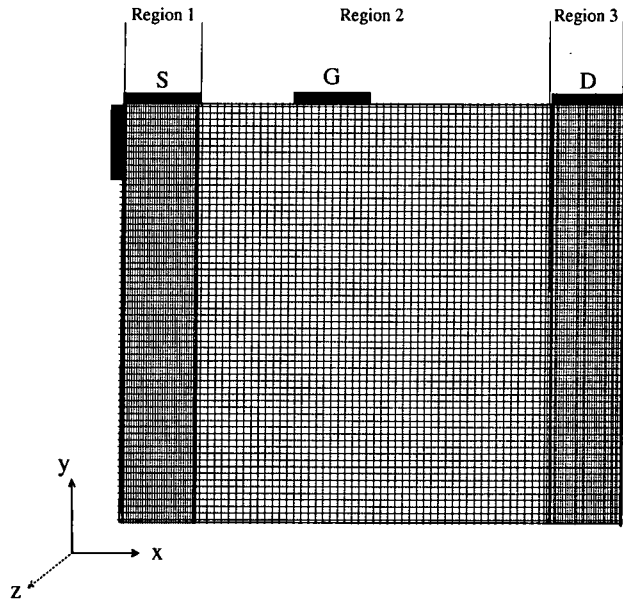
Figure 3.6: Device geometry and discretization of a MESFET. There
are three regions and three contacts S, G and D. The mesh cells are
uniform within any single region and match at the joins.

simulation by defining it in an $x - y$ plane as a set of joined rectangular regions, each
with uniform doping and other material parameters, and a set of contact regions. All
physical quantities are assumed constant in the z direction (device width). Figure
3.6 shows a simple example of joined rectangular regions and contacts for a MESFET
structure. The solution of Poisson's equation is based on a finite difference method
which requires that all the rectangular regions of the device are divided into uniform
arrays of two-dimensional mesh cells. The cells may differ in form from region to region
but it is necessary that they match in size along the join between two adjacent regions.
In figure 3.6 the rectangular regions 1 and 3 have identical uniform mesh cells which
are different from those in region 2, but match at the joins. The cells also form the
frame of reference in which the particles move under the influence of the electric field.
The definition of the mesh (shape and size of the cells) is dependent on the details of
the device and the simulation, since, for example, the resolution of the electric field is
limited by the size of the mesh cells.

After setting all the material and device parameters, the simulation is started

in a state of charge neutrality everywhere in the device. The simulated particles are distributed appropriately among all the mesh cells to achieve the required neutrality. Because the number of electrons in a real device (n) is normally extremely large it is impossible to simulate the motion of all of them by the Monte Carlo method. Therefore in the self-consistent approach a set of N_{sp} superparticles ($N_{sp} \ll n$) which are intended to be representative of the electrons is considered instead. For the superparticle dynamics to be representative of the electrons, the response of each superparticle to the electric field and scattering interactions must be the same as that of an electron. However, for the purposes of calculating the electric field inside the device and the current flow through the electrodes it is necessary for the total charge of the superparticles to be the same as the total electronic charge. In the two-dimensional device models used here there is no variation of electron density or electric field normal to the $x - y$ plane and the superparticles may be considered to be charge rods extending infinitely in the z-direction. The charge per unit length of the charge rods is then taken as

$$q_{sp} = -en/N_{sp}W \qquad (3.24)$$

where W is the device width. It then follows that the total superparticle charge in a range of z equal to the device width is the same as the total electronic charge within the real device.

Initially, all the superparticles in the device are made to occupy the lowest conduction band valley of the constituent semiconductor and are assigned wavevectors corresponding to a Maxwellian distribution. The superparticle system is sampled at regular time intervals (typically 1 femtosecond) and the charge within a cell is calculated. The simplest method for assigning charged particles to cells is the nearest-grid-point scheme in which the total charge found in a cell is assigned to the midpoint of that cell (figure 3.7). After each sampling Poisson's equation is solved and the electric field is updated.

Poisson's equation is solved by a combined fast Fourier transform [77–79] and Buneman cyclic reduction [80] method developed by Walmsley and Abram [81]. This calculational scheme is integrated with a capacity matrix approach [82] that facilitates the use of individual rectangular regions to form more complicated structures.

The information on the state of each particle in the simulation may be used to
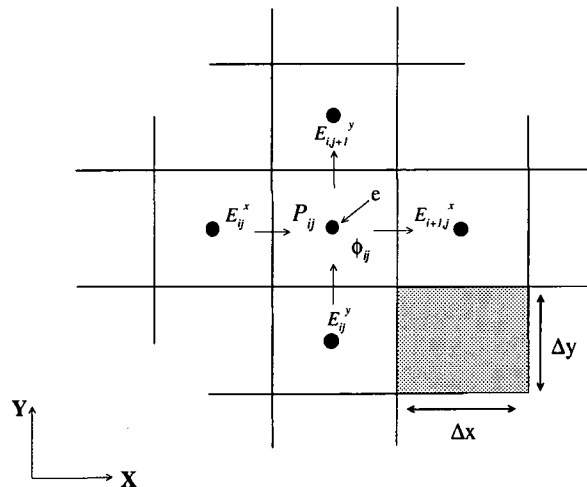
Figure 3.7: Nearest-grid-point method for charge assignment in two-dimensions. The charge density at a mesh point P_{ij} is taken to be the total charge in the mesh cell surrounding the mesh point P_{ij} divided by the cell area. Note discretized electric field E_{ij} and electric potential ϕ_{ij}, $(E = -\nabla\phi)$ are used in the solution of Poisson's equation.

calculate various properties of the ensemble and hence make predictions about the behaviour of a real material or device. For example, ensemble averages of particle velocity or energy may be obtained at a specified time, either for the whole system or for some limited region of space. In the case of a device simulation, the currents at various terminals may also be calculated, in addition to the extraction of microscopic information.

In this way it is possible to study the time-dependent behaviour or transient response of a system. Such results are subject to statistical error due to the limited number of particles used in the simulation. Obviously errors can be reduced by increasing the number of particles, but they can also be reduced when considering the steady-state properties of a system by averaging the relevant data over time.

3.4 High-field simulation in bulk GaN

In this section, we report calculations of the transport properties of zincblende and wurtzite GaN which are relevant to high-power and high-temperature device applications of the materials.

3.4.1 Steady-state drift velocity in bulk GaN structures

Electron drift velocity as a function of electric field is important in determining the performance of high-speed and microwave semiconductor devices. Here we show the results of the steady-state velocity-field characteristics in the zincblende and wurtzite phases of bulk GaN. Steady-state drift velocity, average electron energy and valley occupancy are presented, and the differences between the transport properties of the two phases are discussed. All simulations are for 300 K with an impurity concentration of 10^{22} m^{-3}.

Figure 3.8 shows the simulated velocity-field characteristics of wurtzite and zincblende GaN with the electric field applied along the hexagonal c-axis (wurtzite) or one of the cubic axes (zincblende). The solid circle curves represent simulation results obtained using non-parabolic valleys and the open square curves are for the parabolic band approximation. The difference in the calculated drift velocities between the zincblende and wurtzite phases of GaN can be explained in terms of the band structures of the two phases. The simulations show that the zincblende phase has the higher peak drift velocity of around 2.7×10^5 ms^{-1}, while that for wurtzite is about 2.3×10^5 ms^{-1}. At higher electric fields, intervalley optical phonon emission dominates, causing the drift velocity to decrease and saturate below 2×10^5 ms^{-1} for both phases. The peaks in the characteristics are the result of the onset of significant scattering into the satellite conduction band valleys and the threshold field for this is a function of the intervalley separation and the density of electronic states in the satellite valleys. Inspection of figure 3.8 shows the threshold fields to be 1.5×10^7 and 2.1×10^7 Vm^{-1} for the zincblende and wurtzite phases, respectively. Our drift velocity results for both phases of GaN show good agreement with other Monte Carlo calculations [29, 58, 59]. The values of
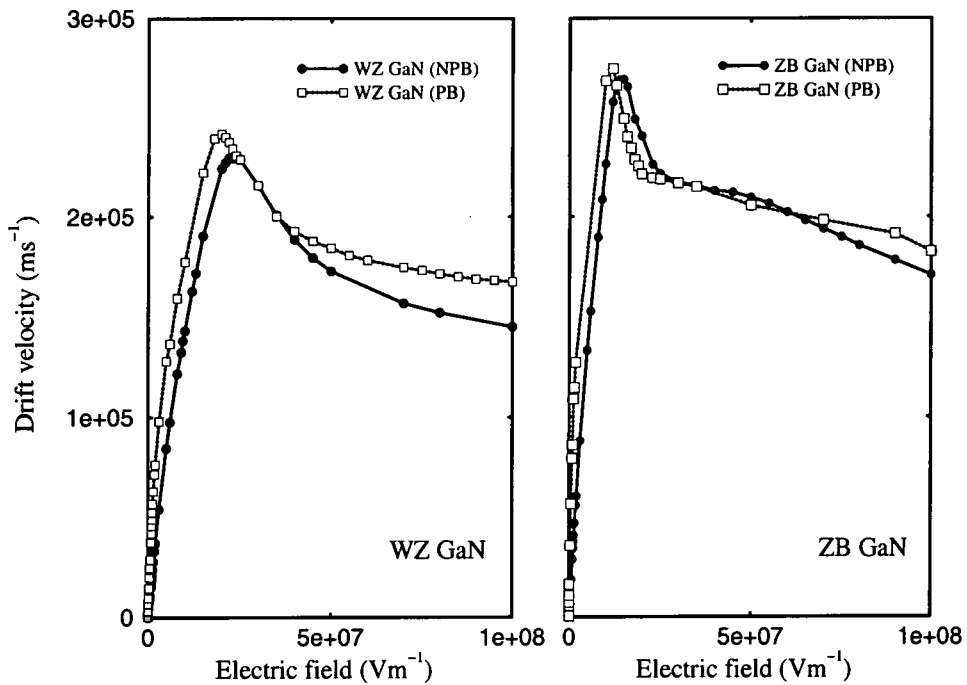
Figure 3.8: Calculated steady-state electron drift velocity in bulk wurtzite and zincblende GaN using the parabolic (PB) and non-parabolic (NPB) band models at room temperature.

drift mobility at low electric fields, can be estimated from the slope of the velocity-field curve. The calculated low field drift mobility in the zincblende and wurtzite phases are, respectively, $1100 \text{ cm}^2\text{V}^{-1}\text{s}^{-1}$ and $790 \text{ cm}^2\text{V}^{-1}\text{s}^{-1}$ which is lower than values calculated by the iterative model.

The calculated electron kinetic energy as a function of applied electric field for the various valleys in two phases are depicted in figure 3.9. As a result of the smaller Γ-valley effective mass in zincblende GaN, there is a more rapid increase in the electron kinetic energy with increasing field for the zincblende phase. The importance of electron intervalley transfer at high electric fields can be clearly seen in figure 3.10. In this figure the fractional valley occupancies for both phases of GaN are plotted. It is obvious that the inclusion of satellite valleys in the simulations is important. Significant electron transfer to the upper valleys only begins to occur when the field strength
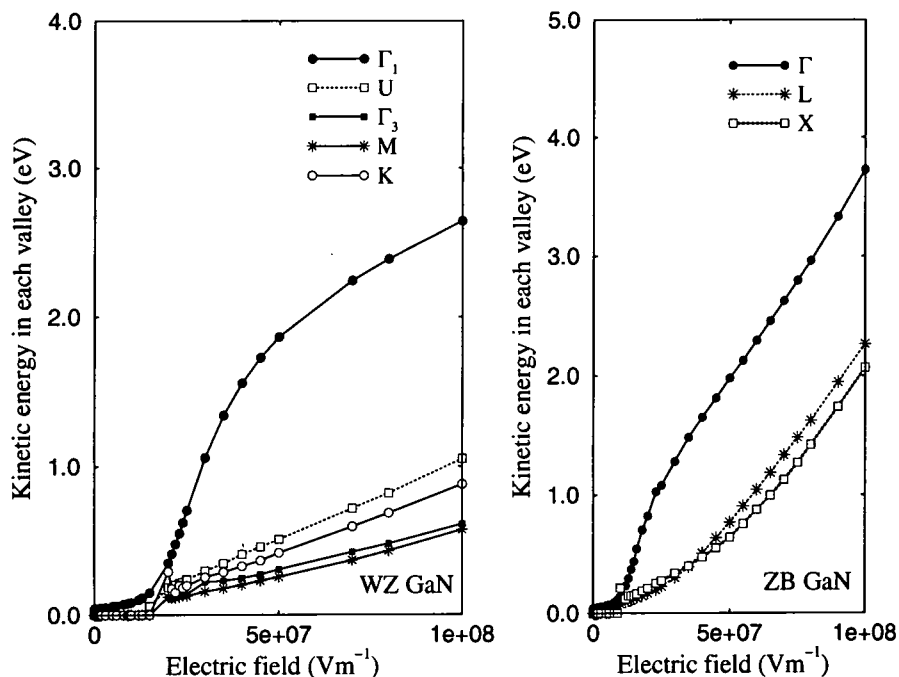
Figure 3.9: Calculated steady-state average electron energy in bulk wurtzite and zincblende GaN as a function of applied electric field in different valleys at room temperature.

is very close to the threshold value. At the threshold field the valley occupancies for the zincblende case are 18% and 2% for the X and L valleys, respectively. For the wurtzite phase we find that at the threshold field the Γ_1, U, K, M and Γ_3 occupancies are 94%, 5%, 0.5%, 0.3% and 0.2%, respectively.

The total average electron kinetic energy as a function of electric field is shown in figure 3.11, for wurtzite GaN (open-circle curve) and zincblende GaN (solid-circle curve). It can be seen that initially, kinetic energy increases with the electric field, due to the large proportion of electrons in the low mass Γ valley of both crystal structures. However, as the field increases, the electrons transfer to higher valleys with higher mass and increased scattering which causes a substantial reduction in the rate of increase of average kinetic energy. The detailed differences in the behaviour of the average electron energy with field for the two crystal structures is simply due to the different band structure features.

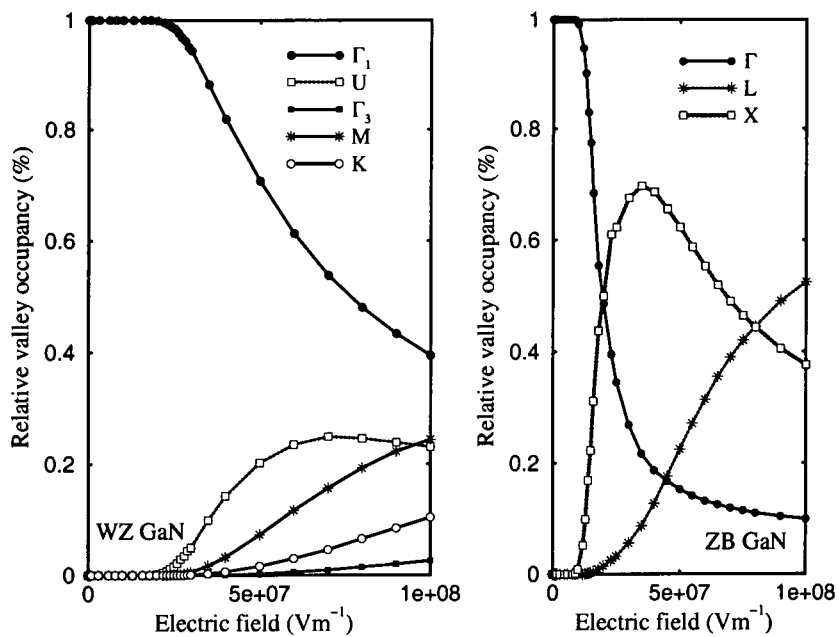**Figure 3.10:** Fractional occupation of the central and satellite valleys of wurtzite and zincblende GaN as a function of applied electric field using the non-parabolic band model at room temperature.
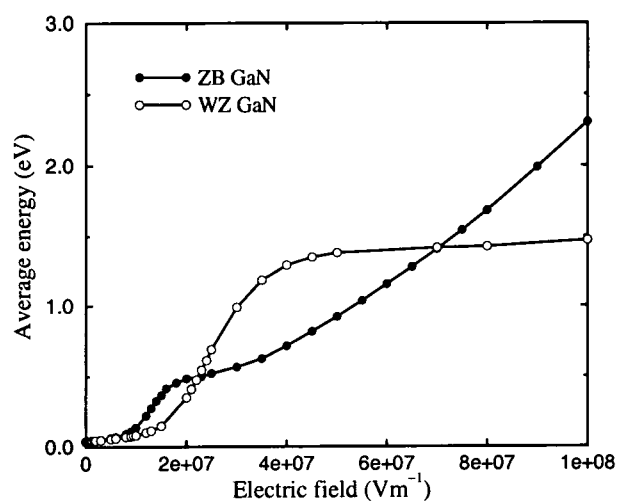

Figure 3.11: Total average electron kinetic energy as a function of applied electric field in bulk zincblende and wurtzite GaN at room temperature.

3.4.2   Effect of field direction

To investigate the effect of electric field direction on the steady-state velocity-field characteristics of wurtzite GaN, simulations have been performed for electric fields in the Γ-A and Γ-M directions. The drift velocities for an electric field along the Γ-A (c-axis) and Γ-M (parallel to basal plane) directions of the Brillouin zone are shown in figure 3.12a. At low electric fields, the drift mobility can be estimated from the slope of the velocity-field curve. For field values below 10^6 Vm^{-1} the calculated low field drift mobility in the Γ-M and Γ-A directions are, respectively, 1000 $cm^2V^{-1}s^{-1}$ and 790 $cm^2V^{-1}s^{-1}$. The linear dependence of velocity on electric field begins to be lost around a field of 5×10^6 Vm^{-1} where the bulk of the particle ensemble has an energy of the order of the optical phonon energy and the emission of polar optical phonons begins. The two curves reach different peak velocities for fields of close to 2×10^7 Vm^{-1} although the peak velocity for the Γ-A direction occurs at a field which is some 5% higher than for the Γ-M direction. The peak values in Γ-M and Γ-A directions are, respectively, 2.7×10^5 ms^{-1} and 2.3×10^5 ms^{-1}.

The reason for these differences is related to the higher effective mass of the Γ_1 valley in the A direction which reduces the low field mobility. It also means the field is less efficient in heating the electrons to the threshold for transfer to the U and K satellite valleys.

Figure 3.12b shows the corresponding average electron kinetic energy as a function of field, along the Γ-M and Γ-A directions. The curve for the direction applied parallel to the c-axis shows a lower average energy than that corresponding to the field in the basal plane which can be understood in a similar manner to the velocity results.
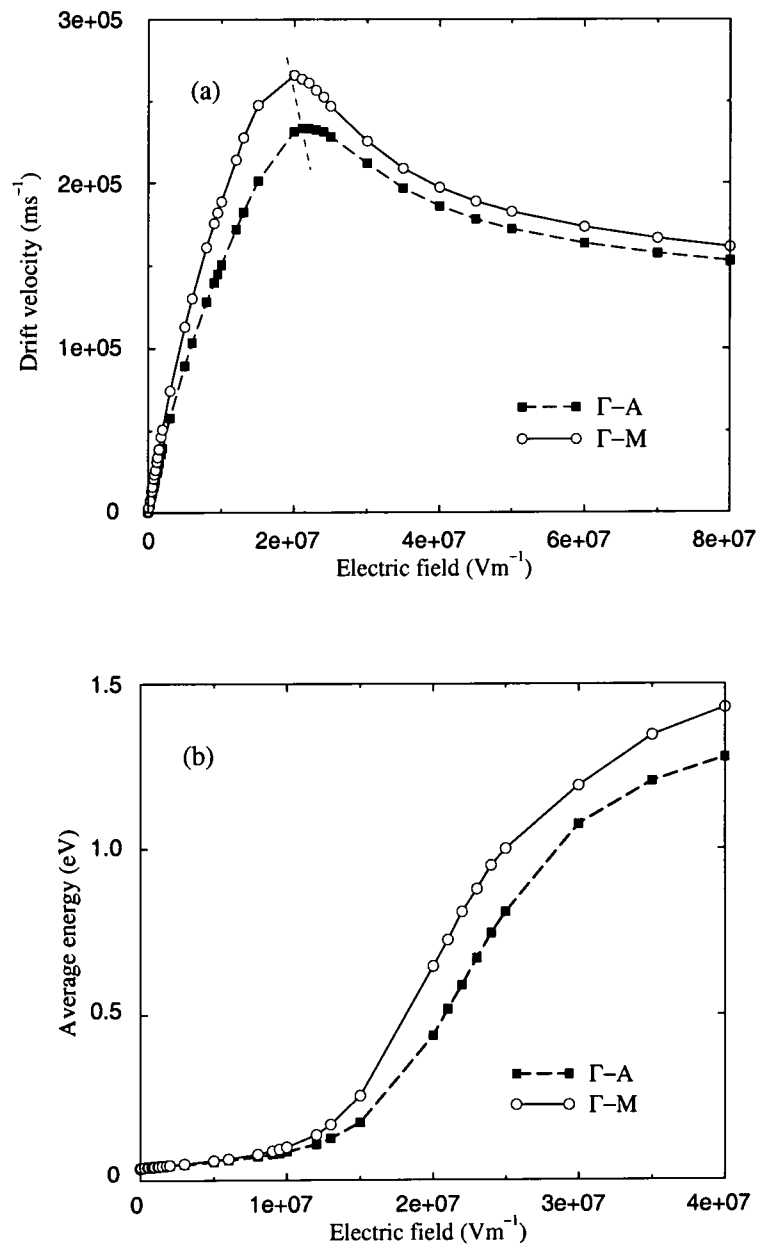
Figure 3.12: Simulated results of wurtzite GaN as a function of applied electric field using the non-parabolic band model along the Γ-A and Γ-M directions at room temperature. (a) Velocity-field characteristic and (b) Average kinetic energy.

3.4.3   Effect of temperature and electron concentration

Figure 3.13 shows the calculated electron drift velocity as a function of electric field strength for temperatures of 300, 450 and 600 K. The decrease in drift mobility with temperature at low fields is due to increased intravalley polar optical phonon scattering whereas the decrease in velocity at higher fields is due to increased intra and intervalley scattering. It can be seen from the figure that the peak velocity also decreases and moves to higher electric field as the temperature is increased. This is due to the general increase of total scattering rate with temperature, which suppresses the electron energy and reduces the population of the satellite valleys. This latter effect is apparent from the fact that the electron population in the Γ_1-valley increases with temperature as shown in figure 3.14.

Figure 3.13: Calculated electron steady-state drift velocity in bulk wurtzite GaN as a function of applied electric field at various lattice temperatures and assuming a donor concentration of 10^{22} m^{-3}. The peak drift velocity decreases by about 20% while the threshold field increases by same percent as the lattice temperature increases from 300 to 600 K.
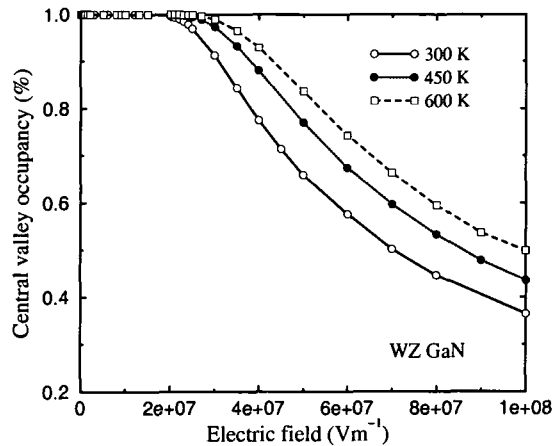
Figure 3.14: Fraction of electrons in the Γ_1 valley of wurtzite GaN as a function of applied electric field versus temperature.

Figure 3.15 shows how the velocity-field relation changes with temperature for electrons in the most populated Γ_1 and U valleys. There are significant statistical fluctuations in the results for the drift velocity of electrons in the U valleys for fields around 2×10^7 Vm^{-1}, which are caused by the relatively small number of superparticles occupying the valleys just above the threshold for intervalley transfer. Nevertheless it can be seen that the average drift velocity decreases as the temperature increases for both valleys. Comparison of the temperature dependence of the transport properties in wurtzite GaN (figure 3.13) and GaAs (figure 3.16) shows that the change in peak velocity of GaN from 300 K to 600 K is a reduction of about 35% whereas for GaAs it is about 78%. Therefore, the electron velocity in GaN is less sensitive to temperature than in GaAs [60–62], and GaN devices are expected be more tolerant to self-heating and high ambient temperature.

Figure 3.17 shows how the velocity-field characteristic of wurtzite GaN changes with impurity concentration at 300 K. It is clear that with increasing donor concentration, there are small changes in the average peak drift velocity and the threshold field. The results show the trend expected from increased ionized impurity scattering is in good general agreement with recent calculations by other workers [62,63].
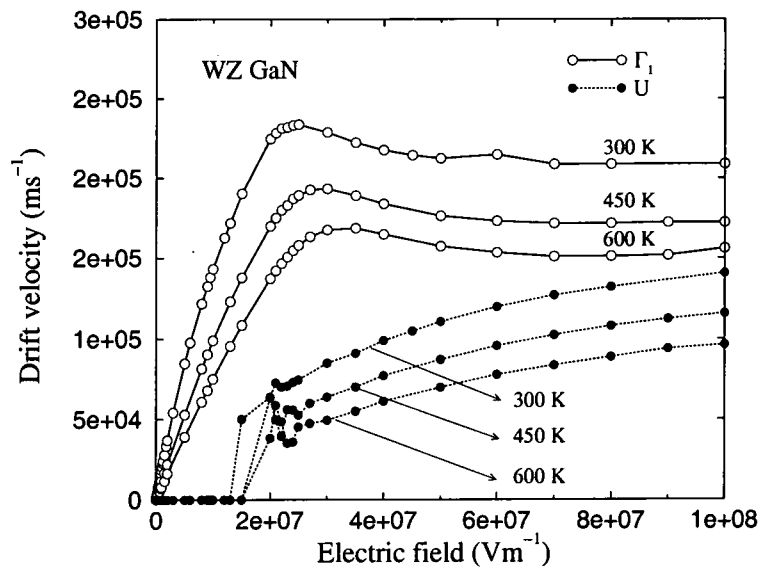
Figure 3.15: Temperature dependence of the drift velocity in the Γ_1 and U valleys in wurtzite GaN as functions of electric field.
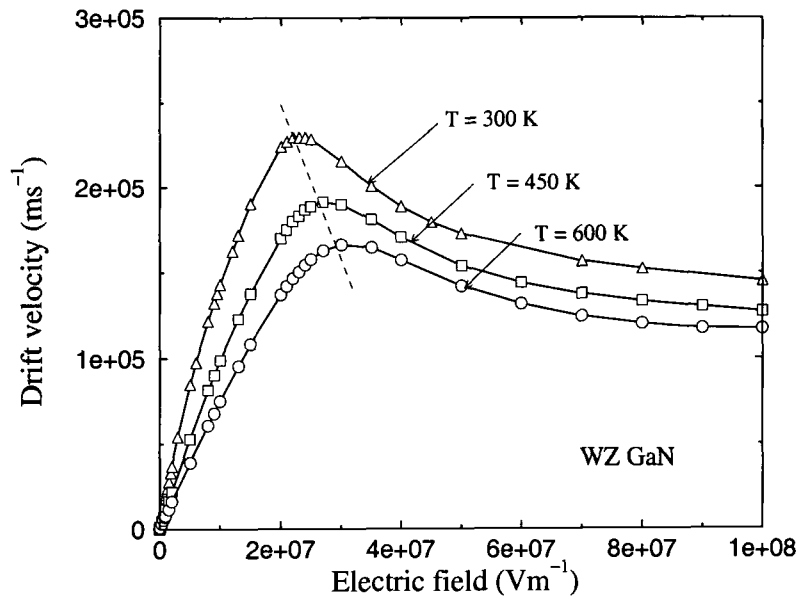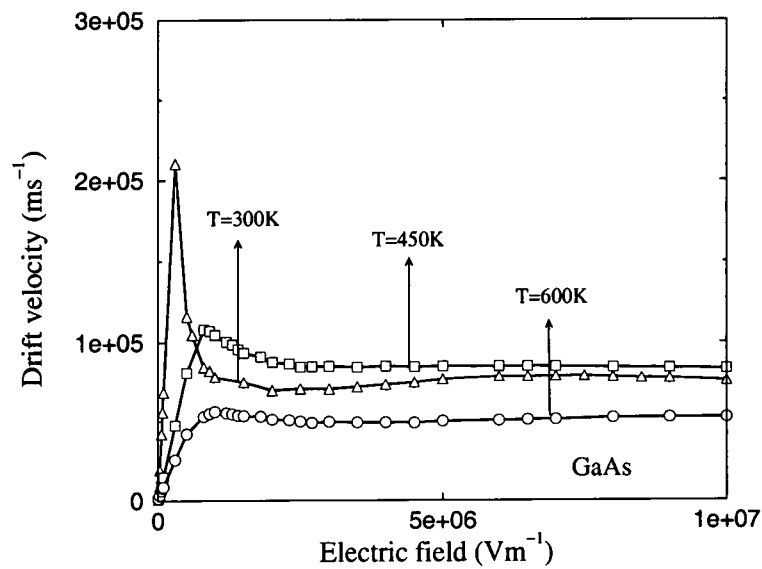

Figure 3.16: Calculated electron steady-state drift velocity in bulk GaAs as a function of applied electric field at various lattice temperatures and assuming a donor concentration of 10^{22} m^{-3}.
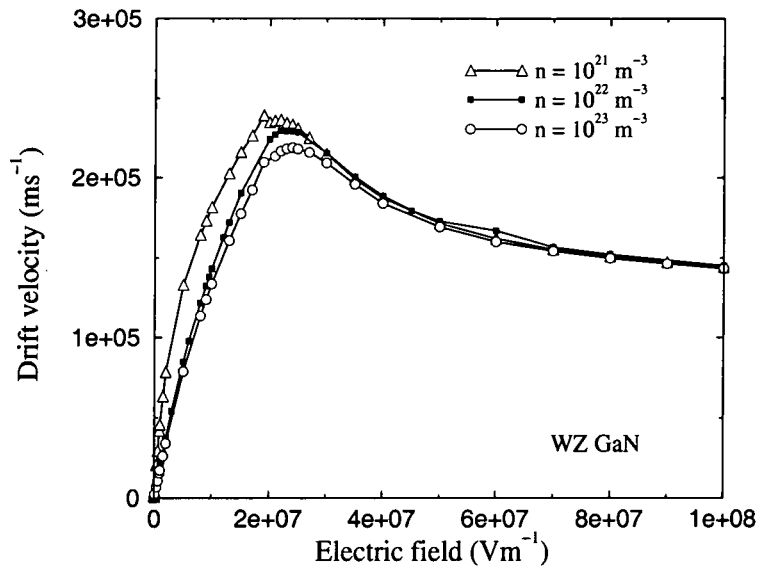
Figure 3.17: Electric field dependence of the drift velocity in wurtzite GaN at 300 K for various donor concentrations.

3.4.4 Transient electron transport in bulk GaN

It is interesting to study how electrons, initially in equilibrium, respond to the sudden application of a constant electric field. Velocity overshoot can occur for electrons in semiconductors when the relaxation rate of momentum is larger than that of energy [29]. The main mechanism that makes the relaxation rate of momentum larger than that of energy is the intervalley scattering when the electrons have reached an energy where transfer to the satellite valleys is possible. Application of a field comparable to the threshold field is necessary for the electrons to be sufficiently excited.

In figures 3.18a and 3.19a we show the transient response of electron velocity for both phases of GaN for fields up to 5×10^7 Vm^{-1}. In wurtzite GaN, we find very little or no overshoot occurs below the threshold field of 2.1×10^7 Vm^{-1}. As the electric field strength is increased to a value above the threshold field, overshoot begins to occur. As the field strength is increased further, both the peak overshoot velocity increases and the time for overshoot relaxation decreases. In zincblende GaN, the velocity overshoot initially increases more rapidly with increasing electric field due to the lower Γ valley effective mass. For example, at 5×10^7 Vm^{-1}, the maximum overshoot velocity for

Figure 3.18: (a) Transient response of electron velocity in bulk zincblende GaN to different applied electric field using the non-parabolic band model, (b) The fractional valley occupancy for applied electric field equal 5×10^7 Vm^{-1}.

zincblende GaN is about 8×10^5 ms^{-1}, whereas for wurtzite GaN it is about 4.8×10^5 ms^{-1}. It is found also that for the same value of the electric field above the threshold value, the electron drift velocity is always smaller in wurtzite GaN than in zincblende.

Also a peak saturation drift velocity ratio of approximately 2:1 is found for the wurtzite structure, while that for zincblende is close to 4:1. This difference is because of the smaller intervalley energy separation and smaller Γ valley effective mass in the zincblende phase. The smaller intervalley separation means that electrons can transfer to the upper valleys quicker, which reduces the average electron velocity owing to the upper valley's larger effective mass. The electron ensemble relaxes to a saturation drift velocity of approximately 2×10^5 ms^{-1} within 3ps in both structures, which is in very good agreement with Foutz *et al.* [63] who used a three-valley model. The evolution of the valley occupancies for both phases of GaN are also shown in figures 3.18b and 3.19b for an applied electric field equal 5×10^7 Vm^{-1}. The time for the satellite valley occupancies to reach steady-state depends on the value of the electric field.
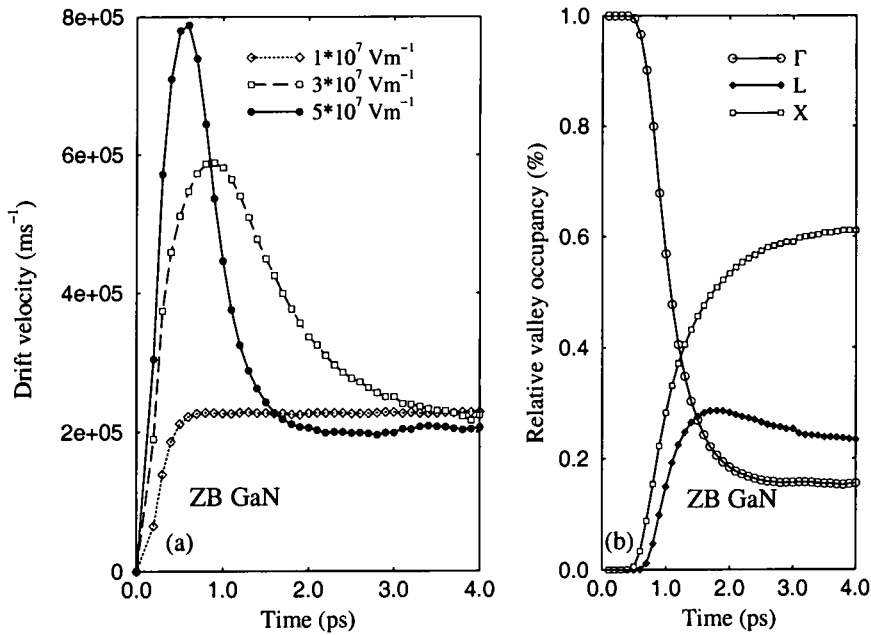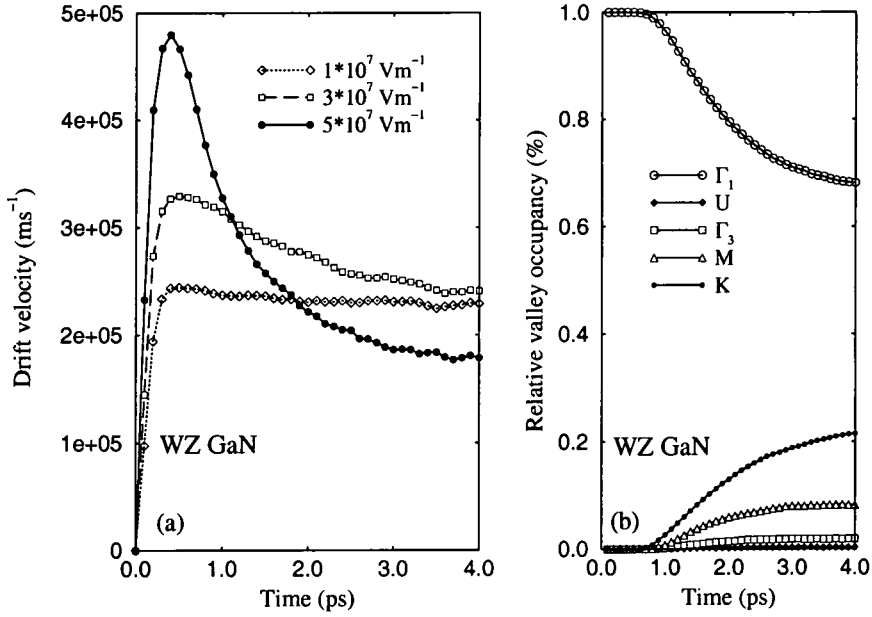
Figure 3.19: (a) Transient response of electron velocity in bulk wurtzite GaN to different applied electric field using the non-parabolic band model, (b) The fractional valley occupancy for applied electric field equal 5×10^7 Vm^{-1}.

3.5 Bulk transport properties in AlN and InN

In order to provide some comparison between the electron transport properties of different nitride semiconductors we have also carried out Monte Carlo simulations for wurtzite InN and AlN. The band structure parameters are estimated from recent band structure calculations [34, 65, 66] and are given in table 3.1. We report initially on the steady-state results and then the transient results.

3.5.1 Steady-state electron transport

The bulk group-III nitride velocity-field characteristics, predicted by our model are shown in figure 3.20. For all cases, the temperature is 300 K and the donor concentration is 10^{22} m^{-3}. We see that each compound exhibits a peak in its velocity-field characteristic. The peak drift velocity for InN is around 2.7×10^5 ms^{-1}, while those for GaN and AlN are about 2.3×10^5 ms^{-1} and 1.7×10^5 ms^{-1}, respectively. At higher

	GaN	InN	AlN
$m^*_{\Gamma_1}$	0.2	0.11	0.31
m^*_U	0.4	0.4	0.39
$m^*_{\Gamma_3}$	0.6	0.6	0.6
m^*_M	0.57	0.57	0.57
m^*_K	0.3	0.3	0.54
α_{Γ_1}	0.189	0.419	0.32
α_U	0.065	0.065	0.5
α_{Γ_3}	0.029	0.036	0.029
α_M	0.0	0.0	0.0
α_K	0.7	0.7	0.03
$\Gamma_1 - U$	2	1.9	0.61
$\Gamma_1 - \Gamma_3$	1.9	1.6	1.3
$\Gamma_1 - M$	3	2.2	0.9
$\Gamma_1 - K$	3.1	2.63	0.67

Table 3.1: Valley parameter selections for wurtzite GaN, InN and AlN

electric fields the drift velocity decreases, eventually saturating at around 1.6×10^5 ms^{-1} for both GaN and AlN and at 1.1×10^5 ms^{-1} for InN. The threshold fields are 2.1×10^7 Vm^{-1} and 4.4×10^7 Vm^{-1} for GaN and AlN, respectively.

For InN the peak drift velocity occurs at a significantly lower electric field of about 10^7 Vm^{-1} which is in good agreement with the results of Bellotti, who used a five-valley model [65], and of O'Leary et al. [66], who used a three-valley model. It should also be noted that the drift velocity of InN is substantially greater than that of GaN for low electric fields. The behaviour of InN can be explained in terms of the energy band structure. In particular, the different electron effective mass within the central valley $(0.11 \ m_0$ in InN versus 0.2 m_0 and 0.31 m_0 in GaN and AlN, respectively).

The valley occupancies for the Γ_1, U, Γ_3, M and K valleys are illustrated in figure 3.21 and show that the inclusion of the satellite valleys in the simulation is important.
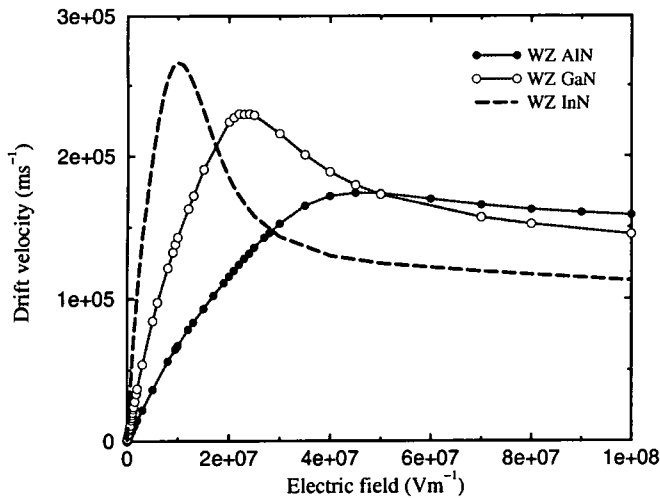
Figure 3.20: Calculated electron steady-state drift velocity in bulk InN, GaN and AlN as a function of applied electric field. The donor concentration is set to 10^{22} m^{-3} and temperature to 300 K.

Significant intervalley scattering into the satellite valleys occurs for fields above the threshold field for each material. This is important because electrons which are near a valley minimum have small kinetic energies and are therefore strongly scattered. It is apparent that intervalley transfer is substantially larger in InN over the range of applied electric fields shown, due to the combined effect of a lower Γ_1 effective mass, lower satellite valley separation energy, and slightly lower phonon scattering rate within the Γ_1 valley. Figure 3.21 also shows, the electron energy distribution functions for various valleys at an electric field of 5×10^7 Vm^{-1}, which is in the saturation regime. These distribution functions show similar features to those described previously for GaN and can be interpreted in terms of each material's band structure. We notice that the electron populations in the Γ_1 valley of InN and GaN increase until an energy of around 2 eV and after that decrease due to scattering to the satellite valleys. The behaviour of AlN is quite different. This is because of the relatively small Γ_1-satellite valley energy separation and the larger Γ_1 effective mass of AlN. At the field corresponding to the peak velocity in AlN we find, occupancies of 15% and 3% for the U and K valleys, respectively, while Albrecht *et al.* [33,60] used a three-valley model to obtain occupancies of 21% and 5%.
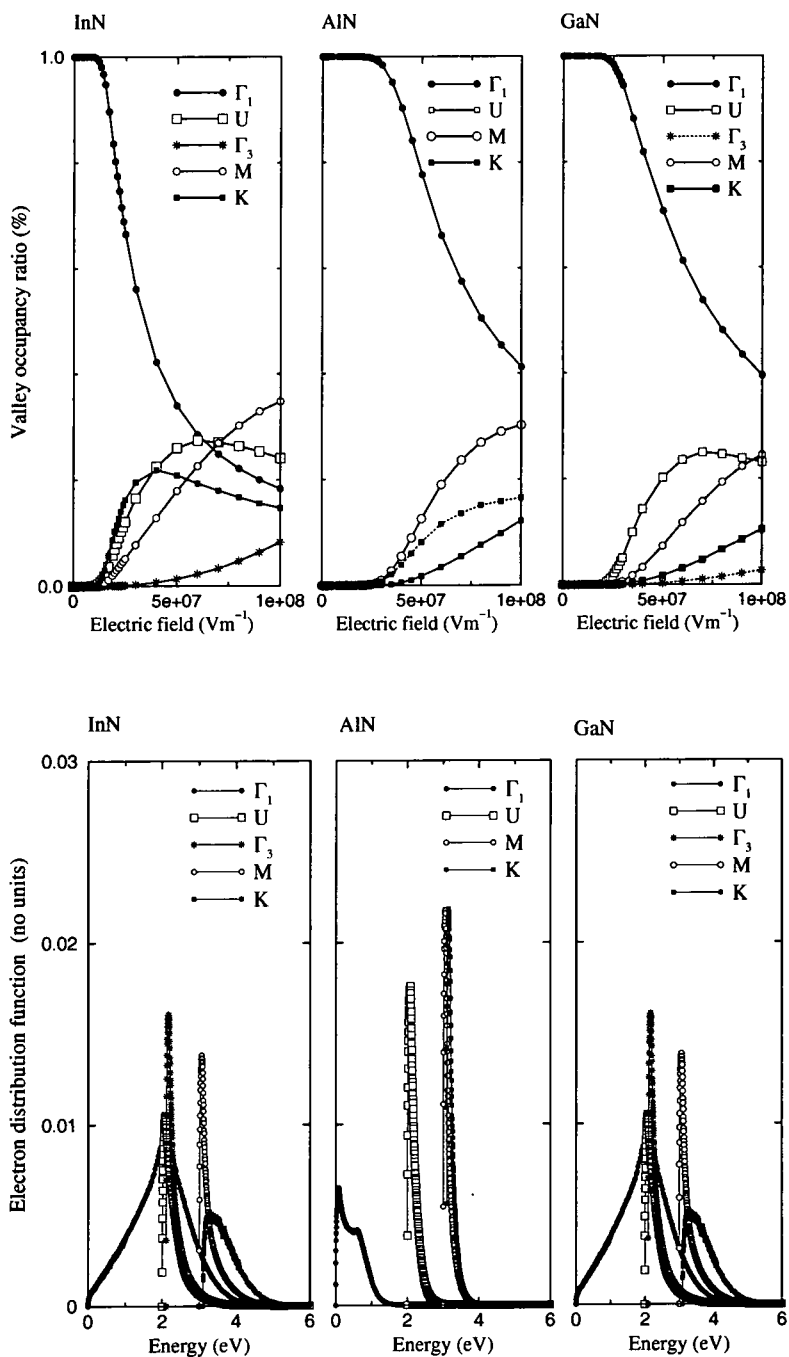
Figure 3.21: Comparison of the valley occupancies and their normalized electron distribution function in wurtzite InN and AlN with GaN for Γ_1, U, Γ_3, M and K valleys at room temperature.

3.5.2   Transient electron transport

We have also examined transient electron transport in bulk AlN and InN. The transient response of electrons in InN, GaN and AlN are compared in figure 3.22 for different electric field strengths. Note that the overshoot velocity in InN is higher and is more enduring than for the other materials. When the field is increased to 5×10^7 Vm^{-1} the peak velocity in InN increases to 6×10^5 ms^{-1}. The velocity overshoot effect in AlN is markedly weaker. This is because of the smaller intervalley energy separation, 0.61 eV (versus 2 eV in GaN and 1.6 eV in InN) and larger Γ effective mass, 0.31 m_0 (versus 0.2 m_0 in GaN and 0.11 m_0 in InN). The smaller satellite energy separation means that the electrons readily transfer to the satellite valleys, resulting in a reduced average electron velocity and the rapid removal of overshoot.
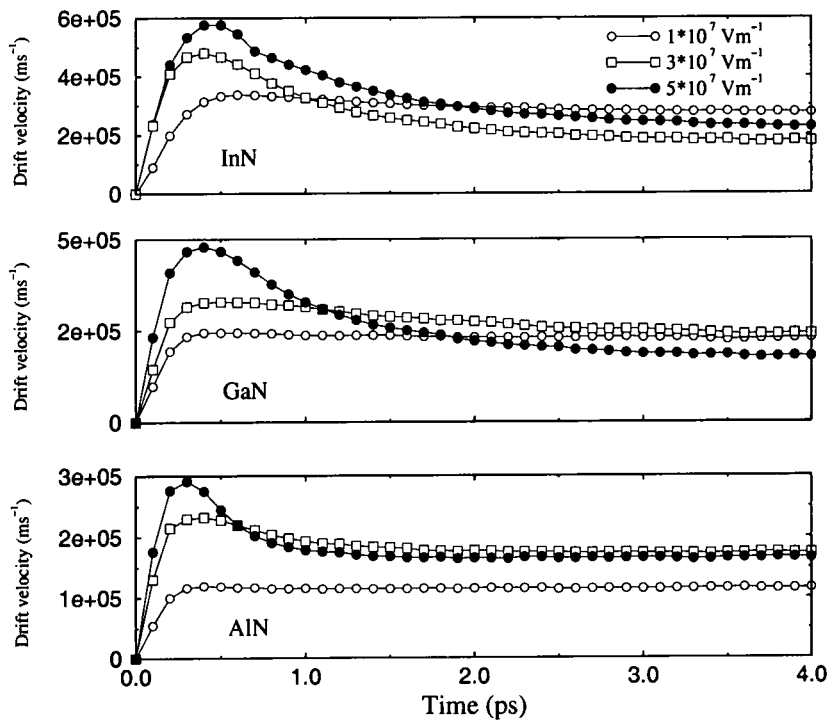
Figure 3.22: A comparison of the velocity overshoot effect exhibited by the group-III nitride semiconductors as calculated by our Monte Carlo simulation. The donor concentration is 10^{22} m^{-3} and the temperature is 300 K.

3.6 Conclusions

The temperature and electron doping dependences of the electron drift mobility in both phases of GaN at low electric field have been calculated using an iterative model. It is assumed that the electrons remain in the Γ valley of the conduction band, which is taken to be isotropic and non-parabolic. Our calculations show the low-field mobility is higher for the zincblende structure due to the lower effective mass in the central Γ valley. We have also found that piezoelectric and ionized impurity scattering processes are important at low temperatures.

High field transport calculations in GaN structures have also been performed using an ensemble Monte Carlo simulation. For the wurtzite structure a five-valley conduction band model has been used to simulate bulk transport properties in high electric fields. The model includes intravalley scattering due to optical and acoustic phonons and ionized impurities and intervalley phonon scattering. We have shown that the drift velocity initially increases with applied electric field to reach a maximum and then decreases, giving rise to a negative differential mobility. The reduction in drift velocity can be attributed to the transfer of electrons from the high mobility central Γ valley to the lower mobility satellite valleys.

Other results of the simulations, specifically the average electron energy, valley occupancy and normalized distribution functions show the importance of the population of the satellite valleys. We have shown the field required to produce the highest drift velocity is bigger for wurtzite GaN than for the zincblende phase. The difference is because of the larger Γ valley effective mass and the Γ-satellite valley separation in wurtzite GaN. However, the large threshold field of wurtzite GaN is attractive for high-power electronic applications, as is the relatively low temperature sensitivity of the transport properties that we have demonstrated.

In the case of wurtzite GaN, the electron transport has been modelled with an electric field applied both parallel and perpendicular to the (0001) c-axis. The velocity field curve exhibits a noticeable anisotropy with respect to field direction. The peak drift velocity has a maximum value of to 2.7×10^5 ms^{-1} for a field in the direction parallel to the basal plane but 2.3×10^5 ms^{-1} in the c-axis direction.

Steady-state and transient electron transport in wurtzite InN and AlN has also been examined and compared with that for GaN. For all materials, we find that electron velocity overshoot only occurs when the electric field is increased to a value above a critical field, specific to each material. The computed velocity field characteristics show that InN has superior transient electron transport properties. We have also shown that GaN exhibits much more pronounced overshoot effects compared to AlN but at much higher electric fields.

Chapter 4

GaN-based n^+-n-n^+ Diodes

4.1 Introduction

In this chapter, we report the use of our ensemble Monte Carlo simulation to study the properties of a GaN n^+-n-n^+ diode. The motivation for the study is that the simulation of that simple structure can provide useful insight into some of the transport effects that occur in the more complex devices such as MESFETs and HFETs that are considered in subsequent chapters.

Tomizama et $al.$ [67] were the first to simulate a submicron GaAs n^+-i(n)-n^+ diode by the ensemble Monte Carlo technique using a two valleys model. Our simulations are similar in nature but use the five-valley model appropriate for wurtzite GaN. Steady-state results of high field transport studies have been obtained for lattice temperatures up to 600 K, in order to gain some insight into the hot carrier transport and the energy distribution function that would be generated in the gate-drain region of a power field effect transistor. The parameters used in the present Monte Carlo simulation for wurtzite GaN are the same as those used in chapter 3. In section 4.2 and 4.3, we discuss the transport properties of a GaN based n^+-n-n^+ diode, and the effects of the doping and the length of the active layer are considered. Section 4.4 draws brief conclusions from the results.

4.2 Device structure

The device considered is the one-dimensional GaN n^+-n-n^+ structure of total length 1 μm shown in figure 4.1. A lightly doped active layer (n-layer) is sandwiched between cathode and anode (n^+) layers, which are abruptly doped with a donor density of 10^{24} m^{-3}. The length of the active layer is either 0.6 μm or 0.4 μm. Approximately 10^4 particles are used in the simulation and lattice temperatures up to 600 K are considered. The applied anode voltage V_a is varied between 10 and 50 V to investigate the effects of field variations on the transport properties. This range of voltages is large enough that velocity overshoot and intervalley transfer effects occur.
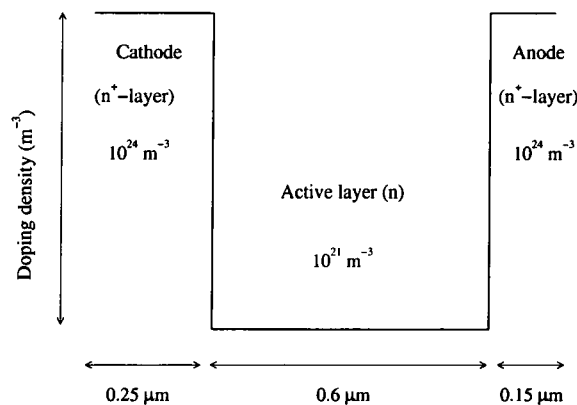
Figure 4.1: Doping profile for the GaN based n^+-n-n^+ diode.

4.3 Transport results and discussion

Figure 4.2a shows the distribution of hot electrons throughout the GaN n^+-n-n^+ diode in the steady-state at 300 K with a bias of 50 V when the active layer doping level is 10^{21} m^{-3}. It is apparent that there is a significant concentration in the satellite valleys on the anode side of the active layer. These electrons have attained enough energy under the action of the electric field to be scattered into satellite valleys.

Figures 4.2b and 4.2c show the corresponding distribution of energy and velocity parallel to the electric field. The electrons in the active layer can be divided into three
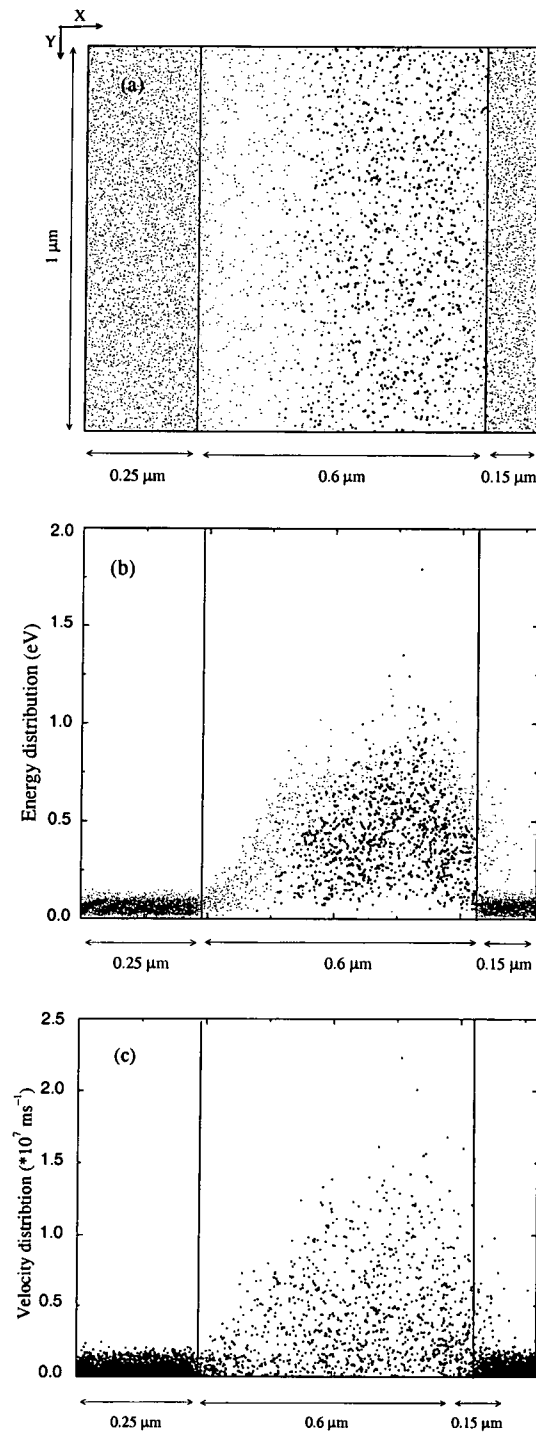
Figure 4.2: (a) Hot electron position throughout the simulated GaN n^+-n-n^+ diode, (b) Energy distribution and (c) Velocity distribution. The bolder points represent hot electrons in the upper valleys (U, M and K valleys). The applied anode voltage is $V_a = 50$ V and the results are at room temperature.

main categories:

1. Electrons in the Γ_1 valley, travelling more or less ballistically towards the anode.

2. Electrons in the satellite valleys, which have been excited by the field in the active layer.

3. Electrons in the Γ_1 valley which have been back-scattered from the anode n$^+$-layer.

The electric field in the device as a function of position x (see figure 4.1) is shown in figure 4.3 for anode voltages between 20 and 50 V. It is apparent from this figure and from figure 4.4d that essentially all the potential is dropped in the active layer. However, as a result of the inhomogeneous space charge the field does vary substantially with position, reaching a maximum magnitude near the anode.
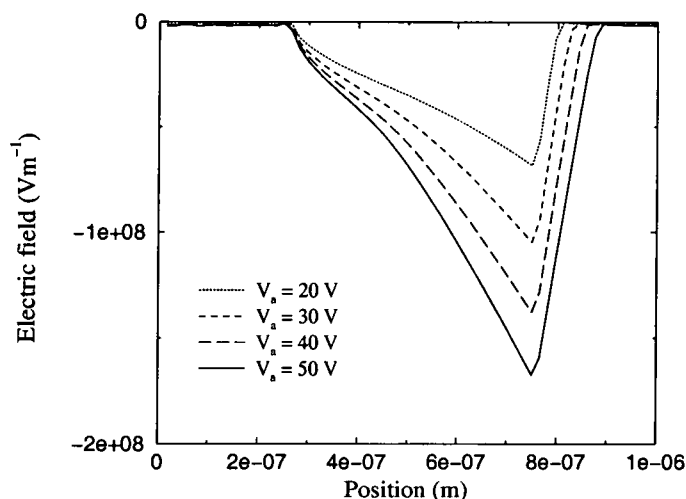
Figure 4.3: The electric field in the GaN n$^+$-n-n$^+$ diode for anode voltages between 20 and 50 V at room temperature.

Figures 4.4a-c show some features of the state of the device at temperatures of 300 K, 450 K and 600 K when the applied voltage is 50 volts. The free electron concentration through the device is plotted in figure 4.4a. The electrons diffuse from the cathode and anode into the active layer and are accelerated towards the anode by the field.

The resulting space charge causes the departure from a uniform electric field clearly apparent in figure 4.3.
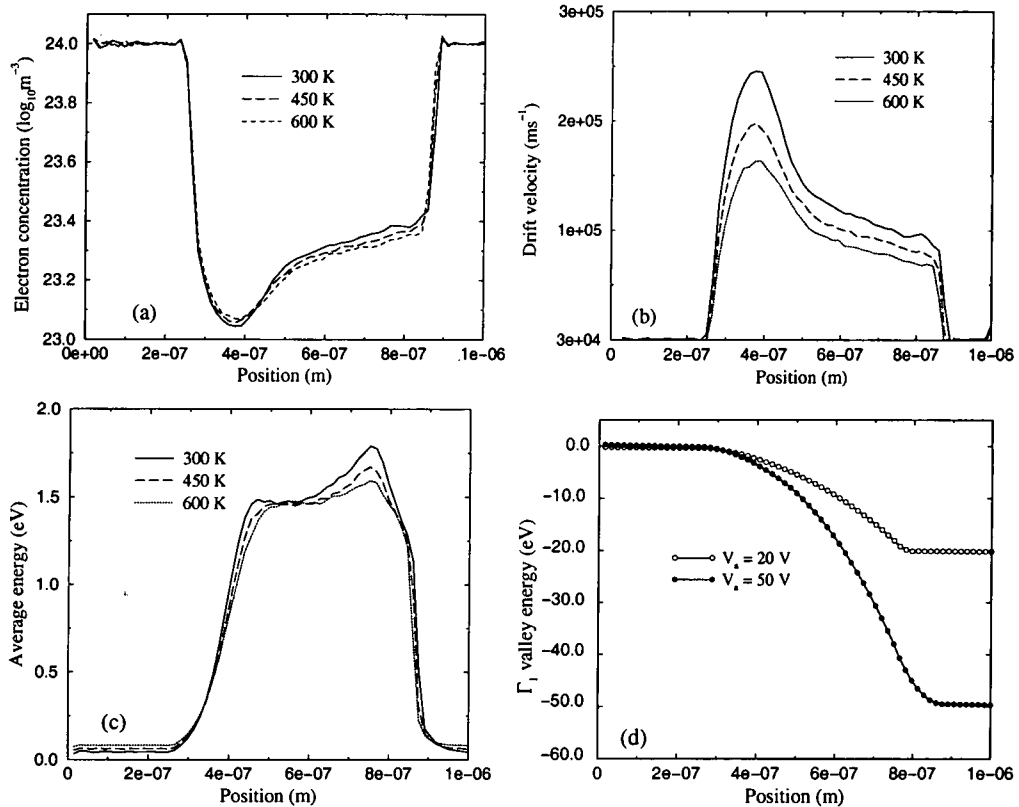
Figure 4.4: Electron transport characteristics as a function of position in the model GaN diode at different temperatures. (a) Electron concentration, (b) Average drift velocity, (c) Average kinetic energy and (d) Γ_1 valley energy profile for $V_a = 20$ V and $V_a = 50$ V.

Figure 4.4b shows that the average drift velocity in the active layer has a maximum value of about 2.4×10^5 ms^{-1} at 300 K. Raising the temperature to 600 K reduces the maximum drift velocity to a value of 1.6×10^5 ms^{-1}. A similar decrease of drift velocity with temperature was seen in bulk material (chapter 3) and is due to increased electron scattering. The plot of average electron kinetic energy across the device (figure 4.4c) provides further information on the dynamics. The electrons reach an average energy between 1.6 and 1.8 eV near the anode region and the more energetic electrons in

the distribution have sufficient energy to transfer to the upper valleys. Finally the Γ_1 valley energy profile for two different voltages applied across the device are illustrated in figure 4.4d.

To investigate the temperature dependence of the valley occupancy and the related energy distribution functions in the active layer, we have simulated the GaN n^+-n-n^+ diode with an applied voltage of 50 V and temperatures of 300 K and 600 K. The results are presented in figure 4.5. The high electric field in the active layer creates a significant electron population in the U, M and K valleys. Increasing the temperature from 300 K to 600 K causes some decrease in the population of the higher valleys. As noted earlier, this effect is due to increased phonon scattering which suppresses the heating of carriers by the electric field. Note, however, the effect is relatively small considering the large increase in temperature.

4.3.1 Effect of the active layer length and doping

To investigate how the diode behaviour is affected by active layer length, simulations have also been performed for a diode with a 0.4 μm active layer, keeping all other device parameters constant.

Figure 4.6 illustrates the effect on the transport properties of decreasing the length of the active layer when the applied anode voltage is 50 V. The maximum electron velocity for the 0.4 μm case is marginally greater than the 0.6 μm case and has a value of about 2.8×10^5 ms^{-1} close to where the electron density has its minimum. Near the anode the velocity approaches the value for the longer active layer, which is characteristic of collision-dominated transport. As a result, the electron velocity averaged over the active layer is substantially greater in the 0.4 μm case because the region of quasi-ballistic motion near the cathode is a greater fraction of the active layer. Simulations that have been carried out for various active layer doping levels, but not shown here, demonstrate that the average drift velocity decreases slowly as the doping increases, but the effect is small because impurity scattering has a relatively small influence on hot carrier transport.
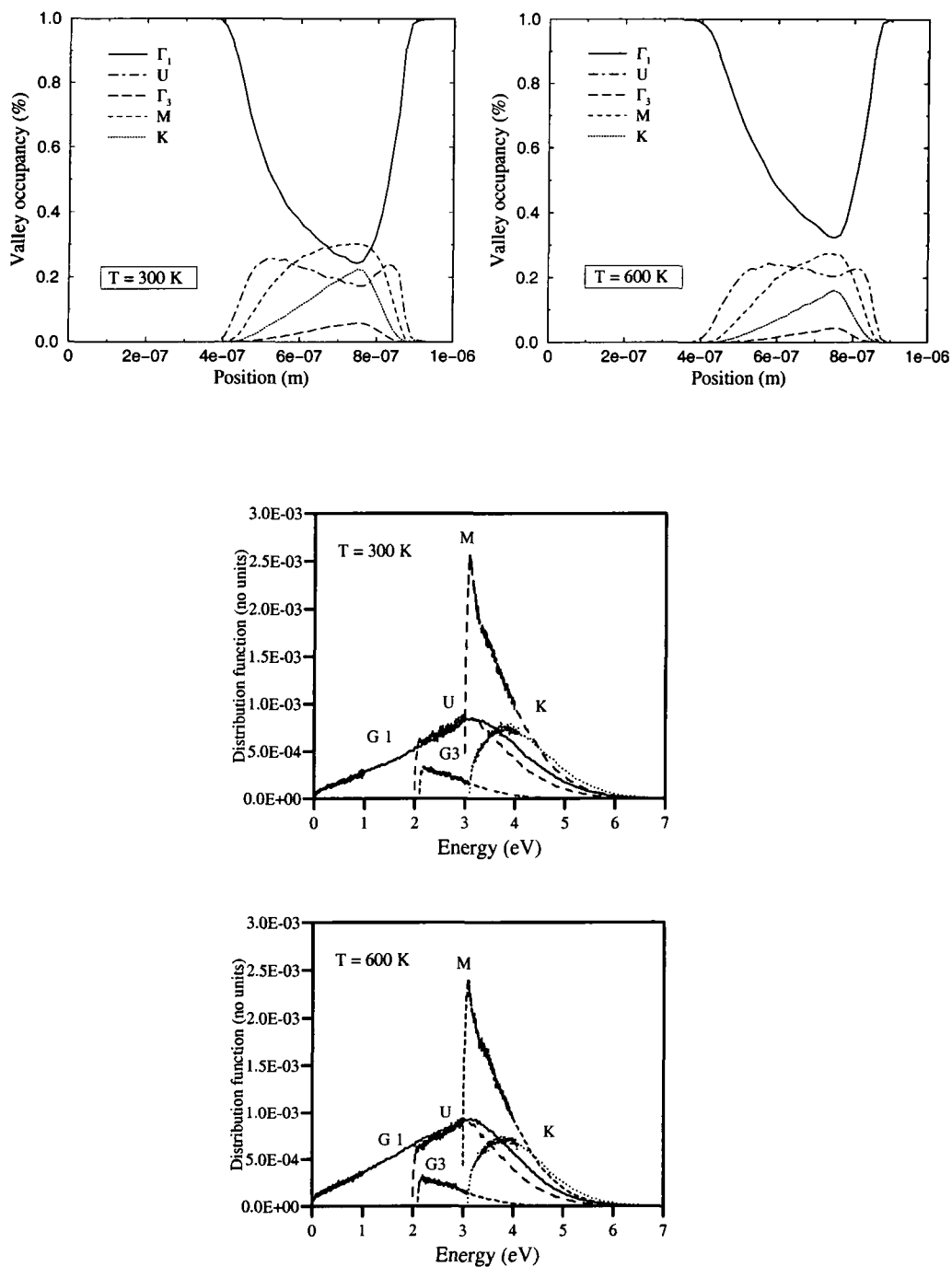
Figure 4.5: Valley occupation and the related energy dependence of electron distribution functions for Γ_1, U, Γ_3, M and K in a GaN wurtzite n^+-n-n^+ diode.
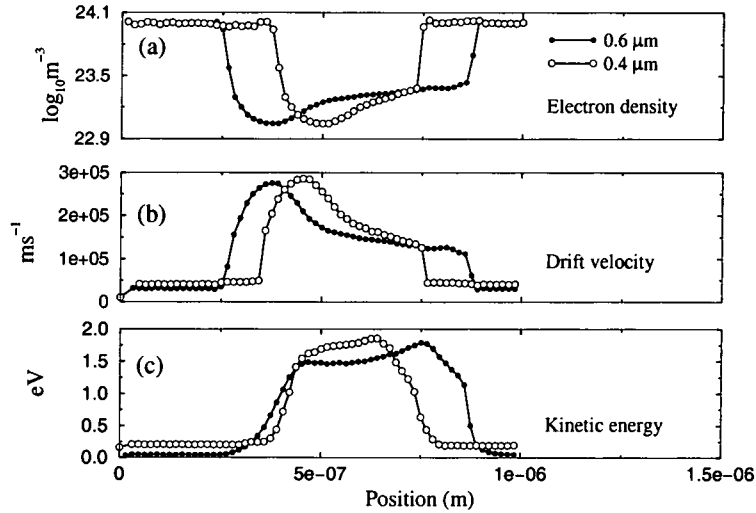
Figure 4.6: Electron transport data recorded as a function of position in the model n^+-n-n^+ diode at room temperature for two different active layer lengths when $V_a = 50$ V. The cathode-active layer interface is at 0.25 μm for the 0.6 μm device and at 0.35 μm for the 0.4 μm device. (a) Electron density, (b) Average drift velocity and (c) Kinetic energy.

4.4 Conclusions

In this chapter the results of simulations of electron transport in GaN n^+-n-n^+ diodes have been reported. The diodes have highly doped n^+-layers serving as the cathode and anode. The anode voltages V_a ranged from 10 to 50 V and lattice temperatures between 300 and 600 K have been considered. The electrons injected from the cathode initially travel quasi-ballistically but there is substantial transfer to the upper satellite valleys as the anode is approached, resulting in a reduced average electron velocity in that region. The peak drift velocity ranges from 2.2×10^5 ms^{-1} to 2.8×10^5 ms^{-1}, with a donor density of 10^{21} m^{-3} and an active layer length of 0.6 μm. Raising the lattice temperature to 600 K reduces the peak drift velocity, but it still remains above 1.5×10^5 ms^{-1}. Our results also show that decreasing the length of the active layer increases the electron velocity averaged over the length of the device because quasi-ballistic transport occurs in a larger fraction of the device.

Chapter 5

Simulation of GaN MESFETs

5.1 Introduction

In this chapter, results are presented relating to the Monte Carlo simulation of wurtzite GaN field effect transistors (MESFETs). The aim of the chapter is to provide an understanding of the important microscopic processes in such devices. In particular, we consider the effect of electron traps on the electrical characteristics of GaN MESFETs and make a comparison between devices with and without traps. The results are discussed and compared with experiments and calculations performed by other workers.

5.2 GaN Based MESFET

GaN has become an attractive material for power transistors [68–70] due to its wide band gap, high breakdown electric field strength, and high thermal conductivity. Also the material has a relatively high electron saturation drift velocity and low relative permittivity, implying potential for high frequency performance. However, set against the virtues of the material are disadvantages associated with material quality. GaN substrates are not readily available and the lattice mismatch of GaN to the different substrate materials commonly used means that layers typically contain between 10^8 and 10^{10} threading dislocations per cm^2. Further, several types of electron trap occur in the device layers and have a significant effect on GaN devices.

5.3 Device structure and simulation details

A schematic diagram of the structure of a MESFET is shown in figure 5.1a. The device consists of ohmic source and drain contacts on either side of a Schottky gate contact on the surface of a semiconductor layer. Contact lengths and separations are typically of the order of a micrometre or less. The layer beneath the contacts is a doped n-type semiconductor, typically 0.1 μm to 0.2 μm thick. A buffer layer may be included between the active layer and the semi-insulating substrate of the device. In the absence of the gate, the active layer provides a channel for the passage of electrons between source and drain. Hence current flows through the device when a positive voltage is applied between the drain and source. However, the Schottky barrier gate creates a depletion region which constricts the channel, either partially or completely. Here we consider normally-on MESFETs in which the channel is not completely constricted at zero gate voltage. However, when a negative bias is applied to the gate, the width of the depletion layer increases and the channel is narrowed further. At a certain gate voltage, pinch-off is said to occur when the depletion region extends through the whole thickness of the channel.

SLURPS was originally developed for the simulation of bipolar and field effect transistors based on the compounds and alloys of Al, In, Ga, As, and P (see for example [71, 72]), and has been thoroughly validated for such devices. Here its capabilities have been developed further to carry out simulations of electronic transport in field effect transistors based on group III-nitrides in the wurtzite crystal structure. The GaN MESFET that we have simulated is illustrated in figure 5.1b. In order to make comparison with experiment, we have used the same device geometry as Trassaert *et al.* [73]. The orientation of the *c*-axis of the wurtzite crystal structure is normal to the surface of the device. The overall device length is 3.3 μm (in the *x*-direction), with 0.3 μm gate and 0.5 μm source and drain lengths. The source to gate and gate to drain separations are 0.8 μm and 1.2 μm, respectively. The source and drain contacts are ohmic and the Schottky barrier height of the gate is 1 eV.

In the simulations the ohmic source and drain contacts are assumed to be ideal and are described by Dirichlet boundary conditions with the potential and electron
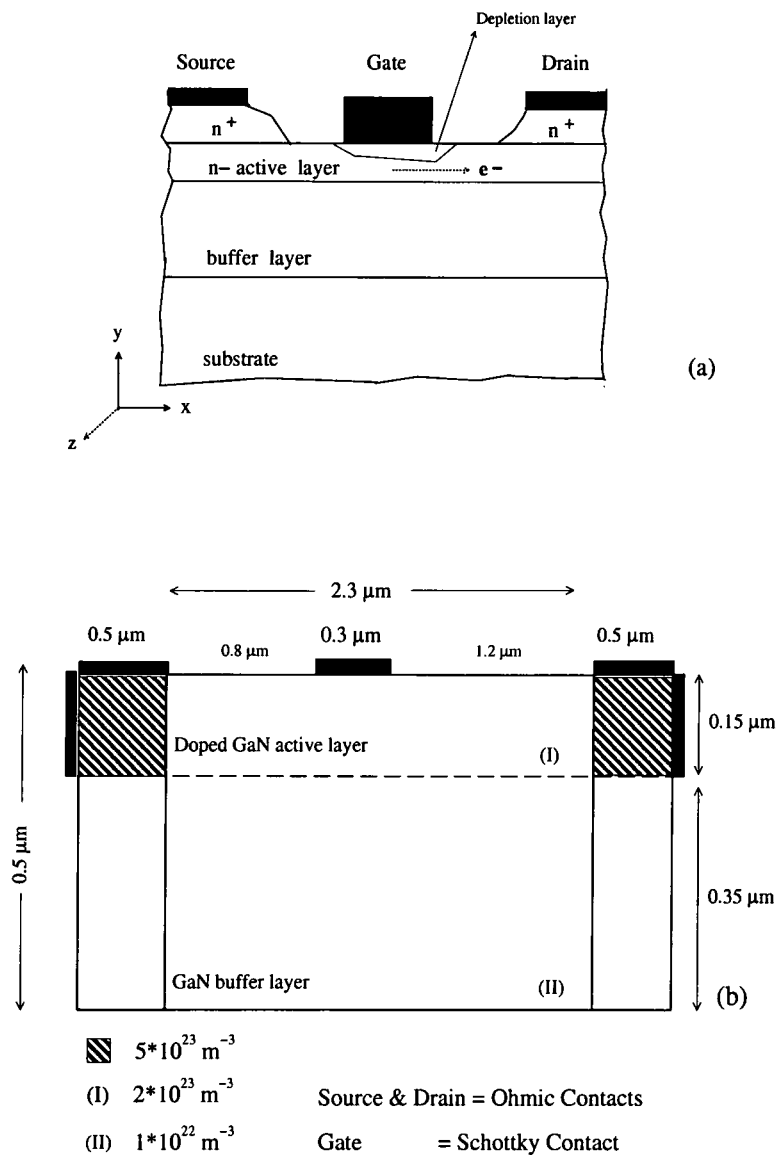
Figure 5.1: (a) Schematic representation of a MESFET and (b) Cross section of the GaN MESFET structure which we have considered in our simulation. The source and drain contacts have low resistance ohmic contacts, while the gate contact forms a Schottky barrier between the metal and the semiconductor epilayer.

concentration fixed. To maintain the latter condition, superparticles are added or re-moved in the immediate vicinity of the contact as appropriate. The Schottky barrier gate is modelled by fixing the potential of the contact at a value equal to the applied potential minus the barrier height. The ohmic and Schottky contacts absorb all su-perparticles that are incident on them. On the boundary of the device other than the contacts, a zero value of the electric field normal to the boundary is prescribed and any superparticles incident on the boundary are reflected. The source potential is set at zero (reference potential), while the gate and drain have static or time-dependent voltages applied. The timestep between sequential solutions of Poisson's equation is 1 fs. Electron transport is based on the five-valley model of wurtzite GaN described in chapter 3. In order to reduce the statistical fluctuations associated with the stochastic simulation to an acceptable level, 20,000 superparticles are used.

5.4 Simulation results

Figure 5.2 compares the instantaneous distribution of electrons throughout the device in the steady-state for different gate and drain biases at room temperature. When a positive potential V_{ds} is applied to the drain, electrons flow from source to drain, giving a current I_{ds} from source to drain. The depletion region of the Schottky barrier restricts the current path to the lower part of the channel and the buffer layer. At zero drain bias (figure 5.2a), the depletion layer beneath the gate has a symmetric shape. At zero gate and drain bias, the depletion region corresponds to that associated with the built-in potential of the Schottky barrier, but is larger for the case of gate bias $V_{gs} = -1$ V shown here. As V_{ds} is increased from zero, the depletion layer becomes asymmetric in shape since the potential difference between the gate and the channel is greater at the drain end than the source end of the gate. The channel is more constricted at the drain end of the gate (see for example at $V_d = 18$ and 30 volt in figures 5.2b and 5.2c) and the field along the channel is also higher in that region.

As the drain-source voltage is increased still further, the field at the drain end of the gate approaches the value at which the electron velocity along the channel saturates.
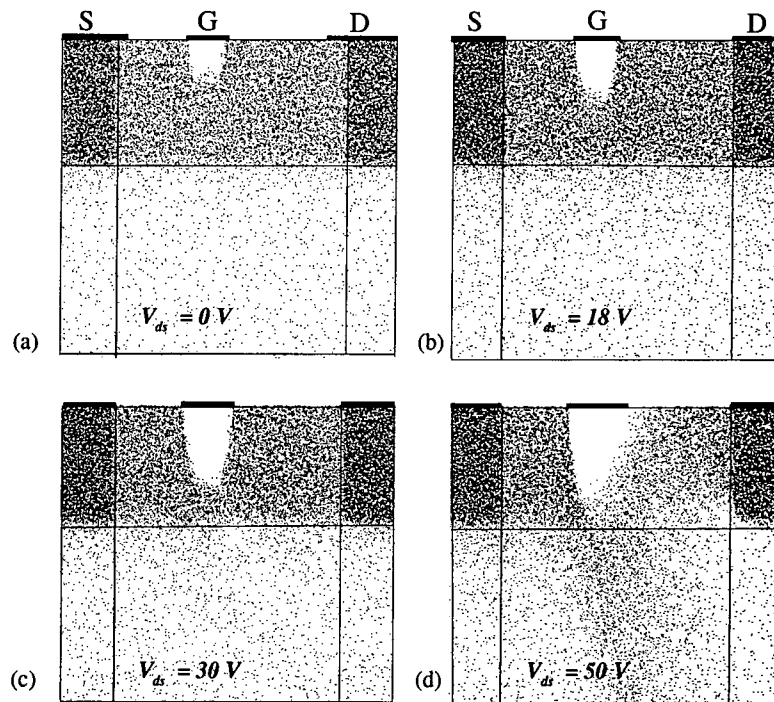
Figure 5.2: Depletion layer profiles for different drain and gate biases for GaN MESFET at room temperature.

Beyond this value, which corresponds to the threshold voltage in the drain current-voltage characteristics, further increase in drain-source voltage does not substantially increase the drain-source current. The length of the region of the channel over which the electrons are in velocity saturation increases and there is some carrier accumulation within the channel. The depletion layer edge at the drain end of the gate also moves closer to the drain as the drain-source voltage increases. Note also that the transition between the gate depletion region and the charge neutral bulk is far from sharp on the drain side. At a sufficiently negative gate potential the depletion layer punches through to the high-resistivity buffer layer, and the source and drain electrodes are connected only by leakage paths within the buffer layer and substrate (see figure 5.2d). An important factor in the high frequency performance of the MESFET is the time taken for electrons to traverse the region of the device beneath the gate, and the performance is enhanced by a high average electron velocity through that region. In this connection

it should be pointed out that GaN offers a higher electron velocity in short gate devices than GaAs as is shown in subsequent sections.

The spatial distribution of hot electrons throughout the device for each valley at $V_{gs} = -1$ V and $V_{ds} = 50$ V for room temperature operation is shown in figure 5.3. Electrons are seen to exist in the upper valleys only to the right of the high field region, which exists on the drain side of the gate, because it is only there that the electrons have attained enough energy to be scattered into the satellite conduction valleys. Also note there is an injection of electrons from the channel into the buffer layer; a process which is eventually opposed by the electric field created by the resulting negative space charge in the buffer layer. Figure 5.3 also shows that the distribution of electrons occupying the upper valleys extends a significant way towards the drain region where the electric field is much lower. This is a result of the finite time that it takes for phonon scattering to return the electrons to the Γ-valley.

Figure 5.4 shows the valley electron occupancies throughout the device. It can be seen that significant electron transfer to the upper valleys only begins to occur under the gate. Approximately 20% of the electrons occupy the higher valleys (mainly U and M valleys) in the vicinity of the gate which is similar to the valley occupancy ratio in the active layer of the n^+-n-n^+ diode discussed in the previous chapter.

Figure 5.5 shows various microscopic properties of the device when the source-drain bias is 50 V and the gate voltage is -1 V; specifically the longitudinal electric field, the Γ-valley band profile, the electron kinetic energy, the average drift velocity and the total electron density as a function of distance from the source. The longitudinal electric field plotted in figure 5.5a shows the high electric field in the region under the gate, which has been referred to earlier. Related to this is the Γ-valley band profile throughout the device in figure 5.5b. Note almost all the drain-source potential is dropped within the gate-drain region, leaving a flat potential profile near the source and drain. As electrons move towards the drain, they lose potential energy and gain sufficient kinetic energy to transfer to the upper conduction valleys where their drift velocity is reduced. The variations of average electron kinetic energy and average drift velocity throughout the simulated device are shown in figures 5.5c and 5.5d, respectively. The average
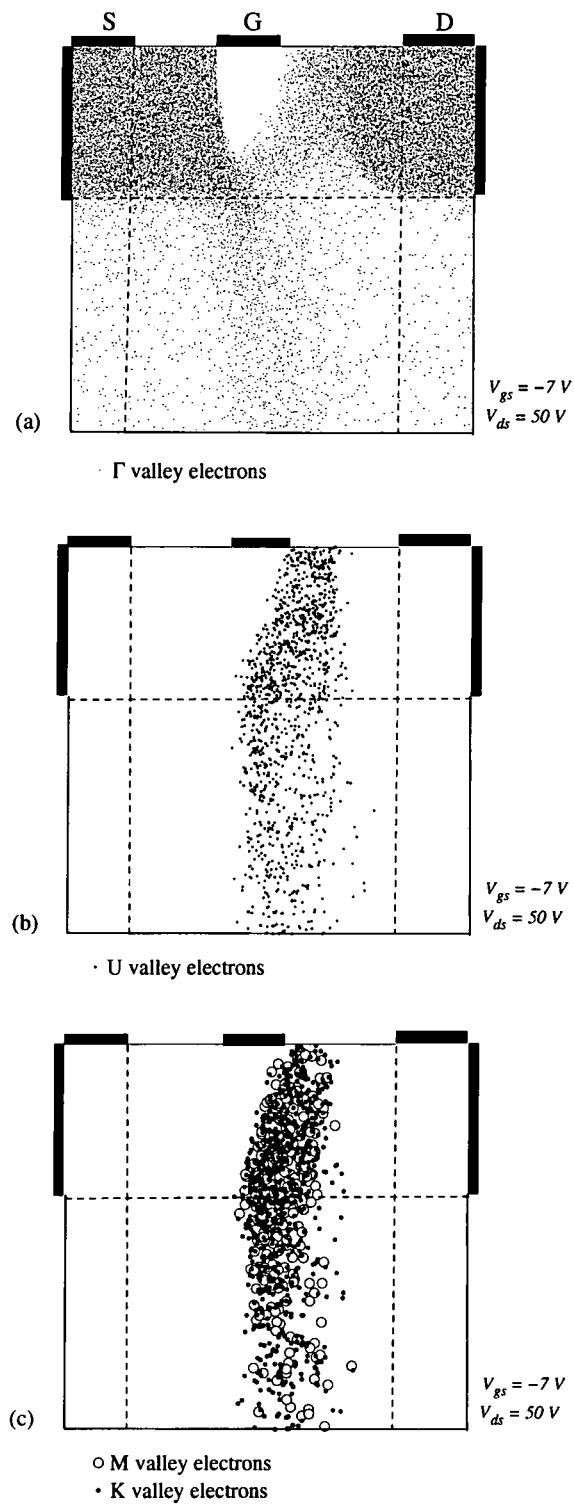
Figure 5.3: The distribution of hot electrons at room temperature for $V_{gs} = -1$ V , $V_{ds} = 50$ V in central Γ valley and upper valleys.

electron velocity reaches about 2.1×10^5 ms^{-1} and then declines towards the drain. The steep decrease in the average kinetic energy on the drain side of the gate is due to the transfer of electrons to the upper valleys. The electron density through the device is shown in figure 5.5e. The gate depletion region is clearly seen where the electron density is several orders of magnitude lower than it is near the source and drain.
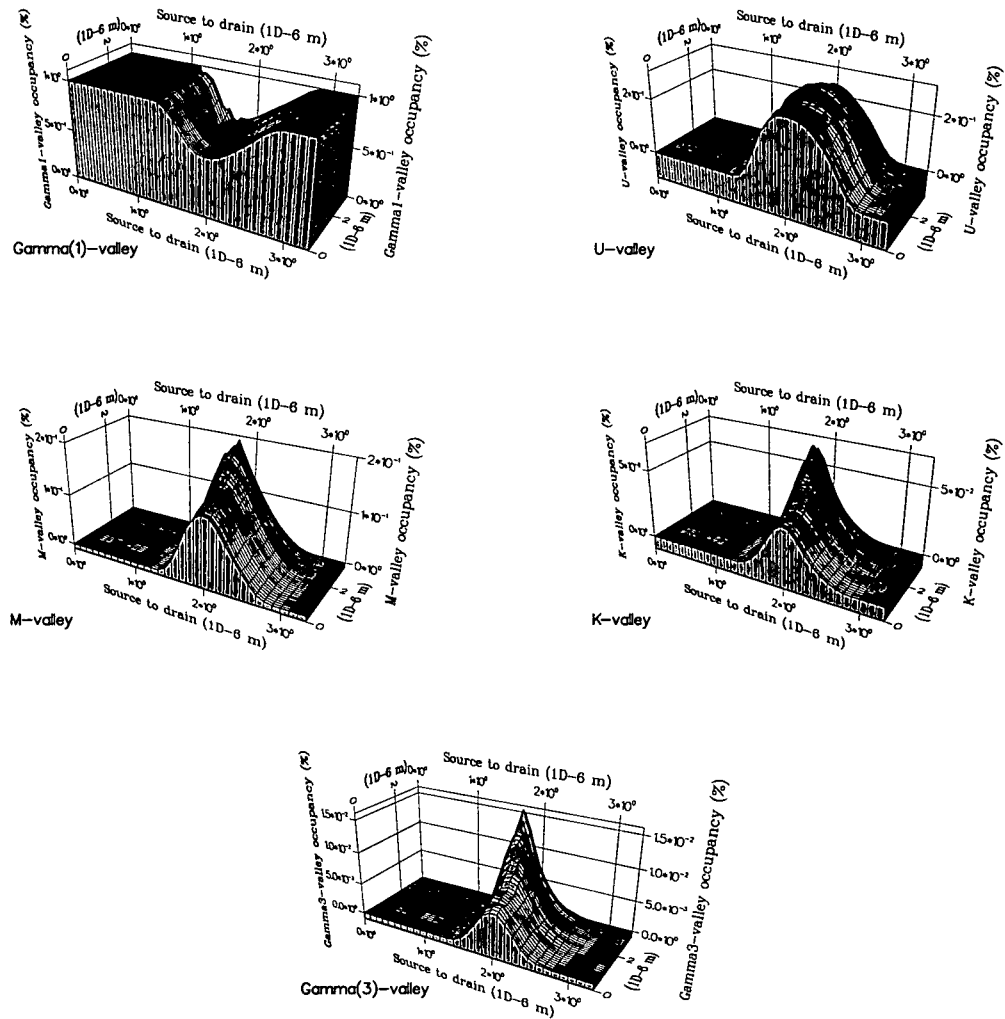
Figure 5.4: The valley occupation ratios for the central Γ_1-valley and upper valleys when the source-drain bias is 50 V and the gate voltage is -1 V at $T = 300$ K.
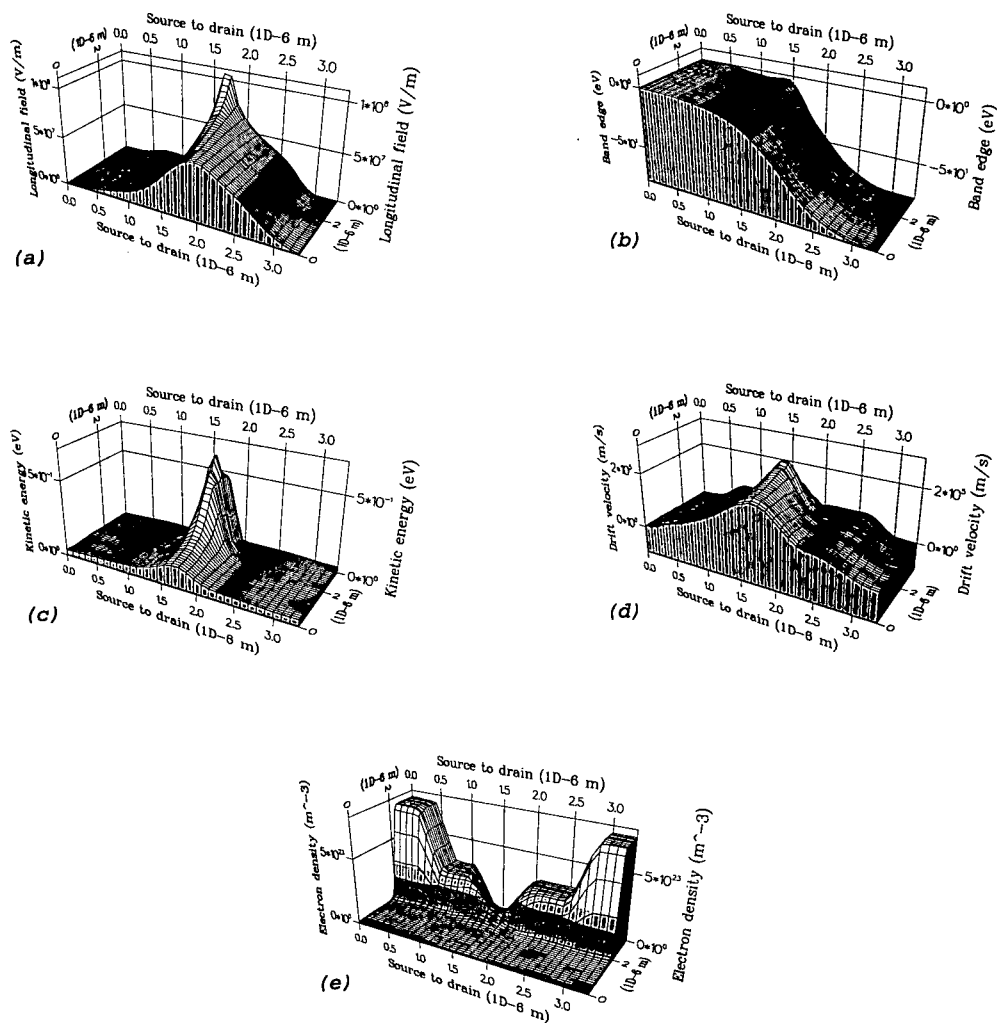
Figure 5.5: Three dimensional distribution of electron data recorded through the simulation of the GaN MESFET when the source-drain bias is 50 V and the gate voltage is −1 V at room temperature. This figure shows: (a) Longitudinal electric field, (b) Γ-valley conduction band profile, (c) Average kinetic energy, (d) Drift velocity and (e) Electron density.

5.4.1 Gate-length effect

The effect of gate length on electron transport in GaN MESFETs has been studied. Figure 5.6 illustrates the average electron velocity through the device as a function of distance along the channel for various gate lengths. It is apparent from this figure, that higher velocities are reached as the gate length is reduced as a result of the increase in longitudinal electric field and velocity overshoot effects. It follows that the electron transit time under the gate is reduced in two ways; there is a reduction in the transit length and also the electron velocity is larger.

The high value of the field at the source-end of the gate is responsible for the almost ballistic acceleration of the electrons as soon as they enter the channel region under the gate. Figure 5.6 shows also that the velocity overshoot reaches its maximum around the centre of the gate, but drops rapidly because of the occurrence of intervalley transfer. As a result, shorter gates lead to higher cutoff frequencies but they are also expected to lead to smaller breakdown voltages. Impact ionization is not included in the simulation model and breakdown is not considered here.

Figure 5.6: Average electron velocity in the simulated GaN MESFET with different gate lengths when the source-drain bias is 50 V and the gate voltage is -1 V at $T = 300$ K. (Note the source end of the gate is kept in the same place)

5.4.2   *I-V* characteristics
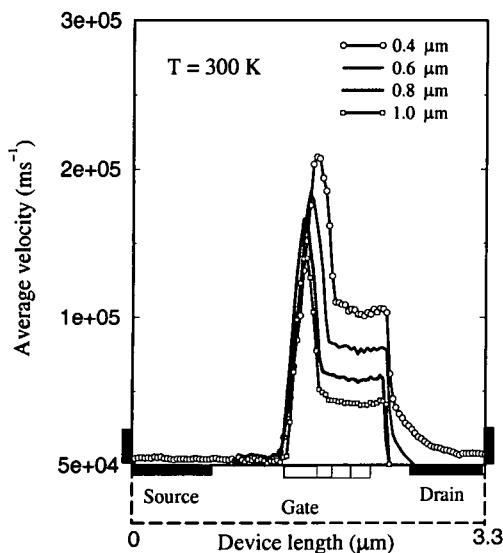
The drain current is obtained by counting the net charge flow through the drain contact. Figures 5.7a and 5.7b show the calculated drain current versus drain-source voltage at different gate biases for temperatures of 300 K and 420 K. Figure 5.7c shows the experimental results for the same device obtained by Trassaert *et al.* [73] at 300 K and a further presentation of the simulation results to facilitate comparison. The simulated characteristics at 300 K show good saturation behaviour with a knee voltage around 20-30 V and a saturation drain current of about 2200 mA mm^{-1} for $V_{gs} = 0$ V. The high drain current density is encouraging for the use of GaN for high-power applications [88].

From figure 5.7a it is clear that the device is not completely pinched-off even at large negative gate bias ($V_{gs} = -15$ V) which is due to strong electron injection into the buffer layer at high electric fields. An increasing fraction of the drain current flows through the buffer as the drain voltage increases. At $V_{ds} = 80$ V essentially the whole drain current flows entirely through the buffer. To obtain some idea of the effect of high temperature on GaN MESFETs, simulations were carried out at $T = 420$ K, keeping the other device parameters unchanged. The *I-V* curves obtained are shown in figure 5.7b. Comparing the *I-V* curves at $T = 300$ and 420 K, it can be seen that the drain current is somewhat lower at the higher temperature, due to increased phonon scattering, but the effect is not major. The transconductance of the MESFET is given by

$$g_m = \frac{\Delta I_d}{\Delta V_g} \Big|_{V_d} \tag{5.1}$$

and is calculated from figure 5.7a to be about 140 mS mm^{-1} at 18 V drain bias and -1 V gate voltage for room temperature. When the drain bias is increased to 50 V at the same gate voltage, the transconductance increases approximately to 200 mS mm^{-1}. In comparison, good GaAs MESFETs without a gate recess have a transconductance around 110 mS mm^{-1} [90–92]. The higher value of transconductance in simulated GaN MESFET is related to a higher drain current.
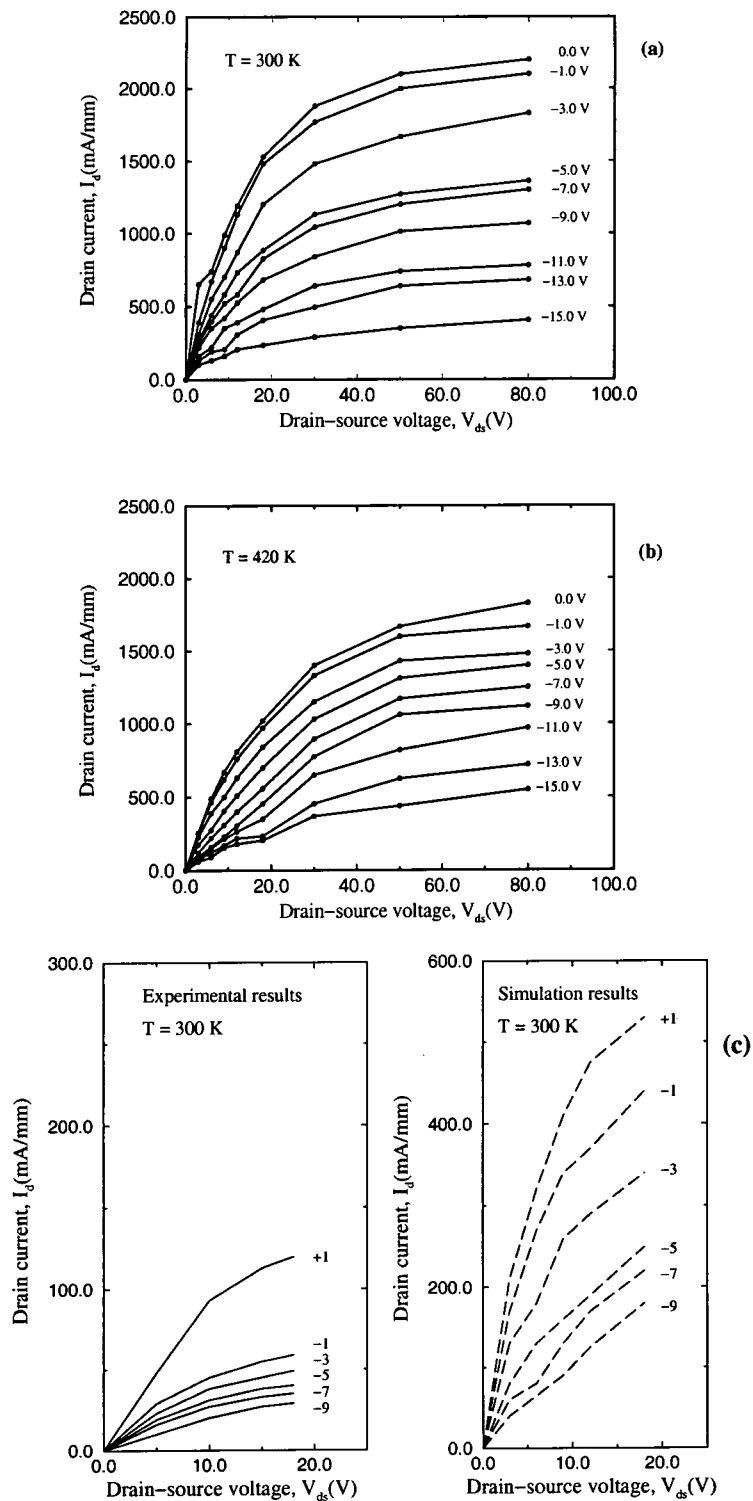
Figure 5.7: (a) The simulated drain current versus drain voltage at $T = 300$ K, (b) The simulated drain current versus drain voltage at $T = 420$ K and (c) Comparison of the experimental I-V characteristics for the same device at $T = 300$ K [73] with the simulated device.

Figure 5.7c shows the general shape of the simulated *I-V* characteristics is similar to the experimental measurements but the predicted drain currents are higher. Trassaert *et al.* [73] have suggested that the existence of traps in GaN crystals can be responsible for lower currents than expected in theoretical calculations. Therefore, in the next section we discuss simulations performed with the specific aim of studying the effects of trapping on the electronic transport behaviour and electrical characteristics of GaN MESFETs.

5.5 Trapping effects in GaN MESFETs

Our Monte Carlo simulations of GaN MESFETs show higher drain currents than seen in experiment. The discrepancy might be explained by electron trapping effects which are thought to play an important role in the electrical properties of GaN devices due to the current limitations of the material technology. Therefore, it is of particular interest to use simulations to examine how certain trap levels affect the electronic transport properties of GaN-based MESFETs.

Trapping of electrons in GaN MESFETs has been the subject of several recent experimental investigations [95–97]. Researchers have used various methods to study trapping and detrapping of electrons in nitride devices. Binari *et al.* [96] were the first to observe that after a high drain bias was applied to a GaN MESFET in the dark, a significant reduction in drain current occurred in subsequent drain bias sweeps, while in the light a normal set of drain characteristics were observed. The behaviour in the dark is thought to result from the trapping of electrons by trap centres located in regions of the device structure outside of the conducting channel, such as the buffer layer. In the light, the electrons are quickly emitted from the traps, so a normal output drain current is observed. In the dark, however, the electrons remain trapped and a depletion region is formed in the lower side of the channel. This results in a large reduction in drain current which is called current collapse.

Current collapse depends on the trap centre parameters. Consequently, a knowledge of the relevant traps that exist in GaN material and devices is important. The most

important experimental techniques that have been used to detect and characterize traps in GaN and related materials include thermally stimulated current (TSC), deep-level transient spectroscopy (DLTS), and photoluminesence spectroscopy (PL) [44,98, 99]. The nitrogen vacancy has been discussed for a long time as being responsible for the traps in GaN [94, 95]. For example, Haase *et al.* [100] have reported that two trap centres with activation energies of 0.6 and 0.67 eV are associated with the nitrogen vacancy. A number of trap centres in GaN are due to the high dislocation densities in GaN layers. The main reason for these dislocations is the lack of a lattice-matched substrate because bulk GaN is difficult to grow in large sizes. The large lattice mismatch inherent in the use of the common substrates, SiC and sapphire, leads to high defects and dislocation densities which can create trap levels with activation energies in the range of $0.15-0.8$ eV and trap densities in the range of $10^{19}-10^{23}$ m^{-3} [101,102]. Table 5.1 gives the parameters of different trap levels in GaN crystals that have been measured by the DLTS, TSC and PL techniques, and which are candidates to be used in our simulations.

In the next section, we first give a brief review of the capture and emission processes which have been assumed in our model. This is followed by a description of how trapping is incorporated in the Monte Carlo simulation. Finally, we compare the results obtained for a GaN MESFET, including trap levels, with our previous results and with experiment. The effects of temperature, capture cross-section, trap density and trap energy have been investigated and their results are reported and discussed.

	ΔE_{trap} (eV)	σ_{trap} (m^2)	n_{trap} (m^{-3})	T_{trap} (K)
E_1	0.14	3.9×10^{-22}	1.8×10^{22}	120
E_2	0.30	2.0×10^{-19}	1.0×10^{23}	270
E_3	0.42	0.5×10^{-18}	0.5×10^{21}	290
E_4	0.50	5.0×10^{-20}	1.7×10^{20}	300
E_5	0.62	7.4×10^{-19}	3.0×10^{20}	330
E_6	0.73	1.0×10^{-19}	3.3×10^{21}	360

Table 5.1: Characteristics of different traps measured by DLTS, TSC and PL in GaN [44, 98, 99] used in our Monte Carlo simulation model. It is assumed in the simulation that the capture cross-sections are independent of temperature.

5.5.1 Trap model description

In the interests of simplicity it is assumed that there is just a single trap with associated energy level E_T in all or just part of the device. Further, it is assumed that only electrons may be captured from the conduction band by the trap centres, which have a capture cross-section σ_n and are neutral when unoccupied, and may only be emitted from an occupied centre to the conduction band. We use the standard model of carrier trapping and emission (see for example [103]).

Consider a local trap density N_T with a trapped electron density n_t and a conduction band electron density n. Only the empty traps with density $N_T - n_t$, can trap electrons and do so at a rate per unit volume $c_n n(N_T - n_t)$, where c_n is the capture coefficient. Trapped electrons are emitted at a rate $e_n n_t$ per unit volume where e_n is the emission coefficient. Therefore, the time rate of change of the conduction band electron density due to trapping and re-emission is given by

$$\frac{dn}{dt} = e_n n_t - c_n n(N_T - n_t) \tag{5.2}$$

For a Boltzmann distribution of electrons the capture coefficient c_n is related to the capture cross-section σ_n by

$$c_n = \sigma_n v_{th} \quad \text{where} \quad v_{th} = \left(\frac{3k_B T}{m^*} \right)^{\frac{1}{2}} \tag{5.3}$$

Here it is assumed these equations also hold under high field transport. In equilibrium the electron emission and capture rates must be equal [87, 104] and n is independent of time, giving

$$e_n n_t = c_n n (N_T - n_t) \tag{5.4}$$

Writing

$$n = n_i \exp\left(\frac{E_F - E_i}{k_B T}\right) \quad , \quad n_t = \frac{N_T}{1 + \exp(\frac{E_T - E_F}{k_B T})} \tag{5.5}$$

where E_i and n_i are the intrinsic Fermi level and electron density respectively, the emission coefficient is given by

$$e_n = \sigma_n v_{th} n_i \exp\left(\frac{E_T - E_i}{k_B T}\right) \tag{5.6}$$

It is apparent from equation 5.6 that an occupied trap centre will only have a significant emission probability above a characteristic temperature $T \simeq (E_T - E_i)/k_B$.

For the Monte Carlo simulation of electron transport in a GaN MESFET with trapping centre effects the following model has been constructed and incorporated into SLURPS. The superparticles in the ensemble Monte Carlo simulation are assumed to be of two types. There are mobile particles that represent unbound electrons throughout the device, as in all the simulations that have been discussed previously. However, the particles may also undergo spontaneous capture by the trap centres distributed in the device. The other type of superparticles are trapping centres that are fixed at the centre of each mesh cell. As illustrated in figure 5.8, each trap centre has the capacity to trap a finite amount of mobile electronic charge from particles that are in its vicinity and reside in the lowest conduction band valley. The vicinity is defined as exactly the area covered by the electric field mesh cell. The finite capacity of the trapping centre in each cell of a specific region in the device is set by a trap density parameter in the simulation programme. The simulation itself is carried out by the following sequence of events. First, the device is initialized with a specific trap which is characterized by its density as a function of position, a trap energy level and a capture cross-section. Then at a specific gate bias the source-drain voltage is applied. Some of the mobile charges passing from the source to the drain in each timestep can be trapped by the centres with a probability which is dependent on the trap cross-section and particle
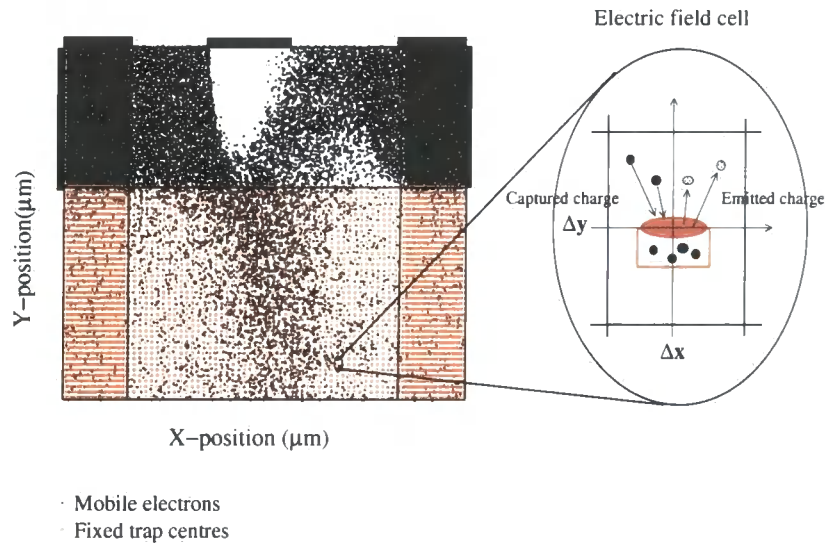
Y-position(μm)

X-position (μm)

Electric field cell

Captured charge   Δy   Emitted charge

Δx

· Mobile electrons
· Fixed trap centres

Figure 5.8: The instantaneous distribution of 10^4 particles at steady forward bias (drain voltage 50 V, gate voltage -1 V), superimposed on the mesh. Note that in the simulation there are two types of super-particles. The mobile particles, which describe unbound electrons, flow through the device and trapping centre particles which are fixed at the centre of each electric field cell (in this case in the buffer layer only). The ellipse represents a trap centre which is fixed at the centre of an electric field cell and occupied by some mobile charges.

velocity in the cell occupied at the relevant time t. The quantity of charge that is captured from a passing mobile particle is the product of this probability and the charge on it. This charge is deducted from the charge of the mobile particle and added to the fixed charge of the trap centre. If a particular trap captures some charge in a field adjusting timestep, no further charge can be captured until some numerically performed emission of charge occurs in that timestep. The emission of charge is simulated using the emission probability of equation 5.6. Any charge emitted from a trap centre is distributed evenly to all mobile particles in the same field cell. Such capture and emission simulations are performed for the entire mesh in the device and information on the ensemble of particles is recorded in the usual way. It is recognized that there are regions of high electric field in GaN MESFETs operating under normal conditions and

that the field could have a significant effect on the capture and emission of electrons by the traps. However, in the absence of an established model of the electric field effect it has been neglected in the simulations. It would be straightforward to include any field effect model since the local electric field is part of the data produced by the simulation.

5.5.2 High-field electron trapping results

Our simulations of devices with trapping effects are based on the geometry of the GaN MESFET described in sections 5.3, enabling a comparison of the electrical properties with and without trap centres. In the absence of any firm information on trap distribution throughout the device, we have looked at a number of different possibilities. Trassaert et al. [73] assumed that a reduction in the drain current is due to the existence of electrical traps localised in the GaN material. Therefore, to make a comparison with the experimental results obtained by Trassaert's group, it is assumed that the trap centres exist throughout the whole device with a density of 10^{23} m^{-3}. Also, it is assumed that the trap centres have an energy ΔE_{trap} of 0.3 eV with capture cross-section of 2×10^{-19} m^2 (E_2 in table 5.1).

The calculated drain current versus drain voltage for gate voltages varing from zero to -15 V are shown in figure 5.9 for devices at 300 K and 420 K. Not surprisingly the drain currents at both temperatures are lower than in the trap-free device (figures 5.7a and 5.7b) at all gate voltages. For example, the calculated maximum drain current at $V_{ds} = 80$ V and $V_{gs} = 0$ is about 650 mA mm^{-1} at $T = 300$ K, whereas for the trap-free device it was about 2200 mA mm^{-1}. The reasons for a large reduction in drain current can be explained by considering the effects of electron trapping. On applying drain bias, electrons passing from source to drain will have a certain probability of being captured. Emission of trapped electrons will also occur with a certain probability and in the steady-state there will be a density of trapped electrons determined by the balance between capture and emission. Hence, for any given electron there will be additional processes of electron capture and re-emission during electron transport and the effective transit time will be increased. In addition the trapped electrons cause space charge which acts to reduce the drain current. Figure 5.9b also shows that there is an increase
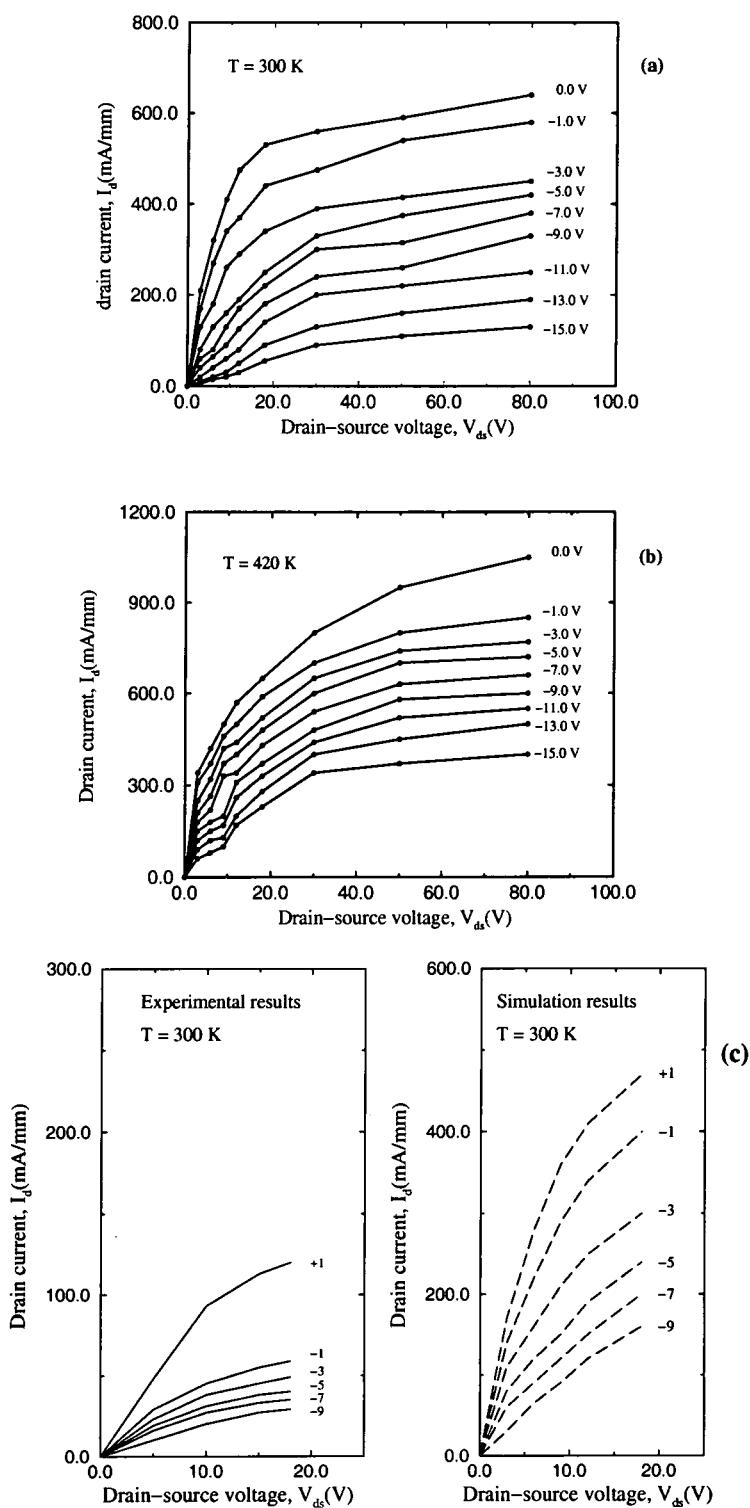
Figure 5.9: Simulated current-voltage characteristic for the GaN MESFET at (a) $T = 300$ K and (b) $T = 420$ K when trap centres exist in whole device. (c) Comparison of the the experimental I-V characteristics for the same device at $T = 300$ K [73] with the simulated device when trap centres exist in whole device.

in current as the temperature is increased from 300 K to 420 K. This is because, at higher temperatures the emission probability of trapped electrons is increased and the density of trapped electrons is lower. Comparison with the experimental results of Trasseart *et al.* [73], illustrated in figure 5.9c, shows that our simulated model are in much closer agreement than before traps were included.

Binari *et al.* [89, 104] have carried out most of the experimental observations of trapping effects in GaN MESFETs. Their results are based on the trapping of hot electrons by traps located in regions of the device structure outside of the conducting channel. Therefore, the effect of traps distributed in the buffer layer is discussed in the next section.

5.5.3   Effect of trap centres in buffer layer

To obtain some idea of the effect of traps in the buffer layer, we have also simulated the same GaN MESFET with trap centres present only in the buffer layer, at a density of 10^{23} m^{-3}. Electrons trapped in the buffer layer produce a negative charge space which acts to create a depletion region and hence narrow the channel causing a reduction in drain current.

Figure 5.10 shows the predicted *I-V* characteristic when the device gate voltage is -5 V. The figure also shows the equivalent characteristic for devices with no traps and with traps in both the active and buffer layers. Not surprisingly there is a lower drain current when there are traps present. However, it is apparent that the majority of current suppression is due to trap centres in the buffer layer. Analysis of the characteristics for the simulated devices show that the transconductance is lower than for the trap-free device at 62 mS mm^{-1} with traps throughout and 75 mS mm^{-1} with traps in the buffer layer only.

The density of trapped electrons is illustrated in figure 5.11 for different drain voltages at -5 V gate bias. Note, when there are traps throughout the device, the magnitude of the trapped electron concentration in the channel is several orders higher than in the buffer at low bias. However, the trapped density in the buffer layer increases with drain voltage and eventually exceeds that in the channel under the gate
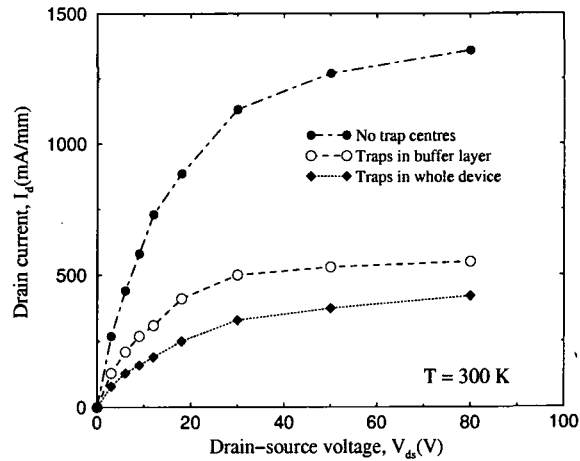
Figure 5.10: A comparison of *I-V* characteristics for the simulated GaN MESFET with no trap centres, trap centres in the whole device and trap centres in buffer layer with a −5 V gate voltage at room temperature.

and between the gate and the drain.

5.5.4 Effect of capture cross-section

The experimental data for the DC drain characteristics of GaN MESFETs show that differences in trap location and the corresponding capture cross-section may lead to different output drain characteristics [96]. In this section, we consider GaN MESFET characteristics calculated using different capture cross-sections.

To investigate the possible effects of capture cross-section on the characteristics of GaN MESFETs, we have performed Monte Carlo simulations for different values of the capture cross-section, keeping all other trap centre parameters unchanged. Also, because of the buffer layer's potentially important role in high-field trapping effects, it is assumed in the simulations that the trap centres are only in the buffer layer with a density of 10^{23} m^{-3}. The simulated current-voltage characteristics measured for different capture cross-sections at −5 V gate bias are plotted in figure 5.12.

In general the drain current decreases with increasing trap cross-section. However, there is a more marked change in the saturation current as the cross-section changes from 10^{-20} m^2 to 10^{-19} m^2 than for the change from 10^{-19} m^2 to 10^{-18} m^2. The

Trap centres in whole device   Trap centres in buffer layer
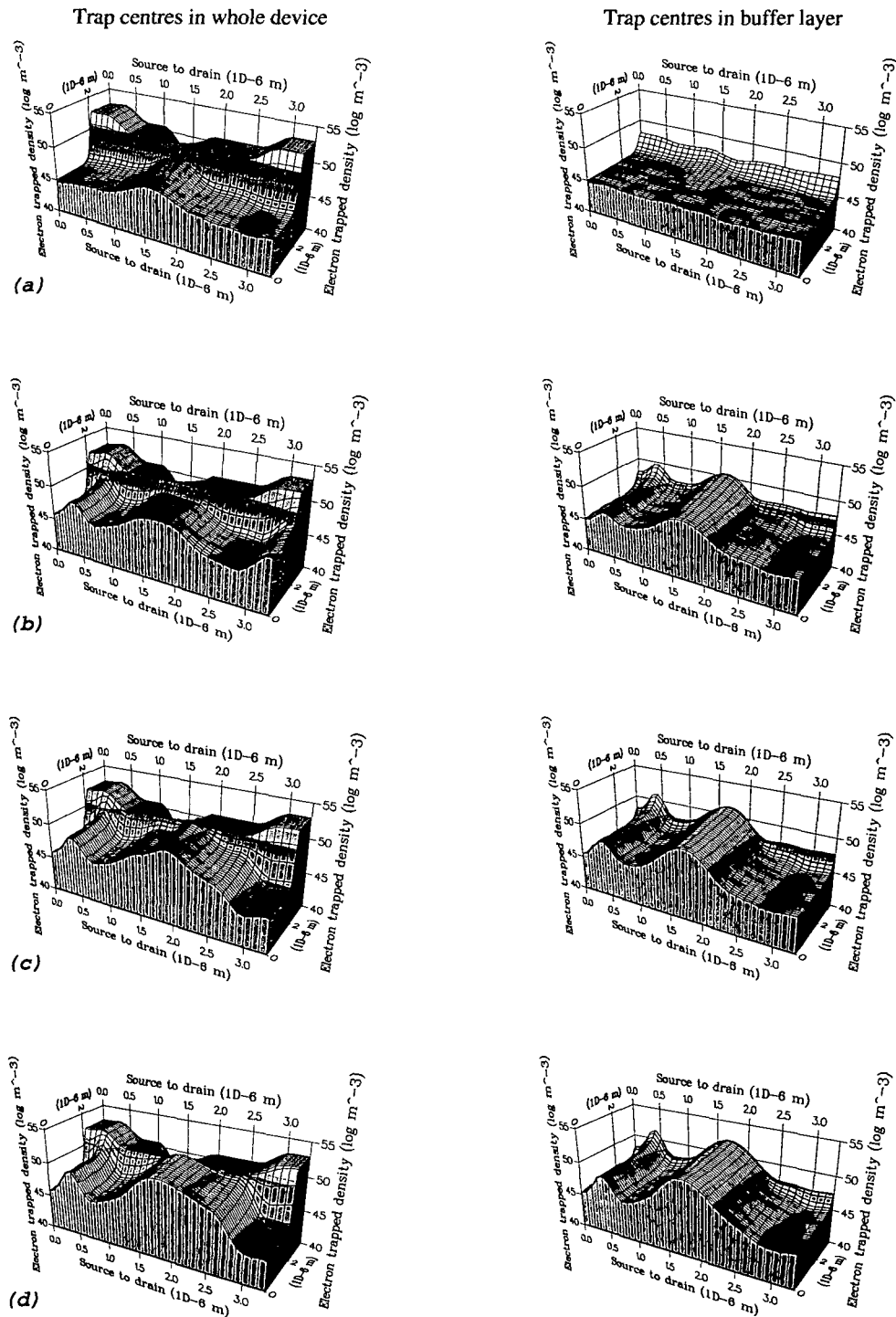

Figure 5.11: Logarithmic distribution of trapped electrons when the trap centres are distributed through the whole device or just in the buffer layer at $T = 300$ K and -5 V gate bias. (a) 6 V drain bias, (b) 18 V drain bias, (c) 30 V drain bias and (d) 50 V drain bias.
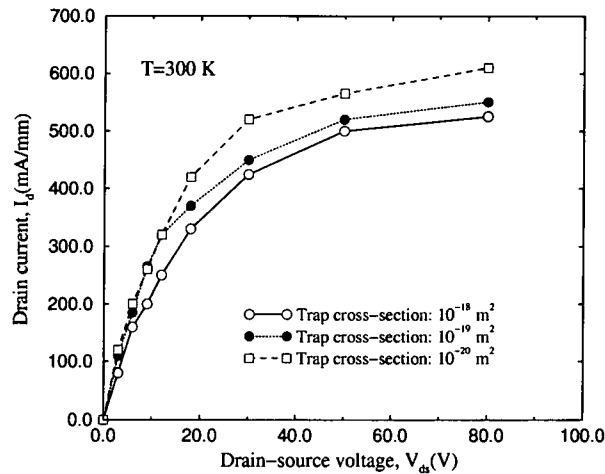
Figure 5.12: A comparison of I-V characteristics for a simulated GaN MESFET for different capture cross-sections and -5 V gate voltage at room temperature.

reason for this behaviour may be explained by reference to the trapped electron density diagrams in figure 5.13. For the large capture cross-sections ($\sigma \sim 10^{-18} - 10^{-19}$ m^2) there is a substantial region where almost all traps are occupied, which extends through the buffer layer. The associated depletion region extends through the channel and affects the potential in the buffer layer, resulting in a large reduction in drain current.

5.5.5 Effect of trap centre energy

In general we expect traps with energies close to the conduction band edge to be less effective in trapping electrons. Consequently, shallow level traps centres tend to have less effect on the I-V characteristics than deep level centres. To predict the effect of trap energy on device performance, we have performed simulations for both shallow and deep level traps, with energies ranging from 0.3 to 2.85 eV. Figure 5.14 compares the simulated drain currents obtained for various trap energies. It can be seen that as the trap level moves closer to the conduction band the drain current increases but the effect is not particularly large.
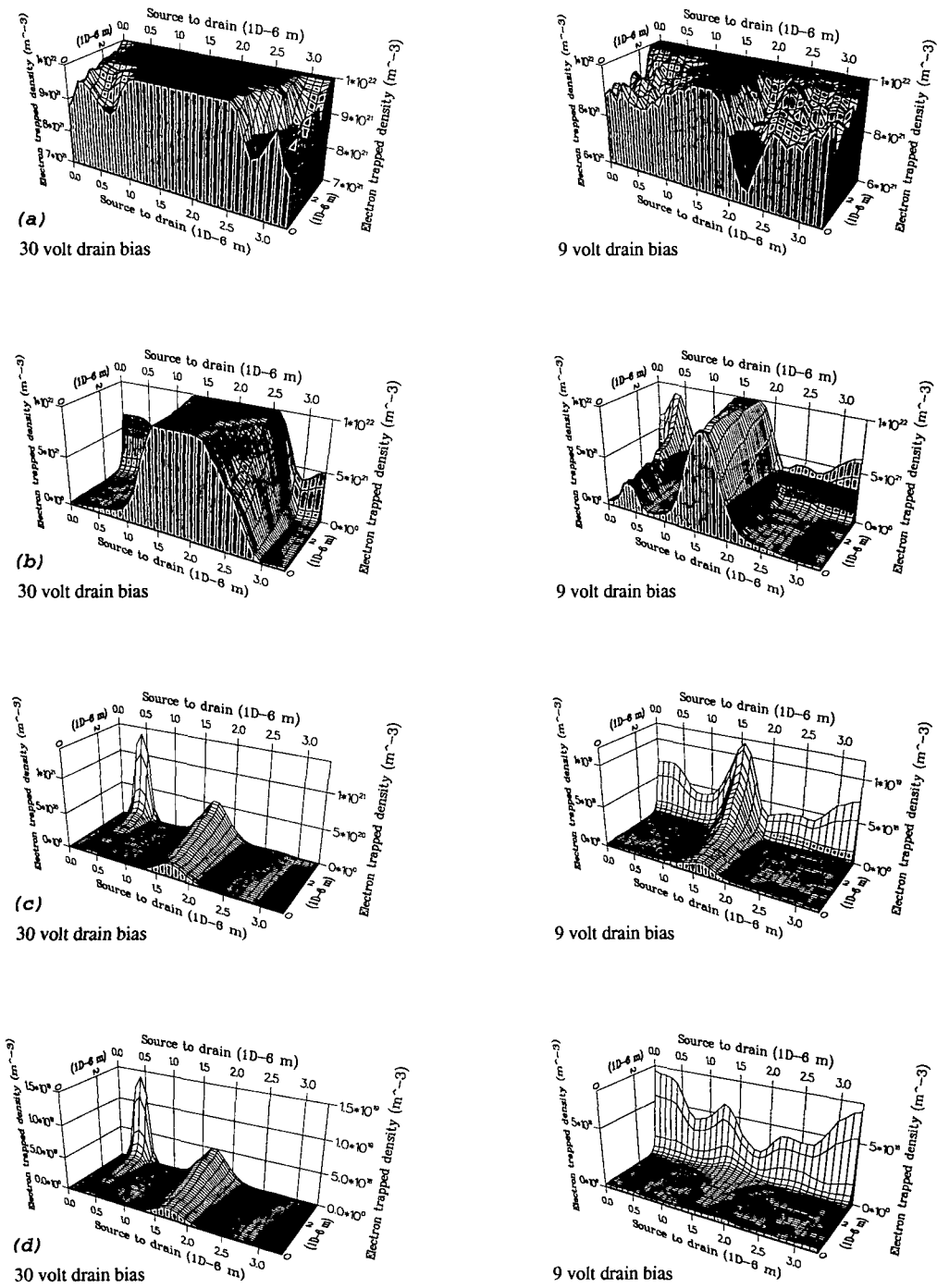
Figure 5.13: Distribution of the electron trapped density for different capture cross-sections at $T = 300$ K and -5 V gate bias. (a) $\sigma \sim 10^{-18}$ m^2, (b) $\sigma \sim 10^{-19}$ m^2, (c) $\sigma \sim 10^{-20}$ m^2 and (d) $\sigma \sim 10^{-21}$ m^2.
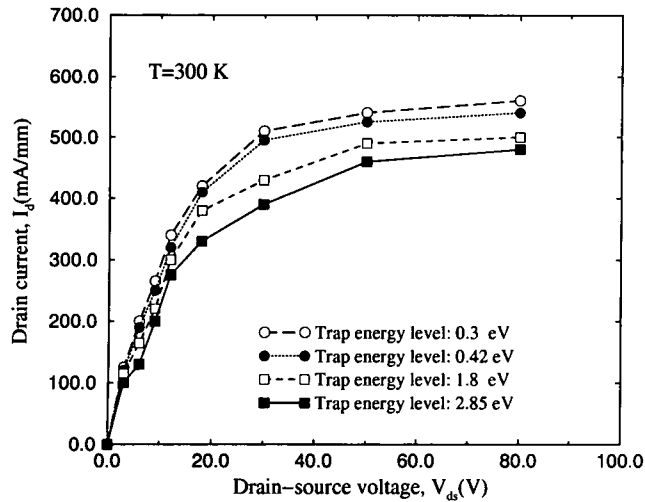
Figure 5.14: A comparison of *I*-*V* characteristics for the simulated GaN MESFET for different trap energy levels and -5 V gate voltage at room temperature. It is assumed that the capture cross-section is about 10^{-19} m^2.

5.5.6   Effect of trap centre density

To examine the effect of trap centre density on the characteristics of GaN MESFETs, we have performed Monte Carlo simulations for a trap capture cross-section of 2×10^{-19} m^2 and density varying from 10^{21} to 10^{24} m^{-3} in the buffer layer only.

Figure 5.15 shows how the drain current decreases with increasing trap density due to the higher trapped electron density which is apparent in figure 5.16.

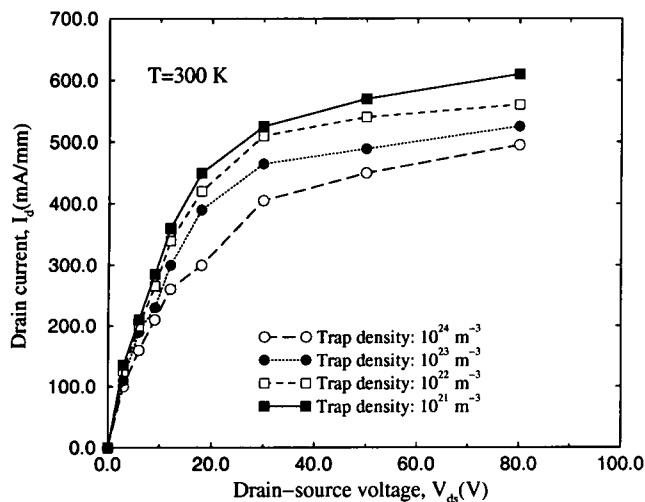**Figure 5.15:** A comparison of *I*-*V* characteristics for the simulated GaN MESFET for different trap centre densities with a -5 V gate voltage at room temperature.
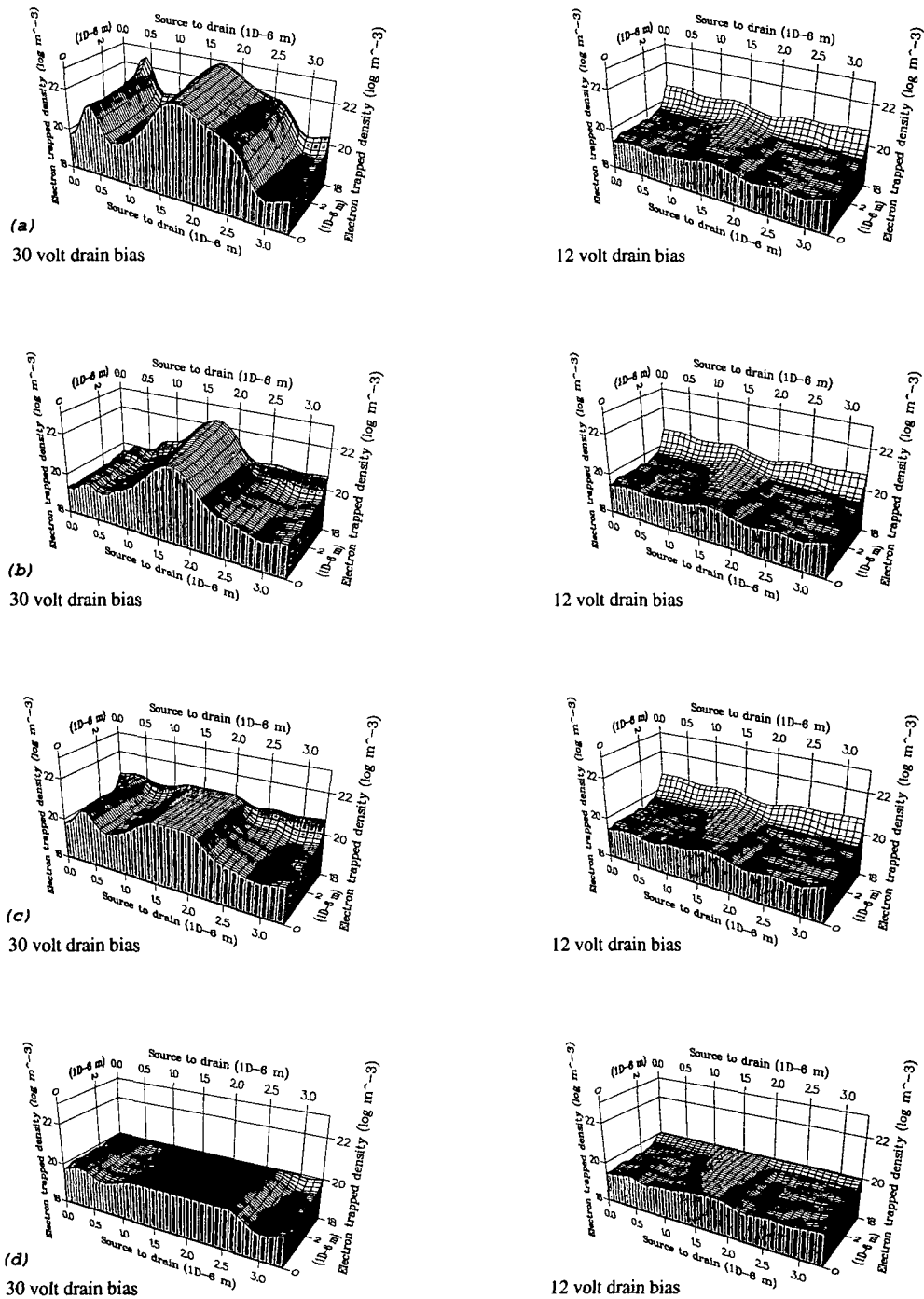
Figure 5.16: Logarithmic distribution of the electron trapped density for different density of trap centres at $T = 300$ K and -5 V gate bias. (a) 10^{24} m^{-3}, (b) 10^{23} m^{-3}, (c) 10^{22} m^{-3} and (d) 10^{21} m^{-3}.

5.5.7   Photoionization of traps in GaN FETs

As we saw earlier, the application of a high drain-source voltage causes hot electrons to be injected into the buffer layer where they are trapped by trap centres. The trapped electrons produce a depletion region in the channel of the GaN MESFET which tends to pinch off the device and reduce the drain current. This effect can be reversed by any factor which substantially increases the electron emission rate from the trapped centres, such as the elevated temperatures considered previously. Here we consider the effect of exposure to light [105].

There have been several experimental investigations of the influence of light on the device characteristics. Binari *et al.* [11,70,96] were the first to study experimentally the current collapse in GaN MESFETs as a function of temperature and illumination. They showed that the photoionization of trapped electrons in the high-resistivity GaN layers and the subsequent return of these electrons to the conduction band could reverse the drain current collapse. Their measurements were carried out as a function of incident light wavelength with values in the range 380 nm to 720 nm, corresponding to photon energies up to 3.25 eV which is close to the GaN band gap. Their results show that when the photon energy exceeds the trap energy, the electrons are quickly emitted and a normal set of drain characteristics are observed.

To examine the photoionization effect in our simulations, the thermal emission rate e_n^t was changed to $e_n^t + e_n^o$, where $e_n^o \sim \sigma_n^o \Phi$ is the optical emission rate, with σ_n^o, the optical capture cross-section and Φ the photon flux density given by

$$\Phi = \frac{I}{h\nu} = \frac{I\lambda}{hc} \tag{5.7}$$

where I is the light intensity, ν is the radiation frequency and λ is the incident light wavelength.

Here our modelling of photoionization effects in GaN MESFETs is based on parameters used by Binari and Klein [106]. The simulations were all carried out for two different deep trap centres, both with a concentration of 10^{22} m^{-3}, and with photoionization threshold energies at 1.8 and 2.85 eV and capture cross-sections of 6×10^{-21} m^2 and 2.8×10^{-19} m^2, respectively. A fixed incident light intensity of 5 Wm^{-2} at

photon energies of 2.07 eV and 3.1 eV is used. The simulations have been performed at a sufficiently high temperature (420 K) for both thermal and optical emission to be significant as well as at room temperature.

Figure 5.17a illustrates the effect on the drain current characteristics of exposure of the device to light at room temperature. The GaN MESFET has a deep trap centre at 1.8 eV and is illuminated at a photon energy of 2.07 eV. It can be seen that in the light the *I-V* curves generally exhibit a larger drain current, especially at higher drain voltages, reflecting the fact that the density of trapped electrons is much lower.

Simulations have also been performed at 420 K for a device with deep level traps at 2.85 eV. The simulation results in figure 5.17b for illumination of a photon energy of 3.1 eV are compared with the collapsed *I-V* curves in the absence of light. Comparison of figures 5.17a and 5.17b shows that the currents are generally higher at 420 K and that the light has less effect at the higher temperature.

5.6 Frequency response

In addition to modelling the steady-state DC characteristics, simulations have also been carried out to obtain the intrinsic cutoff frequency f_T^i corresponding to unit current gain, which is defined as the ratio of drain current to the gate current. The frequency response of a transistor is related to the transit time of the charge carriers across the channel and, since electrons in GaN have a saturation velocity of greater than 2×10^5 ms^{-1}, we can expect that quite high frequency operation is possible in GaN MESFETs. The method used to investigate the frequency response of the GaN MESFET follows that of Crow *et al* [107]. We applied a truncated sinc voltage pulse to the gate contact. A 1000 picosecond duration sinc pulse containing ten minicycles has the specific advantage of having a flat frequency spectrum up to 100 GHz, with 10 GHz resolution. The simulation was performed with 50,000 particles at −1 V gate voltage, which provides the maximum transconductance at 18 V drain-source bias. This bias arrangement should therefore maximize the device response, providing an upper estimate for the cutoff frequency. Traps are included in the simulation to be

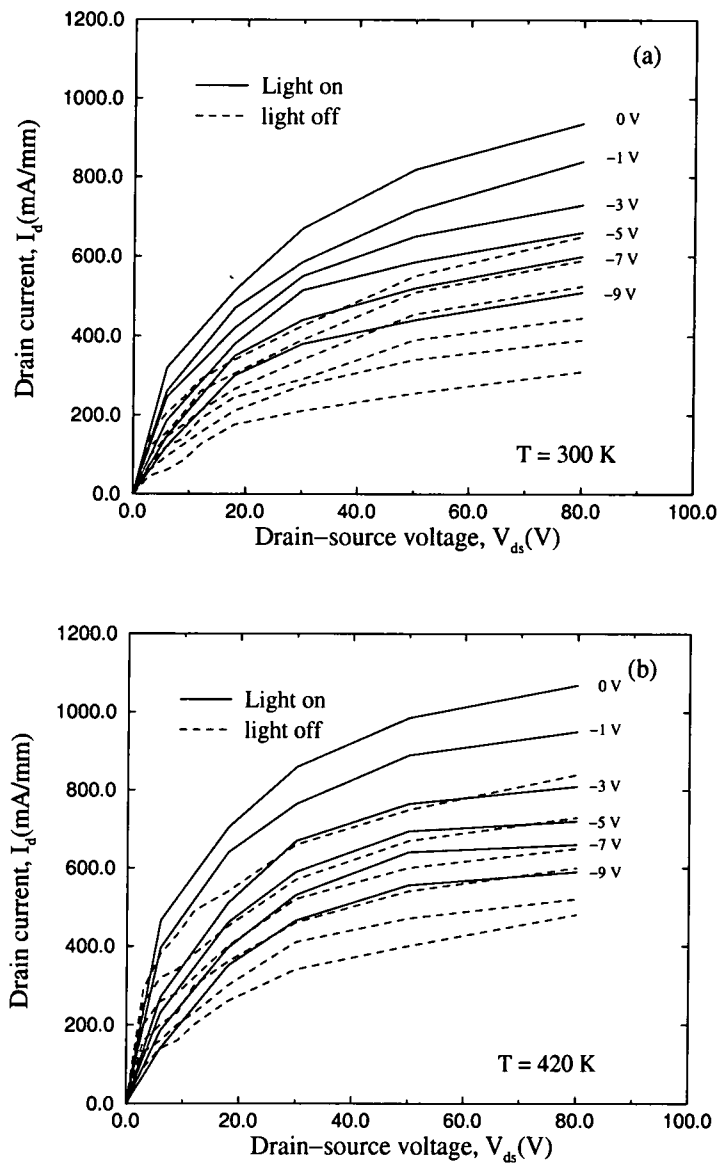**Figure 5.17:** *I-V* Characteristics of a GaN MESFET under optical and thermal emission of trapped electrons (solid curve) and thermal emission of trapped electrons (dashed curve) at two different temperatures. (a) At $T = 300$ K with trap centres at 1.8 eV and illuminated with a photon energy of 2.07 eV. (b) At $T = 420$ K with trap centres at 2.85 eV and illuminated with a photon energy of 3.1 eV.

able to get the results under the real device conditions. We have assumed that trap E_4 in table 5.1 exists throughout the buffer layer.

The simulated frequency response of the GaN MESFET to the gate voltage pulse is plotted in figure 5.18. This figure shows the gate voltage as a function of time for a truncated pulse of duration 1000 ps, the drain current response, the source current response and the gate current, which is mainly electric displacement current.
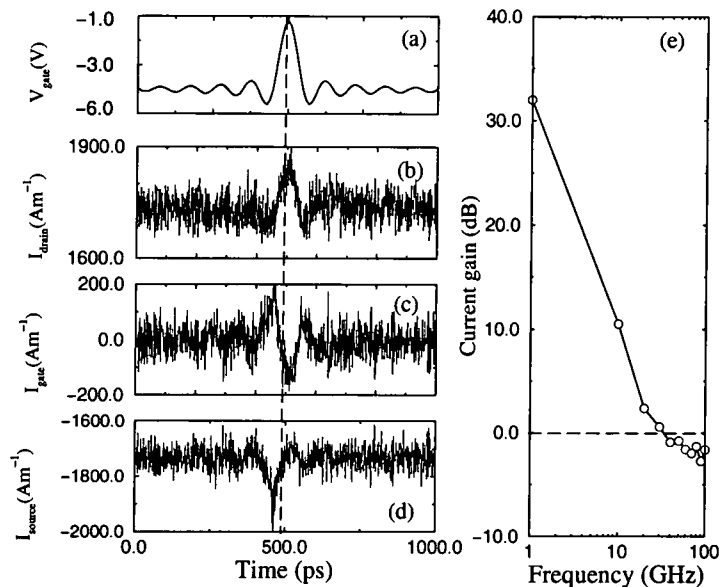
Figure 5.18: The simulated frequency response of the GaN MESFET to a sinc gate voltage pulse. From top to bottom this figure shows the gate voltage (V_{gate}), the drain current (I_{drain}), the gate current (I_{gate}) and the source current (I_{source}). The maximum intrinsic current gain is shown in the logarithmic plot on the right hand side.

The value of the current gain shown in figure 5.18e has been derived as a function of frequency by taking fast Fourier transforms of the simulated drain and gate current signals, then obtaining the ratios of the coefficients of the drain and gate current transforms. It is evident from figure 5.18e that the cutoff frequency for the simulated GaN MESFET is about 25 GHz. The simulation predicts also the current gain of 1 GHz is about 32 dB, which for our 0.3 μm gate device is broadly in line with the experimental result of Dessenne *et al* [108] who obtained a cutoff frequency of 80 GHz

for a GaN MESFET with gate width of about 0.12 μm. The results indicate that GaN MESFETs have good bandwidth capability and have good potential for microwave power applications.

5.7 Conclusions

The operation of GaN MESFETs with and without trapping levels has been simulated by the Monte Carlo method. The microscopic features of the steady-state, such as electron distribution velocities and trapped electron density, as well as the device *I-V* characteristics have been described and explained. We have shown that including traps can result in a significant reduction in the drain current of GaN MESFETs. Since the filled traps can be emptied by both increased temperature (thermal excitation) and illumination (photoionization), their effects in relation to current collapse have been discussed separately. Our results show that as the temperature is increased the collapsed drain current curve moves towards the non-collapsed curve due to the increased rate of emission of trapped electrons at higher temperatures. Although the simulated output drain current is roughly two to three times larger than the experimental results, the effects of trap centres on device performance are similar to those in the experimental studies. In the absence of any firm information on what traps exist and where in the experimental device, the simulations have been performed with trap centres distributed in the whole device or just in the buffer layer. It is found that the majority of current suppression is due to trap centres in the buffer layer.

We have also investigated the effects of different capture cross-sections, trap densities and trap energy levels on the characteristics of GaN MESFETs. The simulation results show that deeper traps produce higher current collapse in comparison to shallow centres. Not surprisingly the simulation results show that increasing the trap density and trap cross-section decrease the output drain current. Finally, we have studied the frequency response of the device by applying a voltage to the gate. The currents at the contacts have been obtained as a function of frequency and the results suggest an intrinsic cutoff frequency of around 25 GHz for the device considered.
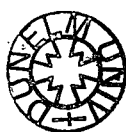
Chapter 6

Simulation of GaN HFETs

6.1 Introduction

It has already been shown in the previous chapter that GaN based MESFETs have properties that suggest they are good candidates for high-power and high-temperature applications. It was demonstrated that MESFETs fabricated from GaN can also offer good microwave power performance, and superior performance at elevated temperatures compared to similar devices fabricated from GaAs and related materials. In the search for even greater power and speed performance, recent experimental investigations have indicated that AlGaN/GaN heterojunction field effect transistors (HFETs) show better performance due to the high sheet carrier concentration that can be achieved in the channel because of large band discontinuities and piezoelectric polarization charge at the relevant interfaces [109–111]. In particular, such devices can show better high frequency gain than GaN based MESFETs. Furthermore, the piezoelectric properties of GaN and AlN can form the basis of a wider range of optoelectronic components, including pressure sensors [112]. In a typical AlGaN/GaN HFET, the AlGaN barrier is grown on top of a thick GaN layer. The lattice constant of GaN is about 2.5% larger than that of AlN. The AlGaN layer is assumed to be grown pseudomorphically, with a biaxial tensile strain in the plane of the epitaxial layer and a compressive strain along its hexagonal c-axis. This strain results in a substantial piezoelectric field whose magnitude is roughly 6×10^7 Vm^{-1} in pseudomorphic $Al_{0.2}Ga_{0.8}N$ [113]. Unfortunately,

as with MESFETs, the epitaxial growth of the GaN layer on SiC or sapphire substrates results in a large density of threading dislocations, which can significantly affect the performance of the transistors.

In this chapter we describe two dimensional Monte Carlo modelling of strained $Al_{0.2}Ga_{0.8}N$/GaN heterojunction field effect transistors, paying particular attention to the effects of the large polarization charges which arise from the strain in the alloy. In section 6.2 we present the geometry of the simulated HFET. Understanding of strain effects on nitride heterojunctions is necessary to optimise the performance of nitride HFETs. Thus some details of strain effects in conventional group III-V semiconductors has been explained in section 6.3. Section 6.4 describes the Monte Carlo model which has been used to study the piezoelectric polarization effects across the heterostructure interfaces. In section 6.5, the transport of electrons in the simulated GaN HFET under bias conditions and the main macroscopic results are presented and discussed. We summarize the chapter in section 6.6, together with the main conclusions of our study.

6.2   Device geometry

The device considered is the $Al_{0.2}Ga_{0.8}N$/GaN HFET illustrated in figure 6.1, which is similar to that studied experimentally by Khan and Yang [110]. It is assumed that the orientation of the c-axis of the wurtzite crystal structure is normal to the surface of the device. The device consists of a 78 nm top AlGaN layer with doping density of 5×10^{23} m^{-3} grown on GaN with a doping density of 10^{23} m^{-3}. The overall device length is 3.5 μm (in the x-direction) with a 0.45 μm gate length and source to gate and gate to drain separations of 0.8 μm and 1.25 μm, respectively. A Schottky barrier height of 1 eV has been used for the Au/Pt gate. The side contacts in figure 6.1 are intended to represent the remainder of the ohmic source and drain pads in the real device.
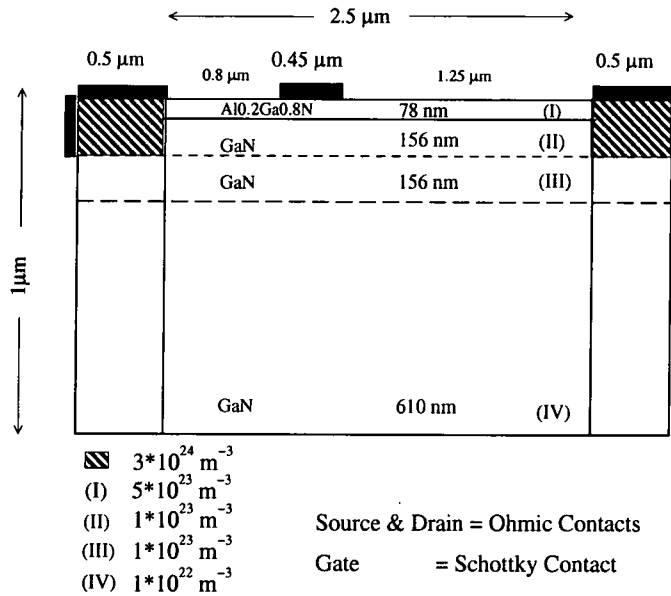
Figure 6.1: Cross section of the $Al_{0.2}Ga_{0.8}N$/GaN structure which we have chosen in our simulation. Source and drain contacts have low resistance ohmic contacts, while the gate contact forms a Schottky barrier between the metal and the semiconductor epilayer.

6.3 Strain effects in the nitride heterostructures

In group-III nitride heterostructures one of the layers is usually strained because there is normally a significant lattice mismatch between the different materials. Strain effects are generally very important in determining the properties of nitride heterojunctions. This is because in addition to the direct effect of strain on the band structure, the wurtzite crystal structure means that the strain is accompanied by substantial piezo-electric effects. Therefore, from the point of view of device design, an understanding of strain and the associated piezoelectric effects is necessary to optimise performance. The materials that make up the device can be chosen to take advantage of piezoelectric effects but at the same time it is necessary to consider the band offset that is required to optimise electronic transport. Thus, in the following section we give a brief review of the theory of strain and the accompanying piezoelectric effects in nitride materials.

6.3.1   Strain theory

A full discussion of the theory of strain in semiconductor heterostructures can be found in for example, [114–116]. Here we present a brief summary of the key aspects of the theory. Figure 6.2a shows an epilayer, which as bulk material would have a lattice constant greater than that of the substrate. In pseudomorphic growth, the atoms of the epilayer material align themselves with those of the substrate which causes a biaxial compressive strain in the plane of the layer and a strain of opposite sign parallel to the growth direction. However, when the epilayer thickness exceeds some critical value, the elastic energy is such that the generation of dislocations is preferred to pseudomorphic growth. Although the thickness of the $Al_{0.2}Ga_{0.8}N$ layer used in the simulated device shown in figure 6.1 is above the critical thickness estimated from the Matthews-Blakeslee model [117] or the Fischer model [118], there are reports of pseudomorphic growth in layers up to 65 nm thick, even with Al mole fractions up to $x = 0.38$ [119, 120].

For a pseudomorphic epitaxial layer of a nitride material the components of the strain tensor in the layer plane are given by

$$\epsilon_\perp = \epsilon_{xx} = \epsilon_{yy} = \frac{a - a_0}{a_0} \quad , \quad \epsilon_\parallel = \epsilon_{zz} = \frac{c - c_0}{c_0} = -\frac{C_{13}}{C_{33}}(\epsilon_{xx} + \epsilon_{yy}) \qquad (6.1)$$

where x and y refer to two in-plane directions and z to the [0001] direction. a and a_0 are respectively the epilayer and substrate in-plane lattice constants and c and c_0 are the corresponding values for the c-axis. C_{13} and C_{33} are the appropriate elastic constants. The strain in the epitaxial layer perpendicular to the substrate can also be written in terms of Poisson's ratio (σ) as

$$\epsilon_\perp = -\frac{2\sigma}{1 - \sigma}\epsilon_\parallel \qquad (6.2)$$

For the nitride semiconductors σ is approximately $1/3$, and thus $\epsilon_\parallel \sim \epsilon_\perp$.

Strain can also shift the energies of the conduction and valence bands and hence change the energy gap. In the nitride materials the calculations of Bernardini et al. [121] and Nardelli et al. [122] show the hydrostatic strain component leads to an increase of the band gap with compressive strain (figure 6.2b). This change in band gap occurs together with changes in the band curvature. However, the resultant changes in carrier
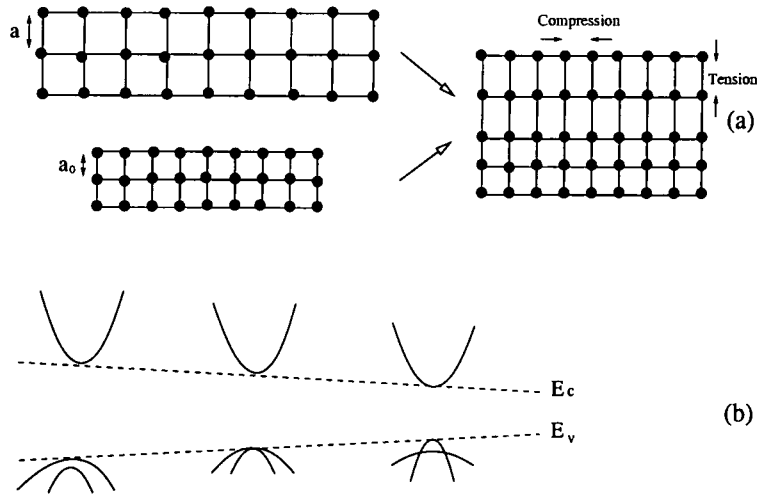
Figure 6.2: Schematic diagram showing exaggerated lattice mismatch between substrate and epilayer, resulting in strained growth. (a) Biaxial strain occurring due to assemblage of crystals with different lattice constants. (b) The behaviour of a direct gap semiconductor with compressive strain on the left and tensile strain on the right.

effective mass are relatively small and are not included in the device simulations [123]. For transport, the primary strain effect is on the valence band in the lifting of the degeneracy, which reduces scattering and hence improves the hole transport properties. Strained HFETs with p-type channels are believed to show improvements due to these band structure improvements but here we are concerned with electron devices only.

6.3.2 Piezoelectric and polarization effects

If piezoelectric and other polarization effects were ignored the conduction band profile of a typical nitride heterostructure in an HFET would be as shown in figure 6.3. Due to the ionized donors in the AlGaN layer and electrons in the GaN, a space-charge region is established that leads to band bending. However, in addition to the conduction band discontinuity across the interface and band bending due to doping and free carrier effects, heterostructures exhibit polarization charge effects. The lattice mismatch between GaN and the ternary alloy AlGaN in HFET structures produces a strain-induced piezoelectric polarization which may lead to an enhanced electron accumulation in the
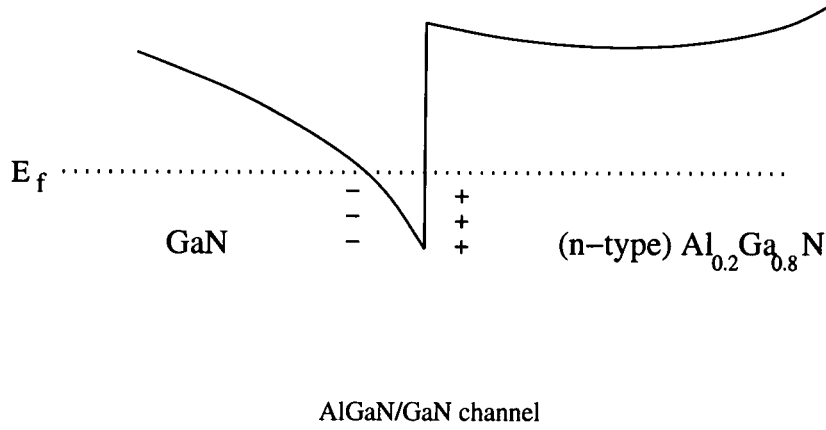
AlGaN/GaN channel

Figure 6.3: Schematic diagram showing the bending of the conduction bands at a AlGaN/GaN heterojunction.

channel region. In addition, nitride heretostructures can have a nonzero macroscopic polarization even in the absence of strain (spontaneous polarization) because of low symmetry in the crystal structure. These effects can have a significant influence on the output characteristics of nitride HFETs.

In the linear regime, the total macroscopic polarization P of nitride layers is the sum of the spontaneous polarization P_{sp} in the equilibrium lattice, and the strain-induced or piezoelectric polarization P_{pe}. The increasing nonideality of the crystal structure in going from GaN to AlN corresponds to an increase in spontaneous polarization. The spontaneous polarization for GaN and AlN along the c-axis of the wurtzite structure is negative and increases in magnitude in going from GaN to AlN [124] according to the rule

$$P_{sp}(x) = -(0.05x + 0.029) \qquad \text{C/m}^2 \qquad (6.3)$$

where x is the Al mole fraction in the $Al_x Ga_{1-x}N$ alloy. The piezoelectric polarization of the alloy is related to the strain ϵ_j and piezoelectric coefficients as

$$P_{pe} = \sum_i e_{ij}\epsilon_j = e_{31}(\epsilon_{xx} + \epsilon_{yy}) + e_{33}\epsilon_{zz} \qquad (6.4)$$

where e_{33} and e_{31} are the piezoelectric coefficients and ϵ_z is the strain along the c-axis. The relation between the lattice constants in the hexagonal AlGaN system is given by

$$\frac{c - c_0}{c_0} = -2\frac{a - a_0}{a_0}\frac{C_{13}}{C_{33}} \qquad (6.5)$$

where C_{13} and C_{33} are elastic constants. Thus the piezoelectric polarization in the direction of the c-axis is

$$P_{pe} = 2\frac{a - a_0}{a_0}\left[e_{31} - e_{33}\frac{C_{13}}{C_{33}}\right] \tag{6.6}$$

In general a spatial variation of the total polarization $(P_{sp} + P_{pe})\hat{z}$ results in a charge distribution $-\nabla.(P_{sp}+P_{pe})\hat{z}$ and an associated electric field given by Poisson's equation

$$\nabla.(\epsilon_0\epsilon_s\mathbf{E}) = -\nabla.(P_{sp} + P_{pe})\hat{z} \tag{6.7}$$

where ϵ_s is the relative permittivity of the material and $\hat{z}$ is a unit vector parallel to the c-axis. In particular the abrupt changes of the polarization field at the AlGaN/GaN interface result in an induced charge per unit area σ_{pz} given by $-(P_{sp} + P_{pe})$ and a z-directed electric field across the AlGaN layer given by [125]

$$E_z = -(P_{sp} + P_{pe})/\epsilon_s\epsilon_0 \tag{6.8}$$

In the HFET of figure 6.1 which is considered here a sheet of positive charge of area density σ_{pz} is present at the AlGaN/GaN interface, and there is a corresponding negative sheet charge $-\sigma_{pz}$ at the top of the AlGaN layer. Note, the piezoelectric charge is another variable that may be used in the design of AlGaN/GaN HFETs. In particular, the sign of the charge obtained is dependent on the orientation of the crystal. AlGaN epitaxial layers grown with Ga-terminated faces (0001 orientation) contain polarization dipoles opposite in orientation to those grown with N-terminated faces (000$\bar{1}$ orientation).

6.4 Monte Carlo model of a AlGaN/GaN HFET

The device shown in figure 6.1 has been modelled using a version of SLURPS that has been modified to include piezoelectric effects in strained layers. In order to represent the polarization across the $Al_{0.2}Ga_{0.8}N$ layer, fixed superparticles are placed in the upper and lower electric field cells of that layer as shown in figure 6.4. In the simulations presented here it is assumed that the magnitude of the spontaneous and strain-induced polarization charge has a density of 2×10^{17} em^{-2} at the top and bottom of the AlGaN

layer [119, 126], with the positive charge at the AlGaN/GaN interface [127]. Figure 6.4b shows the polarization charges at the top and bottom of the layer and the doping centres confined in the AlGaN barrier layer. Also shown in figure 6.4c are the trap centres, which are fixed at the centre of each electric field cell, and some captured mobile carriers.
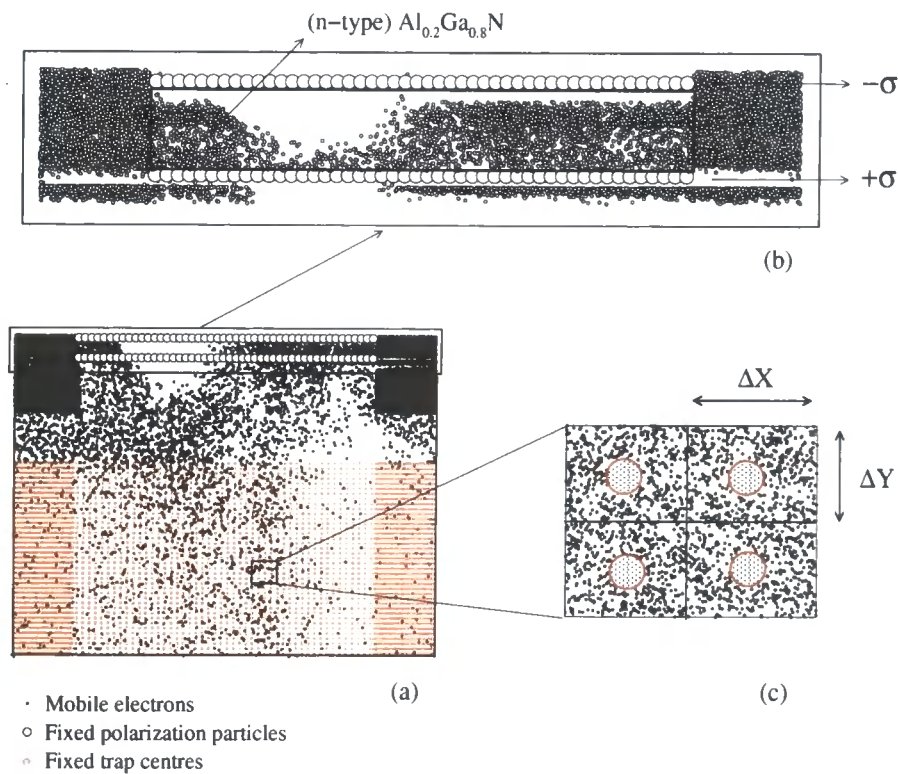
Figure 6.4: (a) Particles in the Monte Carlo simulation of $Al_{0.2}Ga_{0.8}N$/GaN HFET are of two types. There are fixed particles which represent the polarization charges and trap centres. Electrons can be captured by trap centres or attracted by the $+\sigma$ polarization sheet. There are also mobile superparticles which represent unbound electrons which can flow through the device, (b) polarization charges and AlGaN barrier layer and (c) trap centres which are fixed at the centre of electric field cells and occupied by some mobile superparticles.

6.5   Simulated results and discussion

To study the effect of the strain induced polarization on device performance, we have simulated the GaN HFET shown in figure 6.1 with and without the inclusion of the polarization effect. We have also examined the effect of using a doped or low-doped channel on the electron transport properties. The effects of trap centres distributed in the GaN buffer layer have also been included. There is growing evidence suggesting that trapping effects are also present on the AlGaN surface which may be related to current collapse [128]. Therefore, to model this effect we have also performed simulations assuming trap centres in the surface layer only. In the absence of any firm information on trap centre parameters or their distribution throughout the buffer and surface layers, we have assumed trap centres have an energy ΔE_{trap} of 0.3 eV with a capture cross-section of 2×10^{-19} m^2 and a density of 10^{23} m^{-3}, which are the same parameters as used for the MESFET in chapter 5.

The simulation results indicate that the steady-state drift velocity and electronic transport properties of the device increase with the inclusion of the polarization effect across the interface, which is in accord with the recent theoretical work of Ando *et al.* [127], who used two-dimensional self-consistent full-band Monte Carlo simulation for an Al$_{0.2}$Ga$_{0.8}$N/GaN HFET including the piezoelectric polarization effect.

Figure 6.5 shows the *I-V* curves for the polarization and the polarization-free devices. The polarization field in the heterostructure leads to an enhancement of the drain saturation current from 1250 mA mm^{-1} to 1650 mA mm^{-1} at zero gate bias. A comparison with the GaN MESFET of similar dimensions considered in the previous chapter shows that the GaN HFET with and without polarization effects has significantly higher output drain current at the same drain and gate biases. For example, the simulated drain current at zero gate bias and drain bias of 80 V for the GaN MESFET is 600 mA mm^{-1} whereas for the GaN HFET, with and without polarization effects, it is increased to 1250 and 1650 mA mm^{-1} respectively. This pattern of output current enhancement is due to the use of a heterostructure and the fact that the polarization charge encourages a higher electron density at the AlGaN/GaN heterointerface where trapping does not occur and the electron mobility is high. The associated intrinsic

transconductances derived from the current-voltage characteristics at the knee voltage ($\sim$ 18 V) for the simulated devices without and with polarization charge are 85 and 110 mS mm^{-1} respectively.

Figure 6.6 compares the electron density recorded from the buffer to the gate for

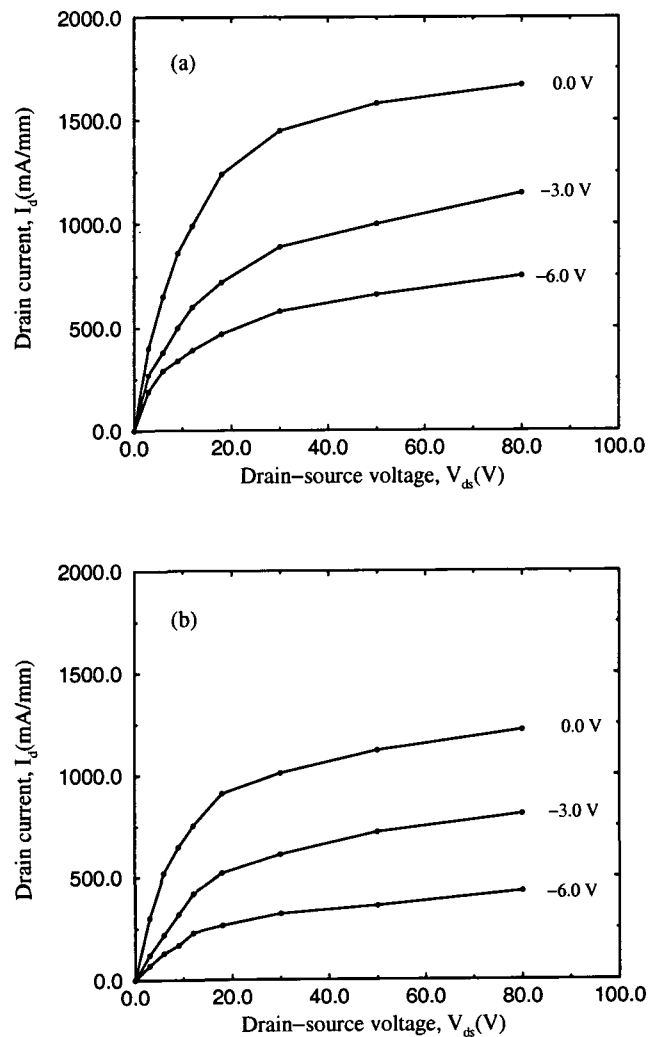**Figure 6.5:** Simulated current-voltage characteristic for the Al$_{0.2}$Ga$_{0.8}$N/GaN HFET at room temperature, (a) With polarization effect ($\sigma = 2 \times 10^{17}$ cm^{-2}) and (b) Without polarization effect.

both polarization and polarization-free devices. It can be seen that for the same bias condition of V_{ds} = 30 V and V_{gs} = -1 V (which we use for a number of subsequent

figures) the electron density in the interface region is substentially increased for device with polarization charge. The speed of the device is related to the cut-off frequency f_T which, in the simplest model, can be determined from the transconductance g_m and the total gate to source capacitance C_{gs} and drain to gate capacitance C_{dg} using the expression [129]

$$f_T = \frac{g_m}{2\pi(C_{gs} + C_{dg})} \tag{6.9}$$

The transconductance can be easily obtained from the transfer characteristic curve as explained previously. The total gate to source and drain to gate capacitances can be obtained directly from the Monte Carlo simulation since the charge throughout the device is available at each timestep. However, this calculation will underestimate the capacitance of the real device because it does not take into account the parasitic capacitances. An alternative method for obtaining f_T, which can be adopted is to calculate the average electron transit time along the channel and hence obtain the intrinsic cut-off frequency by relation [86]

$$f_T = \frac{1}{2\pi\tau} \tag{6.10}$$

By summing the transit times for each field cell we estimate the mean transit time to be $\tau = 2.6$ ps which suggests an intrinsic cut-off frequency of about 60 GHz.

Figures 6.7a and 6.7b show a contour plot of the conduction band edge for the two devices. It is noticeable that much of the drain-source bias in the polarization-free device is dropped in the vicinity of the gate region. The sharp drop in potential at the drain edge of the gate generates hot electrons which can diffuse into the AlGaN layer and also into the GaN buffer layer where they can be trapped. In comparison, figure 6.7b shows that the presence of polarization charge reduces the sharp potential drop seen in figure 6.7a as a result of the high electron density around the heterointerface, and also strongly affects the potential between source and gate. This improves electron confinement, which is one of the reasons for the higher drain current.

To study the effect of the magnitude of the polarization charge density on electronic transport in more detail, Monte Carlo simulations of the steady-state condition were performed for a range of different densities. Figures 6.8a and 6.8b compare semi-quantitatively the electron distribution around the heterointerface for two different
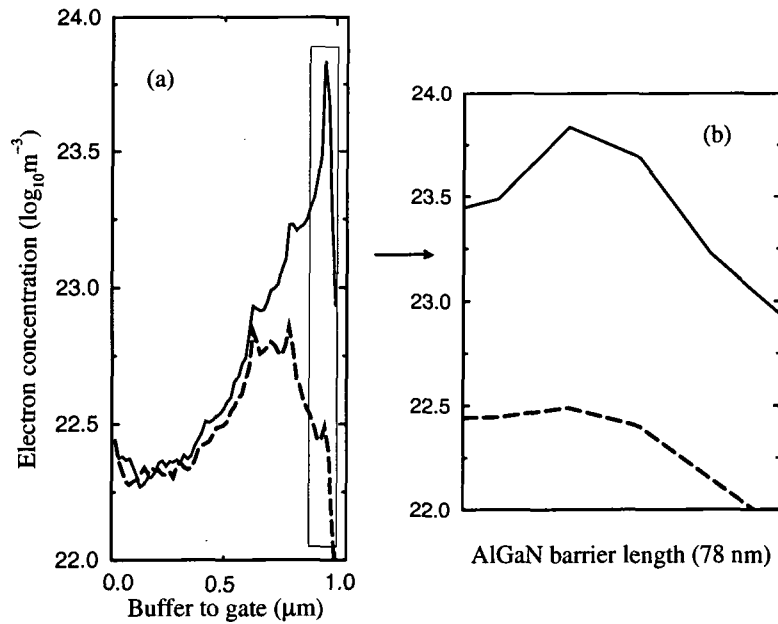
(a)

Electron concentration ($\log_{10}$m^{-3})

24.0

23.5

23.0

22.5

22.0

0.0   0.5   1.0
Buffer to gate (µm)

24.0

23.5

23.0

22.5

22.0

(b)

AlGaN barrier length (78 nm)

Figure 6.6: (a) Electron density through the device under the gate extracted along the vertical line from the buffer to the centre of the gate. The solid line shows the results for the polarized device ($\sigma = 2 \times 10^{17}$ em^{-2}) and the dashed line corresponds to the polarization-free device ($V_{ds} = 30$ V and $V_{gs} = -1$ V), (b) Comparison of electron density through the AlGaN for polarized and polarization-free devices.

charge densities. With increasing polarization charge density the number of electrons occupying the channel region increases. Figure 6.8c shows that the electron drift velocity increases from 1.9×10^5 to 2.7×10^5 ms^{-1} as σ goes from 10^{16} to 2×10^{17} em^{-2}. The calculated kinetic energy averaged over the whole device thickness and its associated values along the buffer to gate region are also shown in figures 6.9a and 6.9b, respectively. Figure 6.9a shows that the maximum of the kinetic energy occurs in the vicinity of the gate, reaching about 4 eV. The kinetic energy in the vicinity of the drain is significantly lower at 3 eV as the electrons lose energy by scattering. Figure 6.9b shows the effect of polarization charges on the electron kinetic energy. It can be seen that in the device with higher polarization, the electron kinetic energy increases abruptly across the interface layer and then goes through a large reduction after the
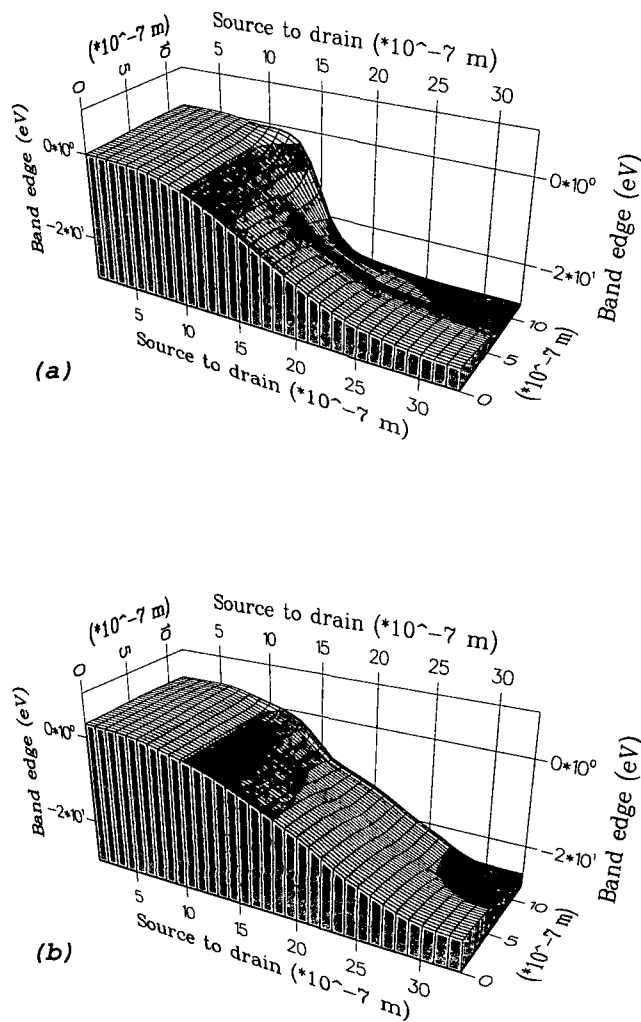
Figure 6.7: Three-dimensional distribution of the conduction band profile in the simulated GaN HFET at room temperature for $V_{ds} = 30$ V and $V_{gs} = -1$ V. (a) Without polarization charge at the interface layer and (b) With polarization charge density of 2×10^{17} em^{-2}.
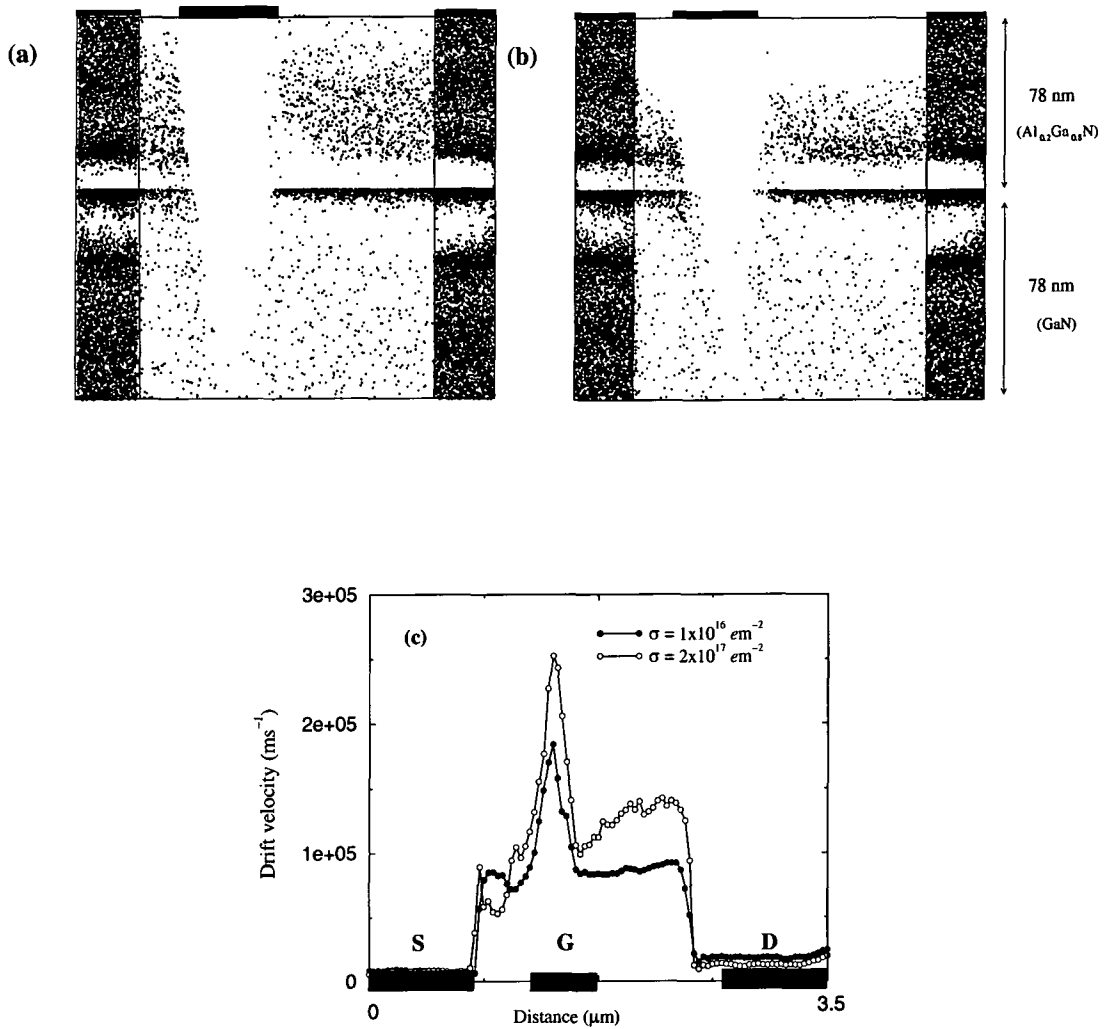
Figure 6.8: Effect of different polarization sheet charge densities on electron distribution and drift velocity through the wurtzite GaN HFET at room temperature when $V_{gs} = -1$ V, $V_{ds} = 30$ V. (a) $\sigma = 10^{16}$ em^{-2}, (b) $\sigma = 2 \times 10^{17}$ em^{-2} and (c) the associated electron drift velocity through the whole device.

polarization layer. This behaviour can be explained by the superior confinement to the channel of hot electrons which exists in the device. Figure 6.10a give an illustration
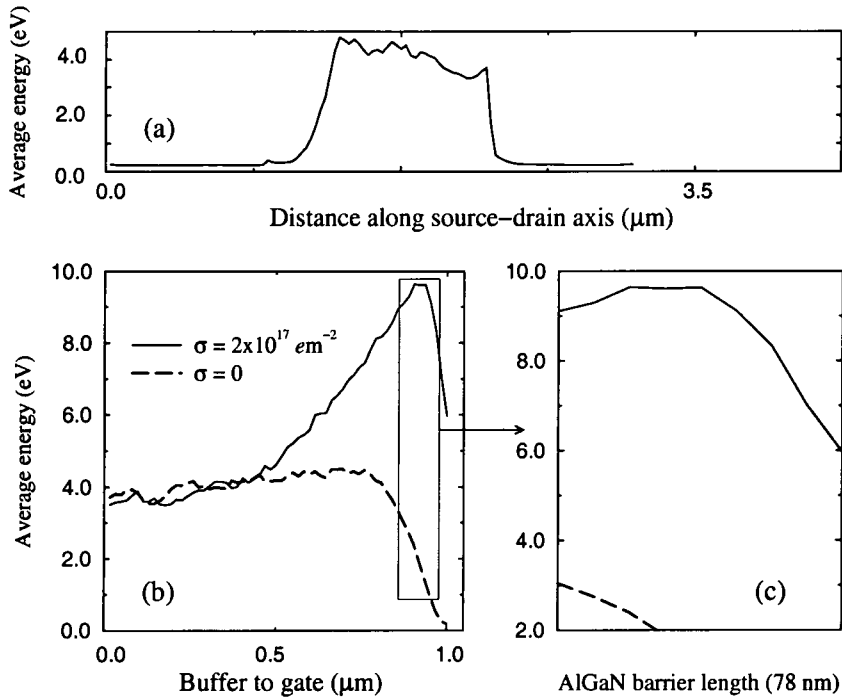

Figure 6.9: (a) Average kinetic energy through the whole device, (b) Average kinetic energy from buffer to gate for polarization and polarization-free devices (V_{ds} = 30 V and V_{gs} = −1 V) and (c) Comparison of kinetic energy through the AlGaN for polarization and polarization-free devices.

of the spatial and valley distribution of the electrons in the device with polarization charge. It is apparent that a high percentage of electrons flow from the source to the drain through the substrate at a drain bias of 30 V. This transport between source and drain is not well controlled by the gate, a problem which is exacerbated when the source and drain are moved closer together. Substrate leakage also causes a negative shift in the threshold voltage. The leakage can be suppressed by placing a complementary-doped buffer layer or a suitable junction between the active layer and the substrate. This figure also shows a marked enhancement of high electron density near the AlGaN interface due to electron attraction by positive charge there. Also, it is clear that in the high electric field region between gate and drain, the electrons are heated and excited

to the upper valleys. The calculations show that about 8% of electrons populate the upper U, K, M and Γ_3 valleys when the drain bias is 30 V.

The longitudinal velocity distributions of electrons in different valleys averaged over the whole device thickness is shown in figure 6.10b. As expected the electron velocity is largest between gate and drain and there is substantial intervalley transfer. As the drain bias is increased, the high-field region between the gate and the drain extends and an increasing number of electrons obtain sufficient kinetic energy to be scattered into one of the satellite valleys of the conduction band. It can be observed from figure 6.10b that electrons reach velocities as high as 3×10^5 ms^{-1}, which is higher than the saturated velocity typically assumed for bulk GaN.

electrons in Γ valley
● electrons in K valley
○ electrons in U valley

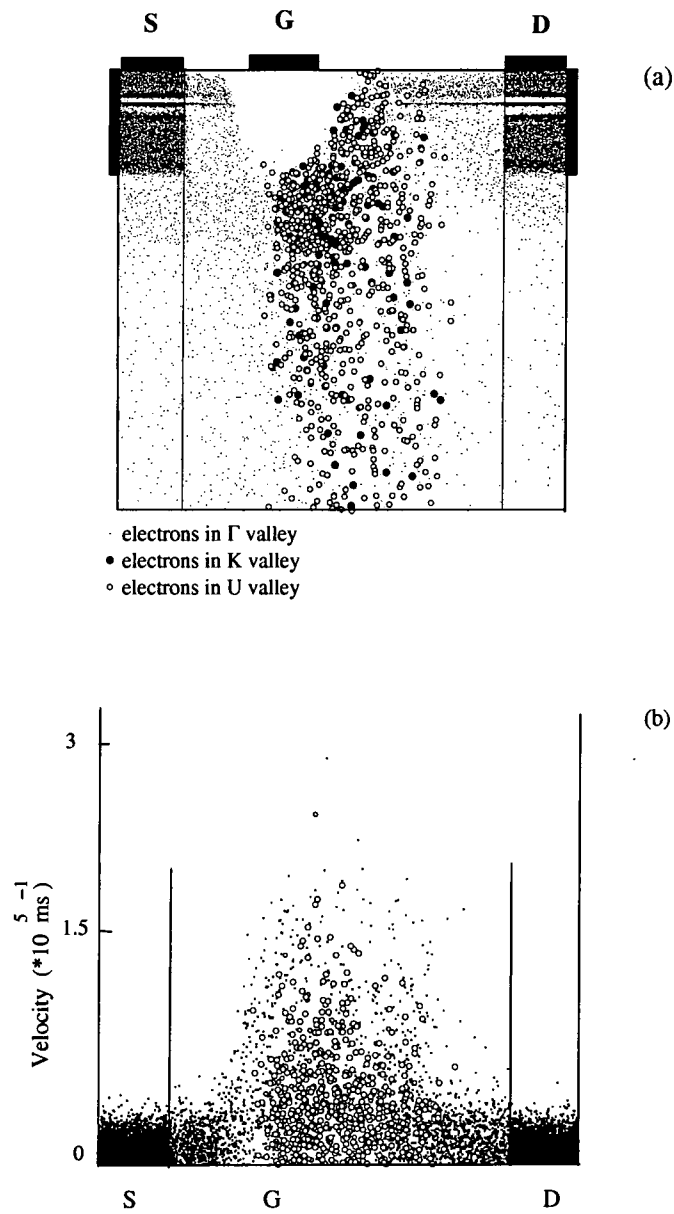**Figure 6.10:** Position of electrons in the simulated $Al_{0.2}Ga_{0.8}N/GaN$ HFET at room temperature. (a) Electron position distribution through the simulated device for $V_{gs} = -1$ V, $V_{ds} = 30$ V in the central Γ, U and K valleys and (b) Longitudinal velocity distribution of electrons in the Γ and other upper valleys.

The influence of surface trap centres on the electron characteristics has also been investigated. Surface trap centres are found to exert little influence on the electron transport in a GaN HFET compared to the traps distributed throughout the buffer layer. Figure 6.11 compares a static I-V characteristic for devices with traps in the buffer layer and at the upper surface of the AlGaN layer with a density of 10^{23} m^{-3}. It is apparent that the traps in the buffer layer have a much higher effect on current suppression.

To examine the possible effect of doping on the characteristics of GaN HFETs, we have also performed Monte Carlo simulations for low-doped channel and AlGaN barrier layers (10^{21} m^{-3}). Figures 6.12a and 6.12b compare the simulated electron density and drain currents obtained for doped and low-doped GaN HFETs. It can be seen that due to polarization charge there is still a substantial electron density in the channel even with low-doping. However, the lower electron density seen in the channel in figure 6.12a does result in a lower drain current as illustrated in figure 6.12b.
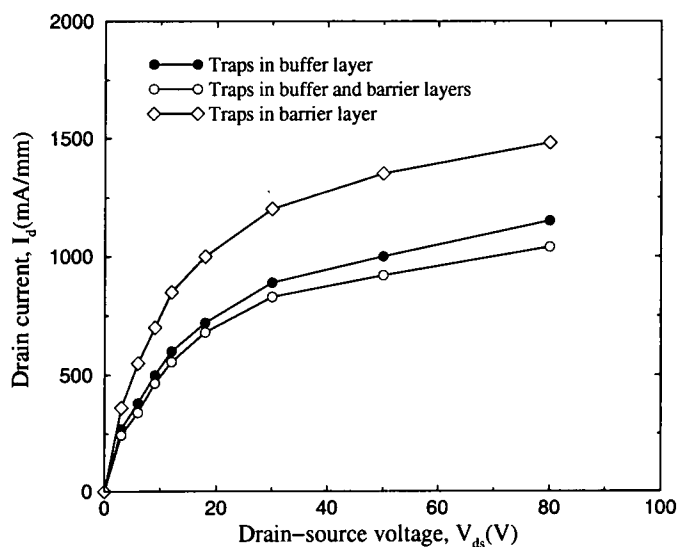
Figure 6.11: A comparison of I-V characteristics for a simulated GaN HFET with surface trap centres and buffer trap centres at room temperature.
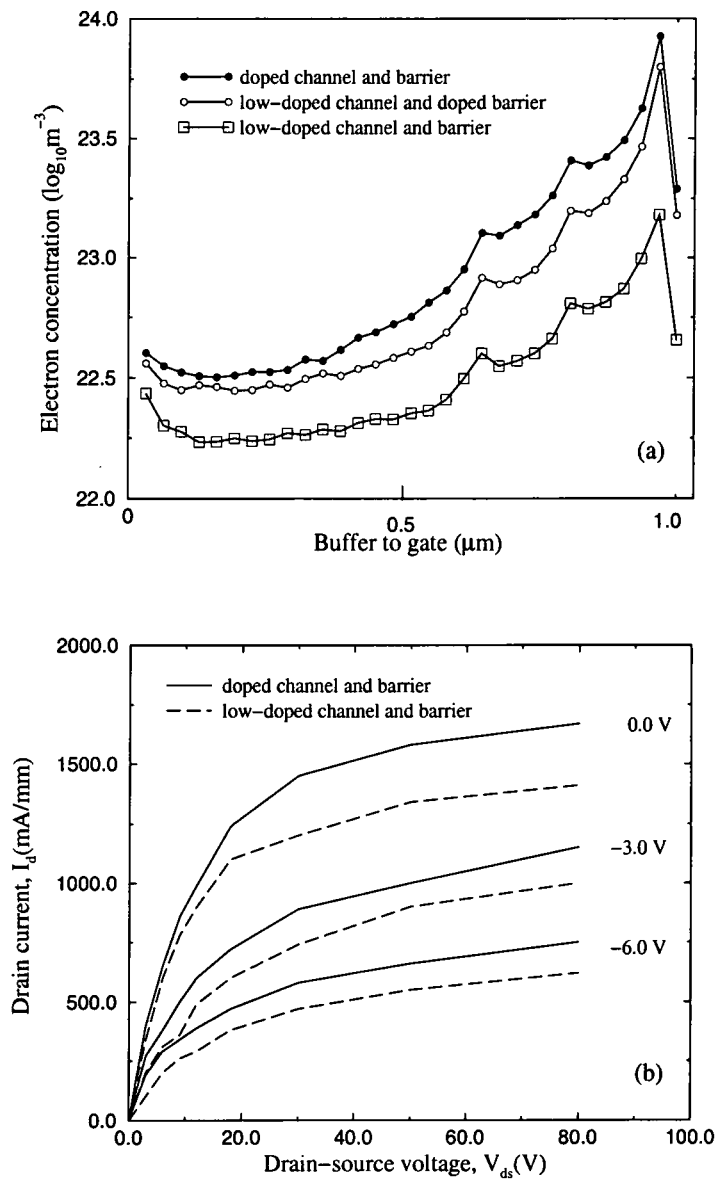
Figure 6.12: (a) Electron density profile from buffer to gate for doped $(5 \times 10^{23}~\mathrm{m}^{-3})$ and low-doped $(10^{21}~\mathrm{m}^{-3})$ channel and AlGaN barrier layers at room temperature when $V_{gs} = -1$ V, $V_{ds} = 30$ V, (b) the relative I-V characteristics for doped and low-doped devices.

6.6 Conclusions

In this chapter, we have used an ensemble Monte Carlo model to investigate the properties of an $Al_{0.2}Ga_{0.8}N$/GaN-based HFET. Due to the existence of strain in the alloy layer, which is piezoelectric, there is a positive polarization charge density at the interface between GaN and AlGaN layers and a negative charge density at the device surface. We have developed a simple model to include the polarization effects in SLURPS and carried out simulations of the device. For the results presented, it has been assumed that polarization charge at the interface layer is $2 \times 10^{17}\ em^{-2}$. The simulation results show that the influence of polarization charge is important because it can significantly enhance the drain saturation current. The polarization effect in the simulated GaN heterostructure was shown not only to increase the output drain current, but also the average electron velocity as a result of concentrating the transport closer to the GaN-AlGaN interface and away from the buffer layer. As a result an improvement in the transconductance is also predicted.

Chapter 7

Summary and Further Work

7.1 Summary

The main aim of the work presented in this thesis has been to use Monte Carlo simulation to understand the electronic transport properties of bulk GaN with high applied electric field and GaN-based field effect transistors operating with high drain-source voltages.

The Durham ensemble Monte Carlo simulation software SLURPS has been modified so that it can be used to model electron transport in semiconductors with the wurtzite crystal structure. The bulk electronic transport calculations carried out with the modified simulation software and described in chapter 3 were intended to test the simulation model and to provide information on the electron drift velocity as a function of electric field, which is a fundamental consideration in electron device design. In particular it was shown how the five-valley model used could be applied to the high-field transport calculations and give theoretical results comparable to those obtained by other workers. We found that for a given electric field, steady-state drift velocity and velocity overshoot are always weaker in the wurtzite crystal structure than in the zincblende structure, which was attributed to the larger Γ valley effective mass in the wurtzite structure. The calculations also suggested that GaN had potential for high-temperature and high-power device applications. The dependence of electron mobility on doping and temperature in the low electric field regime has also been calculated

using an iterative solution of the Boltzmann equation. The results showed that the low-field mobility is significantly higher for the zincblende structure due to the lower effective mass in the central valley.

Chapter 4 reported studies of the transport properties of electrons in wurtzite GaN n^+-i(n)-n^+ diodes with a 0.4 or 0.6 μm active layer length. The anode voltage ranged from 10 to 50 V corresponding to fields close to and beyond the threshold for inter-valley tansfer. The distributions of electron energies and electron velocities, and the profiles of the electron density, electric field and potential were computed. The near ballistic nature of the electron transport in the diode and the role of the upper valleys in electron transport were discussed. The results suggested that the electron velocity averaged over the length of the device increases with decreasing the length of the active layer, largely because of the quasi-ballistic transport occurs in a larger fraction of the device. The effect of raising the lattice temperature to 600 K was found to be a reduction of the maximum average velocities, but these were still above about 2×10^5 ms^{-1}.

In chapter 5 we described the use of the five-valley model of GaN in the simulation of GaN MESFETs. The calculated drain currents were found to be consistently larger than the experimental data for similar devices. Better quantitative agreement with experiment was obtained by introducing electron traps into the transport model. A Monte Carlo-based model to simulate the capture and emission probabilities of electrons in the device was described in chapter five. It was assumed that a single type of trap with specific parameters was distributed throughout the device or just in the buffer layer and we compared the electrical properties of GaN MESFETs with and without trapping centres. Significant differences in the output characteristics were found as a result of electron capture and emission during transport from source to drain, which can increase the effective transit time. In addition the trapped electrons cause space charge which further acts to reduce the drain current. The simulation showed that as the temperature was increased, electrical performance improved due to electron emission from the trap centres. We also investigated how the different trap centre parameters like capture cross-section, trap density and trap energy affect the

steady-state characteristics. Since the filled traps can be emptied by both thermal excitation and photoionization, the model was also modified to consider optical emission. The simulations were carried out as a function of incident wavelength with a fixed incident light intensity. It was shown that the photoionization of trapped electrons in the buffer layer and the subsequent return of these electrons to the conduction band could compensate the drain current collapse as seen in experiment. Calculations of the effect of modulating the gate bias have also been carried out to test the device response and the frequency bandwidth. The maximum cutoff frequency and transconductance of a 0.3 μm gate GaN MESFET including trapping effects were found to be 25 GHz and 75 mS mm^{-1}, respectively.

A simulation model for electron transport in AlGaN/GaN heterojunction FETs was presented in chapter 6. In such devices the alloy layer is strained and the piezoelectric nature of the material results in polarization charge effects. The model was applied to $Al_{0.2}Ga_{0.8}N$/GaN HFET structures with a 78 nm $Al_{0.2}Ga_{0.8}N$ pseudomorphically strained layer where the spontaneous and piezoelectric polarization effects were taken into account. In order to represent the polarization of the $Al_{0.2}Ga_{0.8}N$ layer, fixed superparticles are placed in the upper and lower electric field cells of the layer with a charge density 2×10^{17} em^{-2}. The simulation results showed that the piezoelectric induced polarization charge can produce a significant enhancement of the drain saturation current. The polarization effect was shown to not only increase the current density, but also the average electron velocity as a result of concentrating the transport closer to the GaN-AlGaN interface and away from the buffer layer.

7.2 Further work

The calculations in this thesis were performed in the non-parabolic multivalley approximation and for the most part concentrated on the high electric field regime. Despite the large bandgap of GaN and its alloy with AlN electrons can reach energies at which impact ionization can be expected to occur but that process was not included in the simulations. A possible extension of this work would be to use a full-band Monte Carlo model which includes impact ionization. The inclusion of impact ionization would provide a significant enhancement in the capabilities of the simulation, particularly as there is much interest in the high power applications of GaN transistors. The use of a full-band model of electron transport would itself provide a more reliable picture of high field electron transport with or without impact ionization. However, it must be recognized that the computational effort required for such a numerical model is very great, both in terms of the development of the calculation and running of the software. It would also be necessary to have an accurate description of the band structure of the group-III nitride compounds and alloys over a large energy range.

The current model could be used with little extra development work to study the role of extended scattering defects and the electron-electron scattering mechanisim in device simulation. The results obtained from these simulations might be expected to show some improvement in agreement with experimental observations especially since the quality of many GaN samples is such that defects have a significant effect on the measured transport properties.

Bibliography

[1] W. Shockley, Proc. IRE. **40**, 1365 (1952)

[2] R. J. Molnar, W. Gotz, L. T. Romano and N. M. Johnson, J. Cryst. Growth. **178**, 147 (1997).

[3] S. Nakamura, M. Senoh, S. Nagahama and N. Iwasa, Appl. Phys. Lett. **72**, 2014 (1998)

[4] S. Logothetidis, J. Petalas, M. Cardona and T. Moustakas, Mater. Sci. Eng. **29**, 65 (1995)

[5] M. E. Lin, B. N. Sverdlov and H. Morkov, J. Appl. Phys. **74**, 5038 (1993)

[6] D. G. Ebling, M. Rattunde, L. Steinke and K. W. Benz, J. Cryst. Growth. **201/202**, 411 (1999)

[7] J. I. Pankove, E. A. Miller and J. E. Berkeyheiser, RCA Rev. **32**, 383 (1971)

[8] H. Amano, M. Kito, K. Hiramatsu and I. Akasaki, J. Appl. Phys. **28**, L2112 (1989)

[9] M. Farahmand and K. F. Brennan, IEEE Trans. Elec. Devices. **46**, 1319 (1999)

[10] M. W. Shin and R. J. Trew, Electronics Letters. **31**, 498 (1995)

[11] W. Kruppa, S. C. Binari and K. Doverspike, Electronics Letters. **31**, 1951 (1995)

[12] S. L. Rumyantsev, N. Pala and M. S. Shur, J. Appl. Phys. **88**, 6726 (2000)

[13] A. Ozgur, W. Kim, A. Botchkarev and H. Morkoc, Electronics Letters. **31**, 1389 (1995)

[14] M. A. Khan, J. N. Kuznia and D. T. Olsen, Appl. Phys. Lett. **62**, 1786 (1993)

[15] M. A. Littlejohn, J. R. Houser and T. H. Gilsson, Appl. Phys. Lett. **26**, 625 (1975)

[16] B. Gelmont, K. Kim and M. Shur, J. Appl. Phys. **74**, 1818 (1993)

[17] V. W. Chin, T. L. Tansley and T. Osotchan, J. Appl. Phys. **75**, 7365 (1994)

[18] D. L. Rode and D. K. Gaskill, Appl. Phys. Lett. **66**, 1972 (1995)

[19] U. V. Bhapkar and M. Shur, J. Appl. Phys. **82**, 1649 (1997)

[20] J. Neugebaur and C. G. Van de Walle, Phys. Rev. **B50**, 8067 (1994)

[21] D. J. Chadi, Appl. Phys. Lett. **71**, 2970 (1997)

[22] T. Kurosawa, J. Phys. Soc. Jpn. **21**, 424 (1966)

[23] R. K. Willardson and E. R. Weber, *Semiconductors and Semimetal*, Volume 50, Academic Press (1998)

[24] W. L. Lambrecht, B. Segall, *Band structure of the group-III nitrides*, Academic Press (1998)

[25] R. Wang, P. P. Ruden, J. Kolnik and K. F. Brennan, J. Phys. Chem. Solids. **58**, 913 (1997)

[26] S. Bloom, J. Phys. Chem. Solids. **32**, 2027 (1971)

[27] S. K. Pugh, D. J. Dugdale, S. Brand and R. A. Abram, Semicond. Sci. Technol. **14**, 23 (1999)

[28] S. Strite and H. Morkoc, J. Vac. Sci. Technol, **B10**, 1237 (1992)

[29] B. E. Foutz, L. F. Eastman, U. V. Bhapkar and M. S. Shur, Appl. Phys. Lett. **70**, 2849 (1997)

[30] M. Shur, B. Gelmont, C. Saavedra-Munoz and G. Kelner, Inst. Phys. Conf. Ser, **137**, 465 (1993)

[31] Udayan. V. Bhapkar and M. S. Shur, J. Appl. Phys. **82**, 1649 (1997)

[32] J. Kolnic, I. H. Oguzman and K. F. Brennan, J. Appl. Phys. **78**, 1033 (1995)

[33] J. D. Albrecht, R. P. Wang and P. P. Ruden, J. Appl. Phys. **83**, 4777 (1998)

[34] Y. C. Yeo, T. C. Chong and M. F. Li, J. Appl. Phys. **83**, 1429 (1998)

[35] C. Bulutay, B. K. Ridley and N. A.Zakhleniuk, Phys. Rev. **B62**, 15754 (2000)

[36] W. Fawcett, A. D. Boarrdman and S. Swain, J. Phys. Chem. Solids. **31**, 1963 (1970)

[37] E. O. Kane, J. Phys. Chem. Solids. **1**, 249 (1957)

[38] S. J. Pearton, J. C. Zolper, R. J. Shul and F. Ren, J. Appl. Phys. **86**, 1 (1999)

[39] V. W. Chin, T. L. Tansley and T. Osotchan, J. Appl. Phys. **75**, 7365 (1994)

[40] C. Jacoboni, P. Lugli, *Monte Carlo Method for Semiconductor and Device Simulation*, Springer-Verlag (1989)

[41] C. Moglestue, *Monte Carlo Simulation of Semiconductor Devices*, Chapman and Hall (1993)

[42] B. K. Ridley, *Electrons and phonons in semiconductor multilayers*, Cambridge University Press (1997)

[43] M. S. Lundstrom and R. K. Ahrenkiel, *Semiconductors and Semimetal*, Volume 39, Academic Press (1993)

[44] H. Morkoc, *Nitride semiconductor and devices*, Springer-velag (1999)

[45] D. Chattopadhyay and H. J.Queisser, Review of Modern Physics, **53**, part1 (1981)

[46] J. W. Harrison and J. R. Hauser, Phys. Rev. B13, 5347 (1976)

[47] R. K. Willardson and A. C. Beer, *Semiconductors and Semimetal*, Volume 10, Academic Press (1975)

[48] T. P. Pearsall, *GaInAs Alloy Semiconductors*, John Wiley (1982)

[49] D. L. Rode, Phys. Rev. B2, 1012 (1970)

[50] D. L. Rode, Phys. Rev. B3, 3287 (1971)

[51] D. L. Rode and A. C. Beer, Phys. Rev. B3, 2534 (1971)

[52] A. D. Boardman, *Physics Programs*, John Wiley (1980)

[53] J. M. Hammersley and D. C. Handscomb, *Monte Carlo Methods*, Meethuen (1969)

[54] W. Fawcett, A. D. Boarrdman and S. Swain, J. Phys. Chem. Solids. 31, 1963 (1970)

[55] S. Dhar and S. Ghosh, J. Appl. Phys. 86, 2668 (1999)

[56] W. J. Fan, M. F. Li and T. C. Chong, J. Appl. Phys. 79, 188 (1996)

[57] J. Kolník, Y. Wang, I. H. Oğuzman and K. F. Brennan, J. Appl. Phys. 76, 3542 (1994)

[58] I. H. Oğuzman, Y. Wang, J. Kolník and K. F. Brennan, J. Appl. Phys. 77, 225 (1995)

[59] I. H. Oğuzman, E. Bellotti, K. F. Brennan, J. Kolník, R. Wang and P. P. Ruden, J. Appl. Phys. 81, 7827 (1997)

[60] J. D. Albrecht, R. P. Wang and P. P. Ruden, J. Appl. Phys. 83, 1446 (1998)

[61] J. G. Ruch and W. Fawcett, J. Appl. Phys. 41, 3843 (1970)

[62] N. S. Mansour, K. W. Kim and M. A. Littlejohn, J. Appl. Phys. 77, 2834 (1995)

[63] B. E. Foutz, S. K. O'Leary and M. S. Shur, J. Appl. Phys. **85**, 7727 (1999)

[64] M. Suzuki and T. Uenoyama, Phys. Rev, **B52**. 8132 (1995)

[65] E. Bellotti, B. K. Doshi and K. F. Brennan, J. Appl. Phys. **85**, 916 (1999)

[66] S. K. O'Leary, B. E. Foutz and M. S. Shur, J. Appl. Phys. **83**, 826 (1998)

[67] K. Tomizawa, Y. Awano and N. Hashizume, IEE. PROC. **129**, 131 (1982)

[68] Bernard. Gil, *Group-III Nitride Semiconductor Compounds*, Oxford Science Pub. (1998)

[69] M. Asif Khan and M. S. Shur, Materials Science and Engineering. **B46**, 69 (1997)

[70] S. C. Binari and D. Doverspike, Solid-state Electronics. **41**, 177 (1997)

[71] M. Walmsley and R. A. Abram, Proc. IEEE/Cornell Conference on Advanced Concepts in High Speed Semiconductor Devices and Circuits, Ithaca, USA, (1995) (IEEE, NEW York, 1995)

[72] D. Hoare and R. A. Abram, Int. J. Electronics. **83**, 429 (1997)

[73] S. Trassaert, B. Boudart and C. Gaquiere, a1404 ORSAY France 127 (1999)

[74] W. Fawcett, A. D. Boardman and S. Swain, J. Phys. Chem. Solids. **31**, 1963, (1970)

[75] C. M. Snowman, *Semiconductor device modeling*, Springer-velag, (1989)

[76] C. M. Snowman, *Introduction to semiconductor device modelling*, World scientific, (1986)

[77] J. W. Cooley, J. W. Tukey, Mathematics of Computation. **19**, 297, (1965)

[78] G. D. Bergland, Mathematics of Computation. **21**, 236, (1967)

[79] G. D. Bergland, Mathematics of Computation. **22**, 275, (1968)

[80] C. Temperton, Journal of Computational Physics. **34**, 314, (1980)

[81] M. Walmsley and R. A. Abram, The international Journal for Computation and Mathematics. **15**, 31, (1996)

[82] B. L. Buzbee, SIAM Journal on Numerical Analysis. **18**, 722, (1971)

[83] F. Dessenne, D. Cichocka, P. Desplanques and R. Fauquembergue, Mat. Sci. Eng. **50**, 315, (1997)

[84] E. H. Rhoderick, IEE Proc, **129**, 1, (1982)

[85] W. Schockley and W. T. Read, Physical Review. **87**, 835 (1952)

[86] S. M. Sze, *Physics of Semiconductor Devices*, John Wiley, 2nd edition (1981)

[87] P. K. Schroder, *Semiconductor material and device characterization, chapter 5*, John Wiley (1998)

[88] Won. C. Sub, A. Hyungkeun, El. Nokali, Solid-State Electronics. **43**, 537 (1999)

[89] S. C. Binari, W. Kruppa and H. B. Dietrich, Solid-state Electronics. **41**, 1549 (1997)

[90] C. Moglestue, IEE Proceedings. **130**, 275 (1983)

[91] C. Moglestue, IEE Proceedings. **132**, 217 (1985)

[92] R. A. Warriner, Solid-State and electron Devices. **1**, 105 (1977)

[93] W. I. Lee and T. C. Huang, Appl. Phys. Lett. **67**, 1721 (1995)

[94] Z. Q. Fang, J. W. Hemsky and D. C. Look, Appl. Phys. Lett. **72**, 448 (1998)

[95] C. D. Wang, L. S.Yu, S. S. Lau and E. T. Yu, Appl. Phys. Lett. **72**, 1211 (1998)

[96] P. B. Klein, J. A. Freitas and S. C. Binari, Appl. Phys. Lett, **75**, 4016 (1999)

[97] S. C. Binari and D. Doverspike, Solid-state Electronics. **41**, 177 (1997)

[98] F. D. Auret and S. A. Goodman, Appl. Phys. Lett. **73**, 3745 (1998)

[99] P. Hacke, P. Ramvall and S. Tanaka, Appl. Phys. Lett. **74**, 543 (1999)

[100] D. Haase, M. Schmid, W. Kurner, A. Dornen, F. Scholz and M. Burkard, Appl. Phys. Lett. **69**, 2525 (1996)

[101] N. G. Weimann and L. F. Eastman, J. Appl. Phys, **83**, 3656 (1998)

[102] D. C. Look and J. R. Sizelove, Physical. Rev. Lett. **82**, 1237 (1999)

[103] S. M. Sze, *Semiconductor Devices: Physics and Technology*, John Wiley (1985)

[104] A. G. Milnes, *Deep impurities in semiconductors, chapter 5*, John Wiley (1973)

[105] R. H. Bube, *Photoelectric properties of semiconductors*, Cambridge university press (1992)

[106] P. B. Klein, S. C. Binari, J. A. Freitas and A. E. Wickenden, J. Appl. Phys. **88**, 2843 (2000)

[107] G. C. Crow, R. A. Abram and A. Yangthaisong, semicond. Sci. Technol. **15**, 770 (2000)

[108] F. Dessenne, D. Cichocka, P. Desplanques and R. Fauquembergue, Materials Science and Engineering. **50**, 315 (1997)

[109] M. Asif. khan and J. W. Yang, Appl. Phys. Lett. **76**, 3807 (2000)

[110] Q. Chen, M. Asif. khan, J. W. Yang and C. J. Sun, Appl. Phys. Lett. **69**, 794 (1996)

[111] K. F. Brennan, Enrico. Bellotti and M. Farahmand, Solid-state Electronics. **44**, 195 (2000)

[112] B. P. Luther, S. D. Wolter and S. E. Mohney, Sensors and Actuators. B**56**, 164 (1999)

[113] L. Hsu and W. Walukiewicz, Appl. Phys. Lett. **74**, 2405 (1999)

[114] E. P. O'Reilly, Semicond. Sci. Technol. **4**, 121 (1989)

[115] G. L. Bir and G. E. Pikus, *Symmetry and Strain-induced Effects in Semiconductors*, John Wiley, (1974)

[116] B. Jogai, Solid-state Communications, **105**, 486 (1998)

[117] J. W. Matthews and A. E. Blakeslee, J. Cryst. Growth. **32**, 265 (1974)

[118] A. Fischer, H. Kuhne and H. Richter, Phys. Rev. Lett. **73**, 2712 (1994)

[119] O. Ambacher, J. Smart, J. R. Shealy, N. G. Weimann, K. Chu and M. Murphy, J. Appl. Phys. **85**, 3222 (1999)

[120] H. Amano, T. Takeuchi, S. Sota, H. Sakai and I. Akasaki, Mater. Res. Soc. Symp. Proc. **449**, 1143 (1997)

[121] F. Bernardini and V. Fiorentini, Phys. Rev. B**57**, 9427 (1998)

[122] M. B. Nardelli, K. Rapcewicz and J. Bernholc, Phys. Rev. B**55**, 7323 (1997)

[123] A. Franciosi and C. G. De Walle, Surface Science Reports. **25**, 1 (1996)

[124] I. P. Smorchkova, C. R. Elsass, J. P. Ibbeston and U. K. Mishra, J. Appl. Phys. **86**, 4520 (1999)

[125] L. Hsu and W. Walukiewicz, Appl. Phys. Lett. **73**, 339 (1998)

[126] O. Ambacher, B. Foutz, J. Smart, J. R. Shealy, N. G. Weimann, K. Chu and M. Murphy, J. Appl. Phys. **87**, 334 (2000)

[127] Y. Ando, W. Contrata, N. Samoto, H. Miyamoto and Y. Ohno, IEEE Transaction electron devices. **47**, 1965 (2000)

[128] R. Vetury, N. Q. Zhang, S. Keller and U. K. Mishra, IEEE Transaction electron devices. **48**, 560 (2001)

[129] Sandip. Tiwari, *Compound Semiconductor Device Physics*, Academic Press, (1992)